

Cardiovascular Magnetic Resonance Imaging of Myocardial Scar and Diffuse Fibrosis

Jihye Jang

Vollständiger Abdruck der von der Fakultät für Informatik der Technischen Universität München zur Erlangung des akademischen Grades eines

Doktors der Naturwissenschaften (Dr. rer. nat.)

genehmigten Dissertation.

Vorsitzender:

Prof. Dr.-Ing. Darius Burschka

Prüfende der Dissertation:

1. Prof. Dr. Bjoern Menze
2. Prof. Reza Nezafat, Ph.D.

Die Dissertation wurde am 23.08.2019 bei der Technischen Universität München eingereicht und durch die Fakultät für Informatik am 31.12.2019 angenommen.

CARDIOVASCULAR MAGNETIC RESONANCE IMAGING OF
MYOCARDIAL SCAR AND DIFFUSE FIBROSIS

JIHYE JANG

Jihye Jang: *Cardiovascular Magnetic Resonance Imaging of Myocardial Scar and Diffuse Fibrosis* © August 2019

ABSTRACT

Sudden cardiac death is the leading cause of death, accounting for 230,000 to 350,000 deaths per year in the United States alone. Ventricular tachycardia (VT), often occurring after myocardial infarction, is one of the leading causes of sudden cardiac death. In post-infarcted hearts, previous evidence suggests that conduction channels of surviving tissue in areas of dense scar are responsible for the underlying VT mechanism. Due to the critical role myocardial fibrosis and infarction play in the development of VT, non-invasive imaging biomarkers to identify the VT substrate are desirable. This thesis investigates novel cardiovascular magnetic resonance (CMR) imaging techniques to identify the arrhythmogenic substrate. In the first study, a multimodal data approach investigates the association between non-invasive CMR imaging features and conduction velocity, as estimated from invasive clinical electrophysiology studies. In the second study, the arrhythmogenic structure within a scar is reconstructed by three-dimensional (3D) structural modeling. In the third study, 3D holographic visualization of the complex scar structure improves the 3D anatomical mechanism of a VT ablation. This thesis demonstrates that advanced CMR imaging techniques enable identification of arrhythmogenic scarring and fibrosis in the heart, offering non-invasive CMR imaging biomarkers to support VT diagnosis and treatment, ultimately enhancing risk-stratification of sudden cardiac death.

ABSTRACT

Der plötzliche Herztod ist eine der häufigsten natürlichen Todesursachen, mit 230000 bis 350000 jährlichen Todesfällen alleine in den USA. Ventrikuläre Tachykardien (VT), die häufig nach Herzinfarkten auftreten, sind eine der häufigsten Ursachen für den plötzlichen Herztod. Im post-Infarkt Stadium des Herzens sollen überlebende Zellen umgeben von dichten Narbengewebe Leitungskanäle bilden, welche das Substrat für die VT Entstehung darstellen. Aufgrund der kritischen Rolle von myokardialer Fibrose und Herzinfarkten für die Entstehung von VT sind Biomarker der nicht-invasiver Bildgebung zur VT Identifizierung klinisch notwendig. Diese Arbeit untersucht neue Bildgebungs- und Verarbeitungsverfahren der Magnetresonanztomographie (MRT) zur Identifizierung von arrhythmogenischen Substraten. In der ersten Studie wurde ein multimodaler Datenverarbeitungs-Ansatz angewendet um nicht-invasive Herz-MRT Bildmerkmale mit elektrophysiologisch invasive gemessenen Leitungsgeschwindigkeit zu assoziieren. In der zweiten Studie wurden dreidimensionale (3D) Strukturen modelliert um das arrhythmogenischen Substrat im Narbengewebe zu identifizieren. In der dritten Studie wurden holographische 3D Visualisierungen von komplexen Narben-Strukturen dazu verwendet, 3D Erkennung und das anatomische Verständnis während VT Ablationen zu verbessern. Diese Arbeit demonstriert, dass neue MRT Bildgebungsverfahren des Herzens zur Identifizierung von arrhythmogenischen Narben und Fibrose im Herzenmuskel benutzt werden können. Folgerichtig nicht-invasive Biomarker für MRT Bildgebungsverfahren unterstützen die Diagnose und Therapie von VT, was letztendlich die Risiken des plötzlichen Herztod senkt.

ACKNOWLEDGMENTS

I have been so fortunate to have everyone who has supported me through my PhD study. I couldn't have done it without all the love and support. I feel so grateful and lucky to be surrounded by such loving, passionate, and talented people. I have learned how to believe in myself, how to think like a researcher, and how to become grown-up. This journey through my PhD has become a challenging but inevitable part of my life.

I want to thank my advisor Prof. Reza Nezafat, for being such an inspiring teacher. His example has helped me grow into my potential, and he has become an umbrella and protected me from rainy days. I want to thank Prof. Bjoern Menze for being so supportive and guided me on the right path throughout my journey. He has always been there for me for any discussions for any occasions. Thanks to Prof. Elad Anter for being the kindest mentor and the countless advice on the electrophysiology and my careers. Thanks to all our previous and current lab members who I had the privilege to work with. Thanks to Maryam and Jennifer for being my best friends in and outside of the lab. Many thanks to John Whitaker for teaching me all about electrophysiology. Big thanks to Shiro Nakamori for being the best teacher and for always showing me the kindest thoughtfulness. Thanks to Johannes Rausch, who has introduced me to a deep learning and the best board game night group. Thanks to Charlene Liew for many exciting discussions on clinical and technical viewpoints. Thanks to Cory and Michael, who has taught me everything about animal experiments and electrophysiology. Thanks to Tamer, Seb, and Mehmet, who had taught me so much when I first came to the lab and had no idea what I was doing. Thanks to Beth, Sophie, and Patrick for being the best CMR teachers and all the help with my experiments. Thanks to Dr. Anja Drescher for supporting me with all my administrative matters during my PhD. Thanks to all my friends from Boston, Munich, and Korea, who nourished my PhD journey so pleasant and happy. Last but most important, enormous love for Bernd and my family for always being there for me.

CONTENTS

I INTRODUCTION AND BACKGROUND	
1 INTRODUCTION	3
1.1 Problem Statement	3
1.2 Contribution of the Thesis	3
1.3 Structure of the Thesis	4
2 BACKGROUND	5
2.1 Structure and Conduction System of the Heart	5
2.1.1 Structure of the Heart	5
2.1.2 Conduction System of the Heart	5
2.2 Ventricular Arrhythmias and Electrophysiology Study	6
2.2.1 Ventricular Arrhythmias	6
2.2.2 Electrophysiology Study	7
2.3 Cardiovascular Magnetic Resonance Imaging	9
2.3.1 Principles of Magnetic Resonance Imaging	9
2.3.2 Myocardial Tissue Characterization	13
2.4 Visualizing the Heart	15
2.4.1 Merging Multi-modal Data	15
2.4.2 Visualizing in Three-dimension	16
2.5 Pre-clinical Validation	18
2.5.1 Animal Model of Human Disease	18
2.5.2 In-vivo and Ex-vivo CMR Imaging	18
2.5.3 Histopathological Analysis	20
II METHODS AND RESULTS	
3 CMR IMAGING FEATURES AND CONDUCTION VELOCITY	23
3.1 Introduction	23
3.2 Methods	25
3.2.1 Animal Study	25
3.2.2 Animal Model	25
3.2.3 CMR Imaging	25
3.2.4 Electrophysiology Study	26
3.2.5 Local Conduction Velocity Estimation	27
3.2.6 CMR Image Analysis	29
3.2.7 Data Registration	30
3.2.8 Statistical Analyses	30
3.3 Results	31
3.3.1 CV vs. LGE	31
3.3.2 CV vs. Wall Thinning	31
3.3.3 CV vs. LGE Heterogeneity and Wall Thickness Gradient	32
3.4 Discussion	34

4	3D STRUCTURAL MODELING OF THE ARRHYTHMOGENIC HEART	39
4.1	Introduction	39
4.2	Methods	40
4.2.1	3D Structural Modeling	41
4.2.2	3D Skeletonization	42
4.2.3	Heterogeneous Myocardial Channel Detection	42
4.2.4	Animal Study	43
4.2.5	CMR Imaging	44
4.2.6	Electrophysiology Study	45
4.2.7	Histopathological Analysis	45
4.2.8	Statistical Analyses	45
4.3	Results	46
4.3.1	Animal Model	46
4.3.2	3D Structural Modeling and HT Channel Detection	46
4.3.3	HT Channel and VT Inducibility	47
4.3.4	Site of Origin of VT	47
4.3.5	Comparison to Histology	48
4.4	Discussion	48
5	3D HOLOGRAPHIC VISUALIZATION OF MYOCARDIAL SCAR	53
5.1	Introduction	53
5.2	Methods	54
5.2.1	Myocardial Geometry Reconstruction	55
5.2.2	Voxel-wise 3D Scar Rendering	55
5.2.3	Surface Projection of the Scar	55
5.2.4	Augmented Reality System	56
5.2.5	Pilot Animal Study	56
5.2.6	CMR Imaging	58
5.3	Results	59
5.3.1	Animal Model	59
5.3.2	Augmented Reality System Performance	59
5.3.3	Holographic Visualization of 3D LGE	59
5.4	Discussion	60
III DISCUSSION AND OUTLOOK		
6	DISCUSSION	67
7	OUTLOOK	69
BIBLIOGRAPHY		
		71

LIST OF FIGURES

Figure 2.1	Anatomy of the heart [62].	6
Figure 2.2	The wall of the heart [92].	7
Figure 2.3	Conduction system of the heart [56].	8
Figure 2.4	Normal heart rhythm vs. ventricular tachycardia [29].	9
Figure 2.5	Catheter for recording electrical activity of the heart [114].	10
Figure 2.6	Cardiac ablation therapy for arrhythmias [10].	10
Figure 2.7	Magnetization [81].	11
Figure 2.8	Excitation [81].	11
Figure 2.9	T1 relaxation [81].	12
Figure 2.10	T2 relaxation [81].	12
Figure 2.11	Signal encoding [81].	12
Figure 2.12	Acquisition and image formation [81].	13
Figure 2.13	Late gadolinium enhancement imaging to maximize contrast between scar and healthy myocardium signal.	14
Figure 2.14	Myocardial T1 mapping imaging for tissue characterization.	14
Figure 2.15	Fiducial based registration to merge multimodal data.	15
Figure 2.16	Iterative closest point algorithm to align two point clouds.	16
Figure 2.17	Hammer projection in left ventricle to minimize surface area distortion [55].	16
Figure 2.18	Volume ray casting of the heart with myocardial infarction.	17
Figure 2.19	Isosurface rendering of myocardial surface and the scar.	17
Figure 2.20	Swine model of myocardial infarction via percutaneous balloon occlusion of the left anterior descending (LAD) coronary artery [119].	18
Figure 2.21	A swine research subject undergoing a cardiac MRI scanning under general anesthesia [117].	19
Figure 2.22	3D printed models of left and right ventricles inserted in the ex-vivo heart to maintain the basic geometry.	19
Figure 2.23	CMR and histopathological images of a swine heart with myocardial infarction.	20

- Figure 3.1 Study flowchart. Animal model of healed myocardial infarction (MI) was created by mid left anterior descending (LAD) coronary artery ischemia-reperfusion. After 9 weeks of surviving periods, in-vivo cardiovascular magnetic resonance (CMR) was performed. After 0-5 days of recovery, an electrophysiology (EP) study was performed and electroanatomic maps were acquired while pacing from the RV apex (RVA) at cycle length of 400 ms. CMR and EP data were processed to extract CMR features including late gadolinium enhancement (LGE) and left ventricular wall thickness. Conduction velocity (CV) was estimated using triangulation technique. CMR and CV data were spatially registered to study their associations. 26
- Figure 3.2 Analysis pipeline for investigating association between CMR features and conduction velocity (CV). (A) CV was estimated based on the local activation time (LAT) map using triangulation technique. (B) Endo-/epicardial contours were delineated to perform CMR feature projection on left ventricular endocardial surface model. (C) CV and CMR data were then spatially registered using fiducial registration based on right coronary artery (RCA), left main stem (LMS), and apex. CV and CMR data were then 2D projected on the semi-hemisphere map to minimize the surface area distortion using a Hammer mapping. 28
- Figure 3.3 Conduction velocity (CV) and CMR features from 2 animals. CV was estimated based on the local activation time (LAT). CV and CMR data were registered in the same spatial coordinates. Slower CV was observed in the region of hyper-enhancement on LGE and wall thinning. The pattern of CV was inhomogeneous throughout the scar with maximal slowing in the region of dense scar with higher LGE heterogeneity or wall thickness gradient. 32
- Figure 3.4 Scatter plots of LGE, wall thickness, LGE heterogeneity, and wall thickness gradient vs. conduction velocity (CV) of all 6 animals. Smoothing splines of each animal are overlaid on the scatter plots. 34

- Figure 3.5 Conduction velocity (CV) in the presence and absence of LGE averages over all animals (A) and for each individual animal (B). Slower CV was observed in the areas of hyperenhancement on LGE (LGE+). 36
- Figure 3.6 Conduction velocity (CV) in the presence and absence of wall thinning averages over all animals (A) and for each individual animal (B). Significantly slower CV was observed in areas of wall thinning+ compared to regions of wall thinning-. 37
- Figure 4.1 (A) A 3D volume rendered view of the 3D ex-vivo cardiovascular magnetic resonance (CMR) (yellow, scar; red, viable myocardium) and 3D structural model of viable myocardium in and around the scar generated with triangular surface meshes (yellow, scar; red, viable myocardium). (B) Proposed workflow for detection of a macro-level heterogeneous tissue (HT) channel uses scar and myocardium segmentation from CMR images as input and performs the following steps. Step 1: A 3D structural model of viable myocardium is generated from 3D CMR images to visualize the propagation pathway of a cardiac electrical signal. Step 2: 3D skeletonization of viable myocardium is performed to extract the simplified geometry of the viable tissue and automatize structural model characterization. Step 3: HT channels are automatically detected based on the 3D skeleton segmental analysis that identify HT channels with a high 3D structural complexity. 40

- Figure 4.2 The proposed pipeline for building the 3D structural viable myocardium model. Upper panels show ex-vivo cardiovascular magnetic resonance images with overlaid myocardial segmentation (red), and the 3D structural model view of the corresponding segmentation (red) is represented in the lower panels. The whole ventricular 3D volume is shown in transparent gray. A) Scar and myocardium segmentation are used as an input to the system. B) Myocardium in and around the scar was extracted by expanding the 3D volume of the segmented scar to include neighboring myocardium. C) The scar was removed from the myocardium to exclude scarred tissues and to focus only on the viable myocardium where electrical signals propagate. Scar volume was expanded 1mm before subtracting to remove partial volume errors. 41
- Figure 4.3 The proposed pipeline for 3D skeletonization to simplify viable myocardium geometry and enable automated quantification of the 3D viable myocardium model (A). Laplacian-based maximal voluntary contraction (MVC) (B) and conformal contraction (C) were performed to abstract and smooth the shape of the complex structures of the 3D model. 3D skeletonization was performed by topological thinning, resulting in a 3D skeleton with its simplified geometry represented by lines (D). During the skeletonization process, each segment of the structural model is contracted as a point on the 3D skeletal graph, so that the structural properties of the model can be automatically characterized using the skeletal graph (E). 43

Figure 4.4 The proposed algorithm for automated heterogeneous tissue (HT) channel detection. The algorithm consists of two steps: 1) skeleton segmental analysis of the cross-sectional area to detect narrow and connected segments to identify viable myocardial channels, and 2) HT channel detection based on the 3D structural complexity to detect HT channels that are known to cause slow conduction. A) For each skeletal point, its orthogonal axis is computed based on its two adjacent nodes, and the cross-sectional plane is calculated. Any connected segments with a cross-sectional area less than 90 mm² are automatically detected to identify narrow strips of tissue. B) Detected myocardial channels are further evaluated for tissue heterogeneity based on the 3D structural complexity defined as the unit number of triangular faces. Any myocardial channel with a heterogeneity index (unit number of triangular faces) greater than 26 was identified as an HT channel. 44

Figure 4.5 Example of 3D structural viable myocardium models, 3D skeletons, and detected heterogeneous tissue (HT) channel in an animal with an inducible ventricular tachycardia (VT) and an animal with a non-inducible VT. The 3D viable myocardium model was able to represent surviving and viable myocardium in and around the scar in a true 3D manner for each case (A-B). 3D skeletonization enabled simplification of the geometry of the viable myocardium (C-D). An HT channel was detected in the animal with the inducible VT (E), whereas it was not detected in the animal with the non-inducible VT (F). 46

- Figure 4.6 Results of heterogeneous tissue (HT) channel detection. A) HT channel was detected in all animals with inducible ventricular tachycardias (VT), whereas it was only detected in one animal with a non-inducible VT. Animals with inducible VTs were more likely to have HT channels detected than animals with non-inducible VTs ($P < 0.01$, Fisher's exact test). B) Of all animals with detected HT channels, only one non-inducible VT animal had a shorter channel length (inducible-VT animals: 35 ± 14 mm vs. non-inducible VT animal: 9.94 mm). 47
- Figure 4.7 3D viable tissue model and detected HT channels compared to the electroanatomic mapping data in 3 animals with inducible VT. Bipolar voltage maps during sinus rhythm in both right and left ventricles show similar scar distribution compared to the CMR 3D model. VT exits identified in the activation maps during VT are located near the anterior side of interventricular groove, consistent with where HT channels were detected. 49
- Figure 4.8 Comparison between CMR and histopathological analyses. A $5\text{-}\mu\text{m}$ histological slide with Masson's trichrome staining are shown in an anterior-posterior projection. The histological specimen shows complex scar architecture with areas of transmural scar and subendocardial preservation, along with extensive RV and interventricular septum involvement. The overall architecture and distribution of scar were consistent with the LGE data. 50
- Figure 5.1 A framework for holographic visualization of the 3D late gadolinium enhancement (LGE) data. Endo- and epicardial contours are delineated in LGE images and surface-projected scar and voxel-wise 3D scar models are generated. 3D models are converted to Filmbox (FBX) file format to be able to load on 3D Viewer Beta (Microsoft, Redmond, WA). 3D scar LGE models are holographically visualized in the 3D mixed-reality space, which provides true 3D perception of the complex scar architecture with immersive experience to explore the 3D LGE images with a touchless interaction while maintaining sterile environment. 54

- Figure 5.2 A framework for holographic visualization of the 3D late gadolinium enhancement (LGE) data. Left/ right ventricular (LV/ RV) endo-/ epicardial contours are manually delineated on short-axis view, and LV/RV endo-/ epicardial surfaces are estimated using Poisson surface reconstruction. Scar tissue was defined as voxels in the myocardium with signal intensity greater than a full-width at half-maximum (FWHM). Every voxel was then rendered into a single cube with the actual resolution of the LGE scan. All surface and scar layers were blended with different transparency and color to enhance visibility and perception. 56
- Figure 5.3 A framework for holographic visualization of endocardial surface with scar projection. LV endo-/ epicardial contours are manually delineated on short-axis view. Endocardial surface is then generated using a Poisson surface reconstruction by first performing clustering decimation followed by the surface orientation estimation based on the 10 neighboring points. To project color-coded scar information on the reconstructed endocardial surface, myocardium was divided into subendo, mid, subepicardial regions, and the subendocardial scar information was projected onto the endocardial surface mesh. 57
- Figure 5.4 A flowchart of the pilot animal experiment. Myocardial infarction was created by occluding the mid left anterior descending artery. After 8 weeks of recovery and survival periods, animals underwent in-vivo CMR with high-resolution 3D LGE sequence. Based on the in-vivo CMR images, HoloLens 3D LGE model was generated and tested with the electroanatomic substrate mapping. After the electrophysiology study, ex-vivo imaging was performed to create higher-resolution HoloLens 3D LGE model. 58

- Figure 5.5 Demonstration of the 3D holographic visualization of the voxel-wise 3D scar rendering and scar projected endocardial surface mesh from 3D LGE data that are generated based on the proposed framework. User can interactively explore 3D LGE myocardial scar by scaling, rotation, moving, and viewing from any perspective in the augmented reality environment (A). In the 3D scar rendered model, as user walks closer to the model, the transparent epicardial surface layer becomes invisible and the inner scar volumes can be explored more in detail (B). Augmented reality representation of the 3D LGE data provides embodied experience to explore the clinical standard LGE images in a more interactive, and interpretable way. 61
- Figure 5.6 Demonstration of the HoloLens 3D LGE during the electroanatomic mapping and radio-frequency ablation of ventricular tachycardia in the pilot animal study. Holographic voxel-wise 3D LGE was created as proposed using the in-vivo CMR high-resolution 3D LGE images. The holographic LGE models were tested during the electrophysiology procedure. In the operator view, holographic scar can be compared with the electroanatomic data by overlaying holograms on the mapping system (A). The scar information facilitates navigation of electroanatomic mapping procedures (B). 62
- Figure 5.7 The perceived usefulness questionnaire results from operator and mapping specialist. The usefulness rating is reported as a mean rating of all 6 usefulness items in the questionnaire. Both operator and mapping specialist found HoloLens 3D LGE useful (usefulness rating: operator, 5.8; mapping specialist, 5.5, on a scale from 1 to 7). 63

LIST OF TABLES

Table 3.1	Estimated mean differences in CV between LGE+ and LGE-, 95% confidence interval (CI), and p-value of general linear modeling and of multilevel model of all animals and each individual animal. The model: $CV = \beta_0 LGE + \beta_1 wall\ thinning + \varepsilon$. 33
Table 3.2	Estimated mean difference in CV between wall thinning+ and wall thinning-, 95% confidence interval (CI), and p-value of general linear modeling and of multilevel model of all animals and each individual animal. The model: $CV = \beta_0 LGE + \beta_1 wall\ thinning + \varepsilon$. 33
Table 3.3	The regression slope, 95% confidence interval (CI) and p-value of generalized linear modeling of CV vs. LGE heterogeneity of multilevel model of all animals and each individual animal. The model: $CV = \beta_0 LGE + \beta_1 LGE\ heterogeneity + \beta_2 wall\ thickness + \beta_3 wall\ thickness\ gradient + \varepsilon$. 35
Table 3.4	The regression slope, 95% confidence interval (CI) and p-value of generalized linear modeling of CV vs. wall thickness gradient of multilevel model of all animals and each individual animal. The model: $CV = \beta_0 LGE + \beta_1 LGE\ heterogeneity + \beta_2 wall\ thickness + \beta_3 wall\ thickness\ gradient + \varepsilon$. 35
Table 5.1	System Performance of HoloLens with the 3D LGE Models. Baseline (when nothing is running on the HoloLens), surface-projected model (when surface projected scar model is running on the HoloLens), and voxel-wise 3D model (when voxel-wise 3D model is running on the HoloLens) were compared for system on a chip (SoC) power, system power, frame rate, CPU, and GPU usage. 60

LIST OF PRIOR PUBLICATIONS

- [1] Jihye Jang, Cory M Tschabrunn, Michael Barkagan, Elad Anter, Bjoern Menze, and Reza Nezafat. "Three-dimensional holographic visualization of high-resolution myocardial scar on HoloLens." In: *PloS one* 13.10 (2018), e0205188.

- [2] Jihye Jang, Hye-Jin Hwang, Cory M. Tschabrunn, John Whitaker, Bjoern Menze, Elad Anter, and Reza Nezafat. "Cardiovascular Magnetic Resonance-Based Three-Dimensional Structural Modeling and Automated Heterogeneous Tissue Channel Detection in Ventricular Arrhythmia." In: *Scientific Reports* 9.1 (2019), p. 9317.
- [3] Jihye Jang et al. "Local Conduction Velocity in the Presence of Late Gadolinium Enhancement and Myocardial Wall Thinning: A Cardiac Magnetic Resonance Study in a Swine Model of Healed Left Ventricular Infarction." In: *Circulation: Arrhythmia and Electrophysiology* 12.5 (2019), e007175.

Part I

INTRODUCTION AND BACKGROUND

INTRODUCTION

1.1 PROBLEM STATEMENT

Sudden cardiac death (SCD) is the leading cause of death, which accounts for approximately 230,000 to 350,000 deaths per year in the United States alone [4, 18]. The societal burden of SCD is high relative to other major causes of death, and optimizing and monitoring SCD prevention and treatment should be a high priority [113]. Ventricular tachycardia (VT) is one of the main causes of SCD, in particular in patients with structural heart disease with a prior myocardial infarction [25]. Due to a critical role of scar and fibrosis involved in the development of VT, non-invasive imaging biomarkers to identify the underlying arrhythmogenic structure is desirable. Imaging biomarkers to identify arrhythmogenic scar and fibrosis will help to identify VT substrate, ultimately improve risk stratification for SCD.

1.2 CONTRIBUTION OF THE THESIS

The overall objective of this thesis is to identify non-invasive imaging biomarkers of the arrhythmogenic substrate of VT using cardiovascular magnetic resonance (CMR) imaging and computer vision techniques. This thesis presents novel CMR imaging techniques to investigate and understand better the anatomical structure of the arrhythmogenic heart, which provides a basis for cardiac electrical conduction and underlying structural mechanism of VT.

The first study presented in this thesis performs multimodal data processing to associate various non-invasive CMR imaging features with conduction velocity. Conduction velocity was estimated using a triangulation technique from invasive electroanatomic mapping. This study offers a structural understanding of the slowing of cardiac conduction, which is an important clinical parameter for the initiation and maintenance of VT.

In the second study, 3D structural modeling was performed to reconstruct the arrhythmogenic structure within a myocardial scar. Skeletonization was implemented to simplify the structure and automate the characterization of structural properties to pinpoint the heterogeneous structure, which causes a slowing of conduction and is susceptible to VT.

The last study demonstrated 3D holographic visualization of the complex scar structure to improve 3D perception and understanding of the scar architecture and support VT intervention. The ventricular

shape was modeled with Poisson surface reconstruction, and scar structures were rendered voxel-wise. Mixed-reality visualization offers enhanced 3D perception and interaction while maintaining a sterile environment.

This thesis contributes to improving our understanding of arrhythmogenic VT substrate by characterizing the relationship between CMR imaging features (anatomical) vs. invasive electroanatomic mapping (electrical). Suggested imaging-based risk factors improve our current risk stratification for VT, and visualization techniques enable the effective presentation of arrhythmogenic heart to support diagnosis and treatment of VT.

1.3 STRUCTURE OF THE THESIS

This thesis is structured as follows:

In Chapter 2, the relevant technical and clinical background of the thesis will be introduced.

In Chapter 3, a study of a non-invasive CMR imaging identification of the region of slow conduction will be presented.

In Chapter 4, a study of a 3D structural modeling of arrhythmogenic structure will be presented.

In Chapter 5, a study of a 3D holographic visualization of a myocardial scar to support VT intervention will be presented.

In Chapter 6, presented works will be summarized and assessed.

In Chapter 7, future works and outlook will be discussed.

BACKGROUND

2.1 STRUCTURE AND CONDUCTION SYSTEM OF THE HEART

The heart plays a crucial role in maintaining our life. The heart generates freshly oxygenated blood and supplies them to our body. The heart keeps beating due to a conduction system, which stimulates the heart to beat and maintains a regular heart rhythm. An abnormal function of a heart just for a few seconds can risk our life. In this thesis, we study both the structure and conduction system of the heart by cardiovascular magnetic resonance (CMR) imaging and electrophysiology studies to understand the associations between them in patients with abnormal heart rhythm.

2.1.1 *Structure of the Heart*

The primary function of the heart is to take deoxygenated blood from the body, send it to the lungs to re-oxygenate it, and send this fresh blood from the lung again to the body. The deoxygenated blood comes from superior and inferior vena cava to the right atrium, and right atrium sends blood into the right ventricle. Then, right ventricle sends the blood to the lungs through the Pulmonary artery. Oxygenation of the blood happens in the lungs by exchanging the oxygen and carbon dioxide in the blood, which sends oxygenated blood to the left atrium through the pulmonary vein. Left atrium sends blood to the left ventricle, and left ventricle contracts to push and send oxygenated blood to the whole body through the aorta. The structure of the heart is illustrated in [Figure 2.1](#).

As both of ventricles require durable contraction power to pump out the blood, ventricles have a muscular wall. Three layers are consisting the wall of the heart: myocardium is a thick middle layer, the epicardium is the outer layer, and the endocardium is the inner layer of the heart ([Figure 2.2](#)). Cardiomyocytes, individual heart muscle cells, joined together by intercalated discs, encased by collagen fibers and other substances and form the extracellular matrix.

2.1.2 *Conduction System of the Heart*

The heart is contracted regularly from the electrical stimulus. A conduction system of the heart controls the electrical stimulus of the heart and regulates the heart rhythm. An initial electrical stimulation happens at the sinoatrial node (SA), and then the electrical signal is

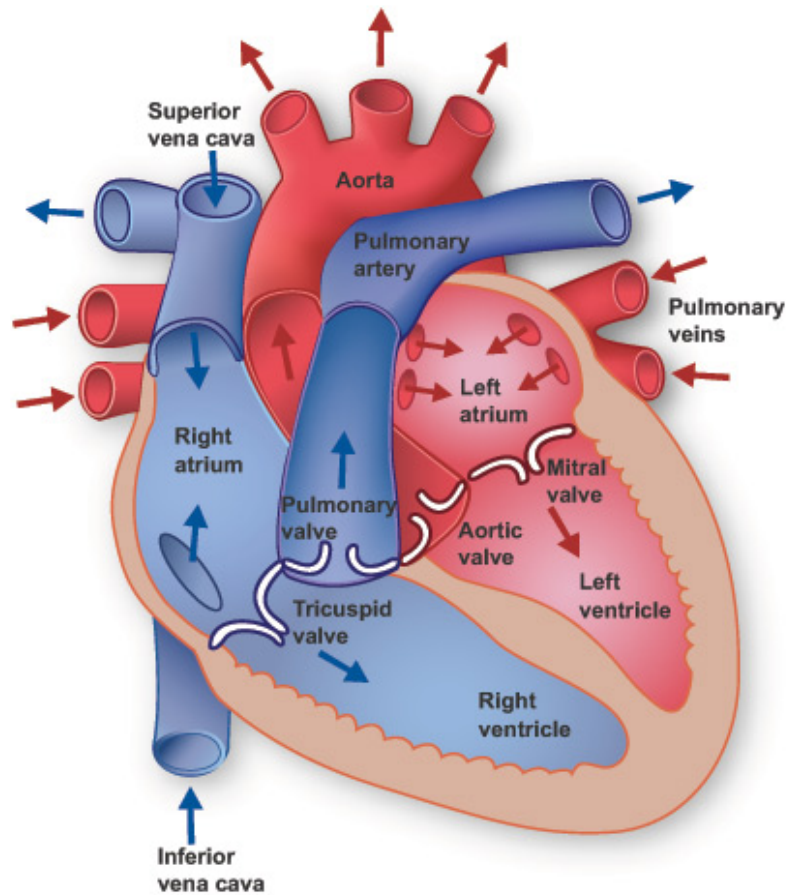


Figure 2.1: Anatomy of the heart [62].

sent to the atrioventricular (AV) node. From the AV node, the electrical signal travels to left and right ventricles, from His bundle to the left and right bundle branch, and spreads through myocardium through Purkinje fibers. The conduction system of the heart is illustrated in Figure 2.3.

2.2 VENTRICULAR ARRHYTHMIAS AND ELECTROPHYSIOLOGY STUDY

2.2.1 Ventricular Arrhythmias

Ventricular arrhythmias refer to irregular heartbeats which originate from ventricles of the heart and can threaten one's life in a second. Ventricular tachycardia (VT) is a regular but fast heartbeat usually faster than 120 bpm. Ventricular fibrillation (VF) is when the heart beats with rapid and erratic electrical impulses so that it quivers instead of pumping. The most common cause of VF is acute coronary

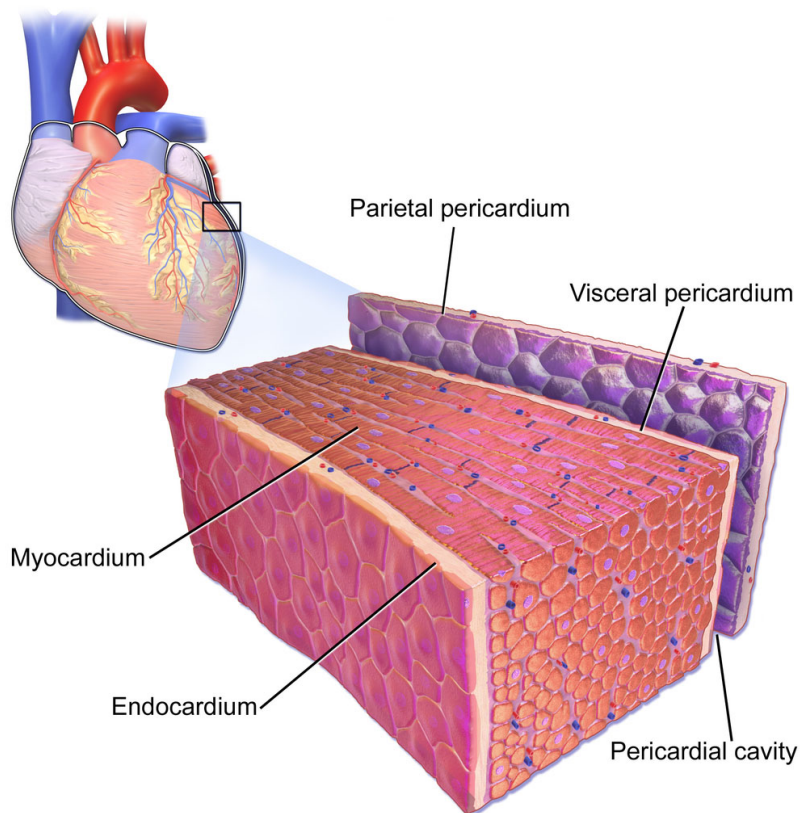


Figure 2.2: The wall of the heart [92].

ischemia, whereas the most common cause of sustained monomorphic VT in patients with structural heart disease is a myocardial scar from prior infarct [25]. VT after previous myocardial infarction is the focus of this thesis.

We can classify VT according to duration, morphology, and hemodynamic effect. Nonsustained VT terminates spontaneously without substantial hemodynamic compromise. Sustained VT lasts longer than 30 seconds requires intervention to terminate before severe hemodynamic compromise or syncope. VT is described as monomorphic when each QRS complex resembles the next one. Polymorphic VT is when QRS complexes vary in appearance from beat to beat during tachycardia (Figure 2.4).

2.2.2 Electrophysiology Study

Electrophysiology (EP) study is performed to identify the origin of arrhythmias and to treat the arrhythmogenic regions in the heart. EP study is an extensively long and invasive procedure. The patient is put general anesthesia before EP study. The heart is accessed using

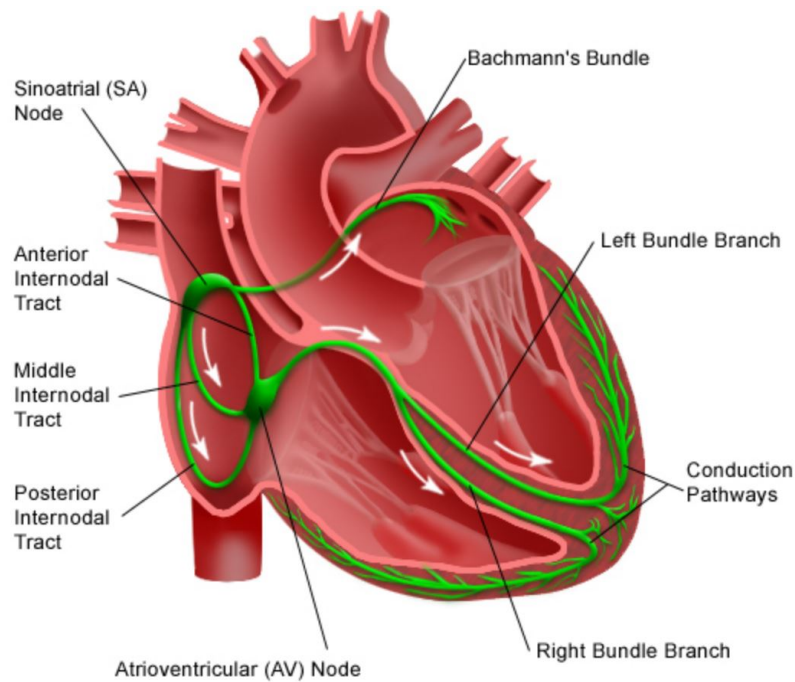


Figure 2.3: Conduction system of the heart [56].

catheters via the femoral vein (Figure 2.5). Different types of catheters are used to access the different parts of the heart. Often, left ventricle (LV) is accessed using a basket catheter, which the 64-electrode catheters are opened and contacted to endocardium when reached within LV. Each electrode records the electrical signal where it contacts within a single heartbeat. When recording a bipolar signal, we consider the ground reference electrode concerning its neighbor electrode. For a unipolar signal, we locate the ground reference electrode at inferior vena cava (IVC). We also record the spatial location of each electrode by using a location magnet, where three magnetic coils, beneath the patient and table, are used as a reference to calculate the location of the third magnetic coil within the catheter. It allows reconstruction of the cardiac chamber geometry and provides an electrical signal map overlaid on this geometry.

2.2.2.1 VT Ablation

VT ablation is a procedure to eliminate the areas of the heart where erratic electrical signals arise such can cause one's heart to beat ineffectively. The goal of VT ablation procedure is to stop the incorrect electrical signals and restore a normal heart rhythm. If the abnormal heartbeat is coming from inside of the heart, catheters are used to damage and block the electrical signals of the tissue which contributes to VT, by transmitting radio-frequency electrical energy (Figure 2.6).

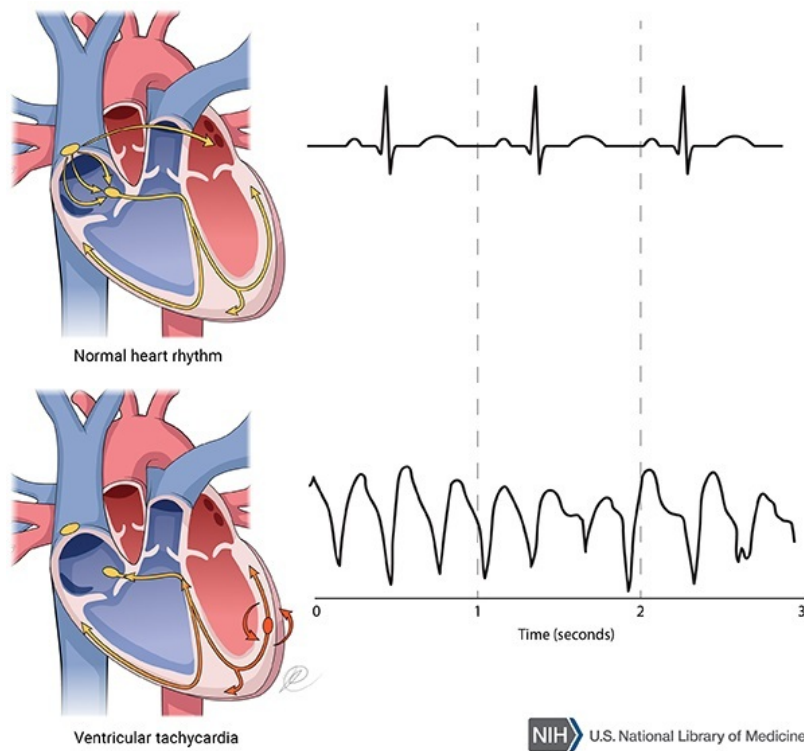


Figure 2.4: Normal heart rhythm vs. ventricular tachycardia [29].

2.3 CARDIOVASCULAR MAGNETIC RESONANCE IMAGING

The main method of this thesis is cardiovascular magnetic resonance imaging (MRI). Cardiovascular MRI is used to assess the anatomy and function of the heart to detect or monitor various cardiovascular diseases. Cardiovascular MRI has become the reference standard imaging test for many cardiovascular conditions based on the extensive and growing evidence [97].

2.3.1 Principles of Magnetic Resonance Imaging

The human body consists of over 80% of water- and water consists of 2 hydrogens and one oxygen atom. MRI uses hydrogen as a source of contrast, which is abundant in the human body and generates an image via physical and mathematical formulations [20].

2.3.1.1 Magnetization

The proton is electrically charged, and rotates around its axis, like earth. When we put a person in a magnet with a strong magnetic field, the hydrogen protons in the human body align with the magnetic field, and they start precession at their Larmor frequency due to the

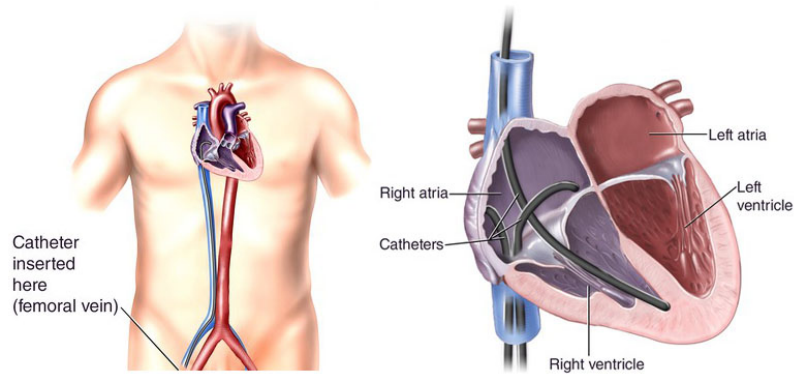


Figure 2.5: Catheter for recording electrical activity of the heart [114].

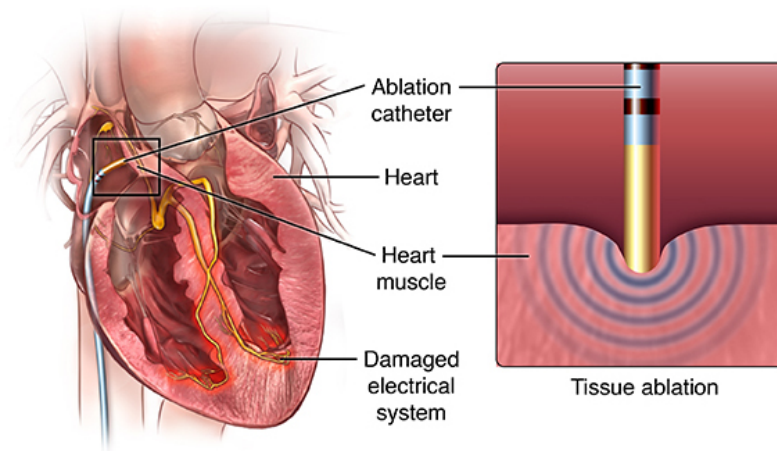


Figure 2.6: Cardiac ablation therapy for arrhythmias [10].

magnetic momentum of the atom. In the end, a net magnetization sums up in the same direction as the MRI scanner's magnetic field (Figure 2.7).

2.3.1.2 Excitation

The center frequency of the MRI system is 63.855 MHz in 1.5T magnet. By sending a radio frequency (RF) pulse with a frequency that matches the center frequency of the system, we can create resonance, and only protons which spin with the same frequency will respond to that RF pulse. By transmitting an RF pulse at the center frequency with a certain strength and period, it is possible to rotate the net magnetization with a specific flip angle of 0 180 degree, which is called excitation (Figure 2.8).

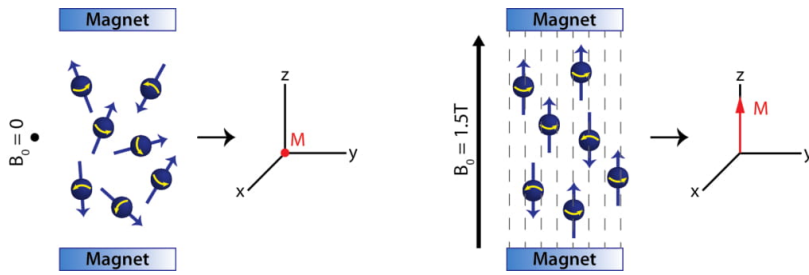


Figure 2.7: Magnetization [81].

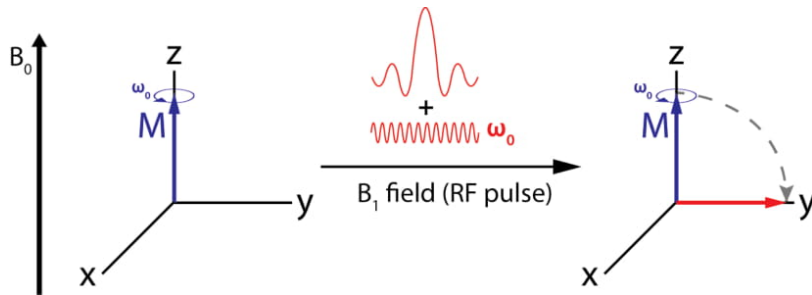


Figure 2.8: Excitation [81].

2.3.1.3 Relaxation

We rotate the protons to the direction of a net magnetization by performing excitation. It causes protons to be in a higher energy state by absorbing energy from the RF pulse. Protons, therefore, want to go back to their original energy state, called equilibrium, by releasing the absorbed energy. This process is called relaxation, and consists of two parts, depending on the directions: T₁ and T₂ relaxation.

T₁ Relaxation T₁ relaxation is called Spin-Lattice relaxation and describes what happens in the Z direction (spin-lattice relaxation). Each tissue differently bounded in their molecules; for example, fat tissue has tighter bound, and the water tissue has looser bound. Tightly bound protons will release energy to their surroundings quicker than loosely bound protons. It provides a source of T₁ contrast in MRI - Every tissue has different T₁ time. T₁ relaxation time is a time for the longitudinal magnetization (M_z) to reach back to 63% of their original magnetization (Figure 2.9).

T₂ Relaxation T₂ relaxation describes the relaxation in the X-Y plane (spin-spin relaxation) and is an independent process with a T₁ relaxation. Depending on the tissue and pathophysiology, bound of proton in its molecule and rate of de-phasing are different. Fat tissue will de-phase more quickly, and water will de-phase slower. T₂ time is the time it takes for the spins to de-phase to 37% of their original transverse magnetization (M_t) (Figure 2.10).

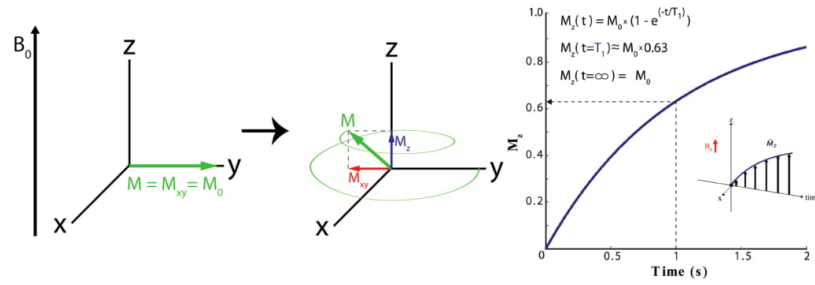


Figure 2.9: T1 relaxation [81].

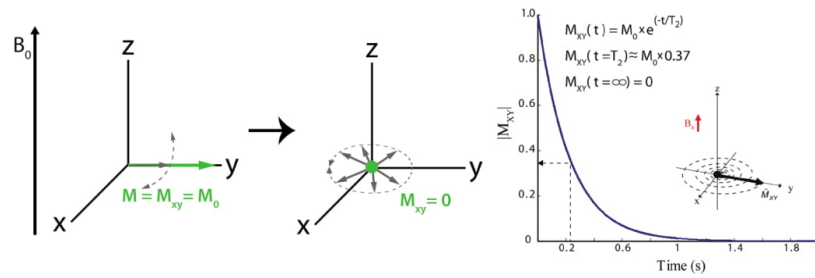


Figure 2.10: T2 relaxation [81].

2.3.1.4 Signal Encoding

Signal encoding is a process to determine where the signal is coming from so that we can generate an image.

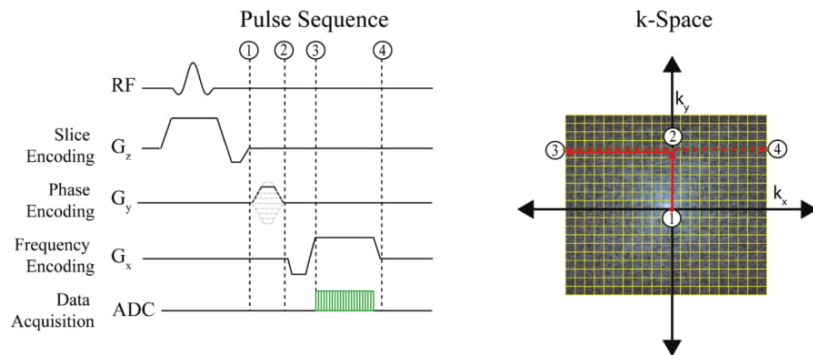


Figure 2.11: Signal encoding [81].

Imaging Slice: Z Direction The first step is to select a slice for imaging. Z-gradient is switched on, and it generates an additional magnetic field in the Z-direction, superimposed on B_0 . As a result, along the entire slope of the gradient, there will be a different B_0 field, and consequently, the spin of the proton will be at slightly different frequencies. Now, we apply an RF pulse with a frequency of the protons in the imaging slice, and only the protons in this selected slice with the same frequency will respond.

Imaging Plane: X-Y Direction Similar to the Z-direction spatial encoding, the G_y gradient is switched on, and it creates an additional gradient magnetic field in the Y-direction. It results in protons to spin slightly faster or slower throughout Y-direction. When the G_y gradient is switched off, each proton in the Y-direction spins with the same frequency, but with different phase. Subsequently, the last G_x gradient is switched on, and it creates an additional gradient magnetic field and different frequencies in the X-direction, while maintaining previously acquired phase difference from the G_y gradient. Finally, each voxel within the same imaging slice has a unique combination of frequency and phase in X- and Y-directions, and we can know the exact location where the signal comes from (Figure 2.11).

2.3.1.5 Acquisition & Image Formation

During the relaxation process, the spins release their excess energy, in the shape of radio-frequency waves. MRI image acquisition proceeds by receiving these energies by using a receiver coil - When a magnetic field goes through the loop, it induces a current due to Faraday's Law. The received signal is then sent to a computer, and a 2D Fourier transform is performed to calculate the exact location and signal intensity of each voxel. Finally, the image is generated (Figure 2.12).

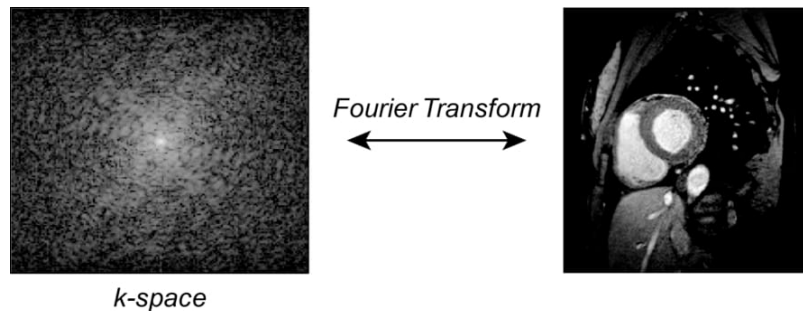


Figure 2.12: Acquisition and image formation [81].

2.3.2 Myocardial Tissue Characterization

Late Gadolinium Enhancement (LGE) Late gadolinium enhancement (LGE) is a clinical gold standard for imaging myocardial scar. T_1 relaxation is the basis of LGE imaging. After 15-20 min of the Gadolinium injection, it stays in the scarred tissue, and decrease the T_1 time of the scarred tissue, but not healthy and normal myocardial tissue. By imaging at this time point, we can achieve the highest image contrast between scar and healthy normal tissue. An inversion pulse is applied, and we perform the imaging when the signal of healthy my-

o-cardium is nulled to maximize the contrast between scar and normal myocardium (Figure 2.13).

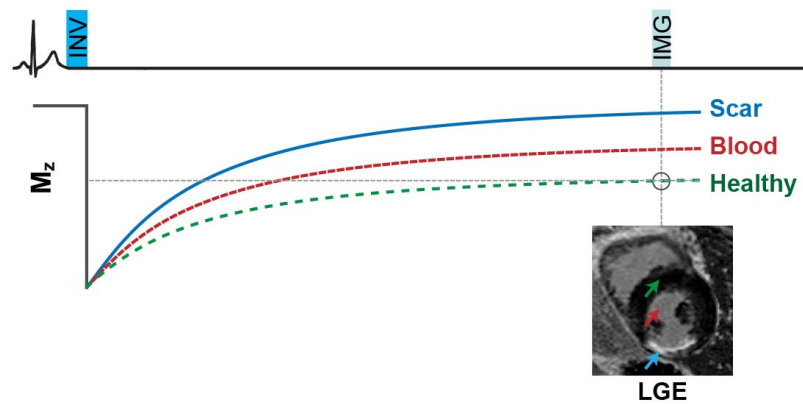


Figure 2.13: Late gadolinium enhancement imaging to maximize contrast between scar and healthy myocardium signal.

Myocardial Parametric Mapping CMR parametric mapping allows quantification of biopathological changes in myocardium based on the myocardial parameters, such as T_1 , T_2 , T_2^* and ECV. Unlike qualitative imaging, quantitative mapping permits both visualization and quantification of the disease process, independent of whether the myocardial disease is focal or diffuse. Myocardial parametric mapping is performed by acquiring a series of T_1 -, T_2 -, or T_2^* -weighted images at different time points and fitting them in physical models of T_1 , T_2 , or T_2^* time in a voxel-wise manner, as illustrated in Figure 2.14.

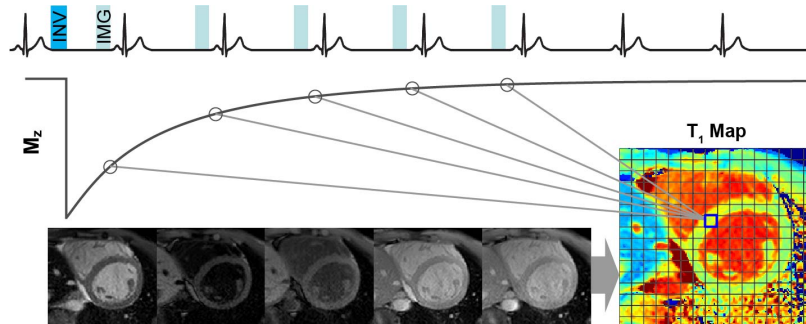


Figure 2.14: Myocardial T_1 mapping imaging for tissue characterization.

2.4 VISUALIZING THE HEART

2.4.1 Merging Multi-modal Data

In this thesis, we perform various spatial alignment approach to investigate multimodal data from CMR and electrophysiology studies simultaneously.

2.4.1.1 Fiducial Based Registration

We used fiducial-based registration as the first step of spatial alignment of two 3D objects. Several landmarks are first manually defined in two independent data, and we perform spatial alignment based on these landmarks by minimizing the distance between each pair of fiducials. It is a rigid registration, where we fix the distance of all points in each 3D objects, and two objects are aligned based on the landmarks (Figure 2.15). We perform finer registration in the next steps.

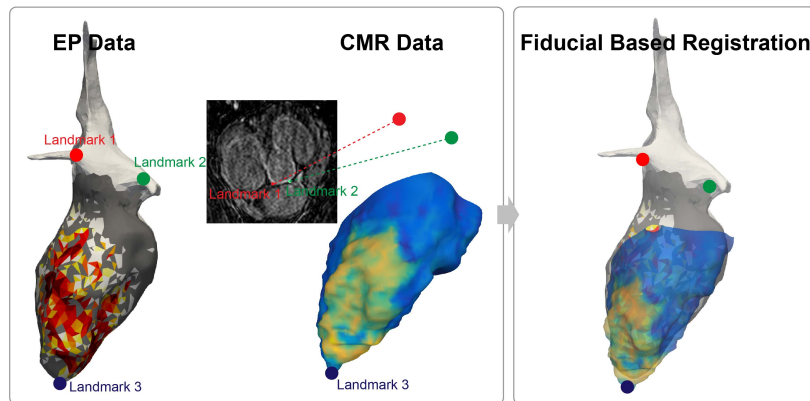


Figure 2.15: Fiducial based registration to merge multimodal data.

2.4.1.2 Iterative Closest Point Algorithm

Iterative closest point (ICP) algorithm aligns two 2D/3D point clouds by minimizing the distance between two point clouds iteratively (Figure 2.16). ICP is non-rigid and point-to-point surface registration, where it estimates rotation and translation for each point to match the source to the closest point in the reference point cloud. A minimization technique is applied to minimize a distance metric such as root-mean-square.

2.4.1.3 2D Projection of 3D Data

We aligned multimodal data into the same spatial coordinate system 3-dimensionally. Another way to bring two different data is a 2D projection of each data into the same coordinate system.

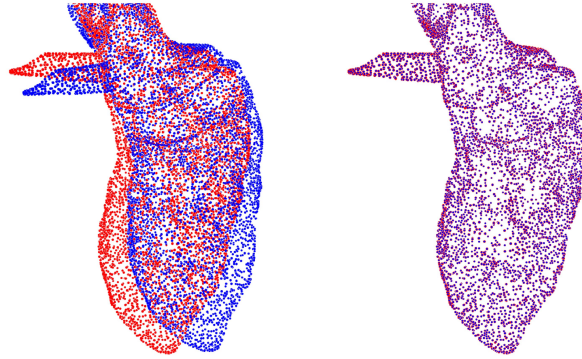


Figure 2.16: Iterative closest point algorithm to align two point clouds.

For left ventricle (LV), hammer mapping is a simple yet powerful approach to visualize the complete ventricles on a 2D coordinate. LV has a shape of 3D semi-sphere, and therefore, we can imagine to open the LV through a transmural cut in one of the wall and put down on a surface according to mathematically formulated projection (Figure 2.17). Hammer projection is designed initially to map the earth on a 2D hemisphere while minimizing the surface area distortion.

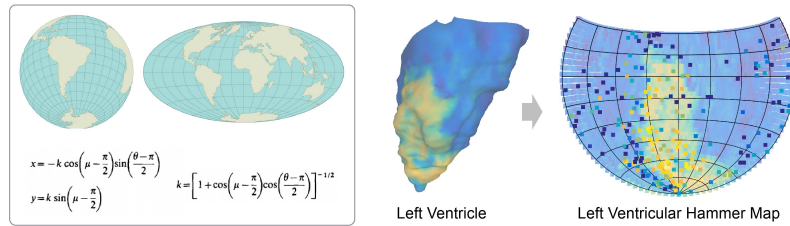


Figure 2.17: Hammer projection in left ventricle to minimize surface area distortion [55].

2.4.2 Visualizing in Three-dimension

In 3D computer graphics, 3D modeling is the process of developing a mathematical representation of any surface of an object in three dimensions. 3D rendering displays objects as two-dimensional images based on a computer simulation of physical phenomena.

2.4.2.1 Volume Ray Casting

One of the most standard ways for direct volume rendering is ray casting. Ray casting is to directly render every voxel with RGBA transfer function (RGB color and alpha transparency) from a fixed point of the camera. Figure 2.18 shows an example of volume ray casting rendering ex-vivo CMR images of left and right ventricles

with myocardial infarction. For the ex-vivo images, the background voxels (non-myocardium voxels) have low signal, and can be set to be transparent ($\alpha = 0$). For in-vivo imaging, myocardial contours can be delineated before volume rendering to separate the heart structure from the background signal.

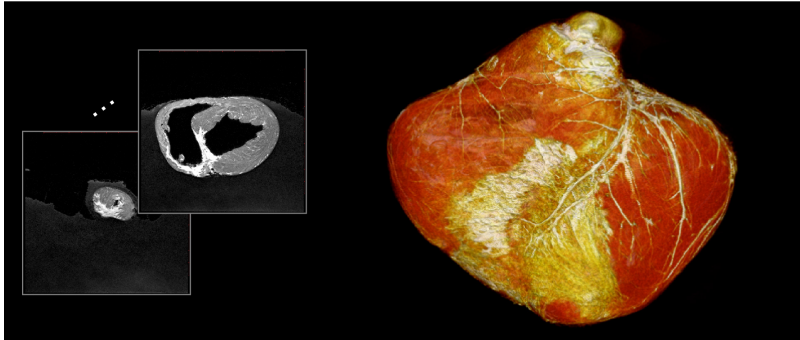


Figure 2.18: Volume ray casting of the heart with myocardial infarction.

2.4.2.2 Surface Rendering

A direct volume rendering can be a computationally exhausting process. Another way of rendering volume in 3D is the isosurface extraction. We can extract isosurfaces (surfaces with equal value) and render the surface using polygonal meshes (Figure 2.19). To render multiple tissue structures, we can render isosurface of each tissue into a single volume, and render different tissue into another volume. These multiple layers of volumes can be aligned and rendered in one view. Each surface-rendered volume can have its color and transparency. Isosurface rendering reduces computational power and allows separate control of each tissue structure.

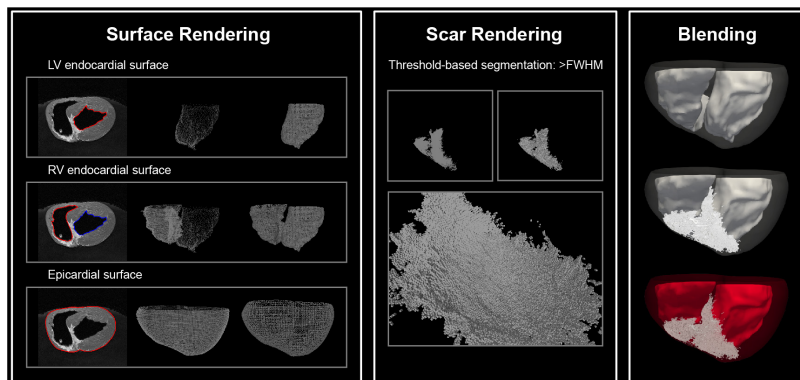


Figure 2.19: Isosurface rendering of myocardial surface and the scar.

2.5 PRE-CLINICAL VALIDATION

In this thesis, pre-clinical animal studies were performed to validate the hypotheses in a controlled experimental setup.

2.5.1 *Animal Model of Human Disease*

Human ventricular tachycardia (VT) after myocardial infarction usually occurs due to subendocardial reentrant circuits originating in scar tissue which borders surviving myocardial bundles. We used a well-characterized swine model of scar-related subendocardial reentrant VT, which serves as the basis for investigation in the physiology and therapeutics of humanlike post-infarction reentrant VT (Figure 2.20).

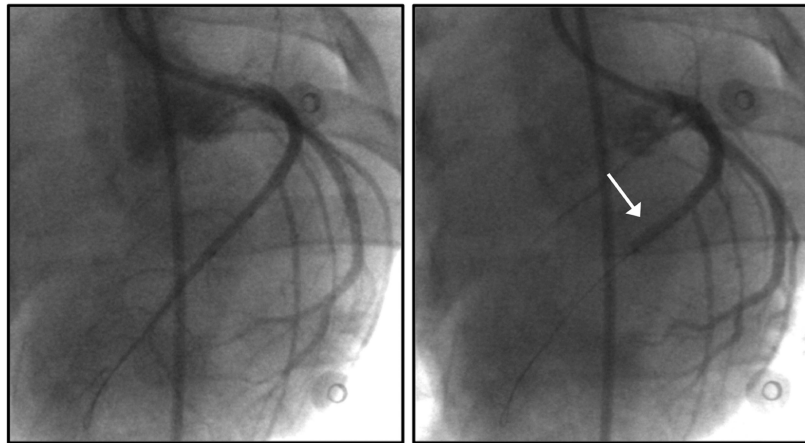


Figure 2.20: Swine model of myocardial infarction via percutaneous balloon occlusion of the left anterior descending (LAD) coronary artery [119].

2.5.2 *In-vivo and Ex-vivo CMR Imaging*

2.5.2.1 *In-vivo CMR Imaging*

For in-vivo imaging, the animal was put under anesthesia, and ventilated with oxygen (Figure 2.21). We located the animal on the scanner bed and placed a cardiac coil on the chest. We monitored ECG and oximetry throughout the scan. For all scans, we performed cardiac gating. For breath-hold scans, we manually paused the ventilator during the breath-hold periods and proceeded the imaging.

2.5.2.2 *Ex-vivo CMR Imaging*

Ex-vivo imaging was performed to provide detailed high-resolution reference scar images. To administer contrast in the scar tissue, we



Figure 2.21: A swine research subject undergoing a cardiac MRI scanning under general anesthesia [117].

performed intravenous (IV) injection of 0.2 mmol/kg gadobenate dimeglumine, 15 minutes before animal euthanasia. Then, the heart was harvested and excised along the atrioventricular groove. As the ex-vivo heart has no blood filled in anymore, there is no volume in the ventricles. To maintain the geometry of the heart, the left and right ventricular shapes were 3D printed using previously scanned in-vivo images, and was inserted into ventricles before ex-vivo imaging (Figure 2.22). It allows the geometry of ex-vivo images to match well with the one from in-vivo images. Both clay and kinetic sand also offers flexible filling of ventricles and maintain the basic geometry while providing a low signal for CMR imaging. We placed the geometry-maintained ex-vivo heart in a plastic box and filled up Saline to cover the entire heart to minimize air-water interface artifacts while imaging. For scar imaging, we performed T₁-weighted imaging with an isotropic spatial resolution of 0.4mm.



Figure 2.22: 3D printed models of left and right ventricles inserted in the ex-vivo heart to maintain the basic geometry.

2.5.3 Histopathological Analysis

Histopathological analysis was performed to validate the findings in the imaging studies. After the ex-vivo CMR study, the hearts were placed in a 10 % buffered formalin solution for >1-week for tissue fixation, then serially sectioned parallel to the atrioventricular groove into 5-mm thick slices starting from the apex. Tissue samples were paraffin-embedded using large tissue histology cassettes. We further sectioned the tissue with a 5- μ m thickness, and stained the slides with Masson's trichrome for collagen detection. The slides were then digitized. [Figure 2.23](#) shows CMR imaging slices identified and compared to pathological and histological regions of interest of the heart.

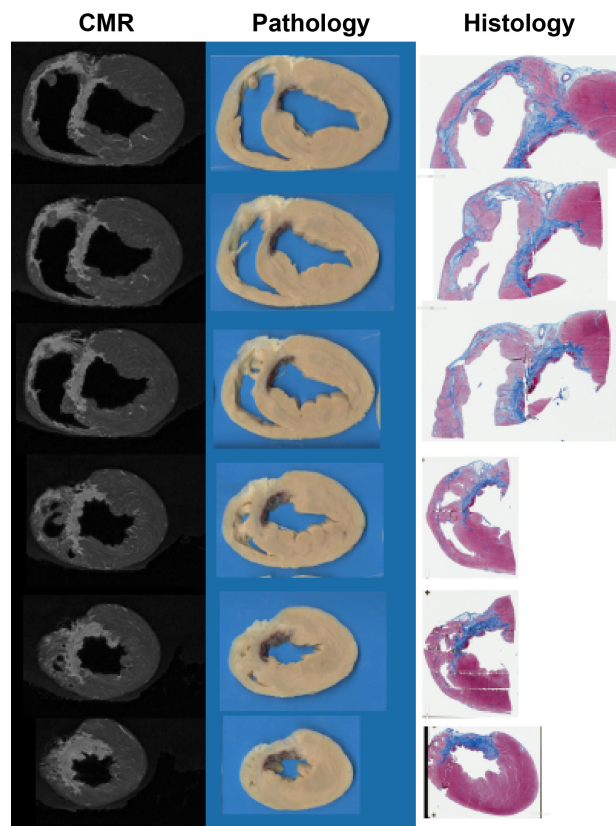


Figure 2.23: CMR and histopathological images of a swine heart with myocardial infarction.

Part II

METHODS AND RESULTS

CMR IMAGING FEATURES AND CONDUCTION VELOCITY

3.1 INTRODUCTION

Cardiovascular magnetic resonance (CMR) late gadolinium enhancement (LGE) imaging is the gold standard for visualizing and identifying the extent, volume, and characteristics of myocardial scar in patients with prior myocardial infarction (MI) [31, 51]. The extent of LGE has been reported as a predictor for the arrhythmogenic substrate, adverse outcome, and appropriate implantable cardioverter defibrillator therapy in patients with ventricular arrhythmias [52, 94, 128]. The presence of the scar border zone, as defined by LGE, correlates with inducibility and mortality in ventricular tachycardia (VT) [14, 19, 21, 83, 88, 104, 110]. Studies have also shown that decreased relative wall thickness is associated with an increased risk of ventricular arrhythmias [58]. The association between the extent and the heterogeneity of myocardial fibrosis and decreased wall thickness with adverse outcomes in patients with arrhythmias [14, 19, 21, 31, 51, 52, 58, 83, 86, 88, 94, 104, 110, 128] are likely to reflect the importance of myocardial tissue structure on conduction of the heart.

Conduction velocity (CV) describes the speed and direction of cardiac electrical propagation within the myocardium and is an important property that contributes to the substrate arrhythmogenicity [100]. Slow conduction regions are necessary for the initiation and maintenance of re-entrant arrhythmias [5, 64–66, 105], and are therefore critical components of pathological re-entrant circuits. Re-entry mechanism is the main cause of monomorphic VT observed in tissue damaged by prior MI, and is a major cause for sudden cardiac death.

Various factors can affect CV in post-infarction ventricular tissue. Myocardial fibrosis reduces connectivity in myocyte-myocyte and myocyte-fibroblast couplings and therefore slows CV [32, 36, 59, 66]. Tortuous or ‘zig-zag’ conduction through isolated bundles of surviving myocytes in and around infarcted regions represent a structural mechanism responsible for slow conduction in the scarred ventricular myocardium [35, 125]. Wavefront curvature also affects CV; A convex wavefront propagates more slowly than a planar wavefront due to a source-sink mismatch [93], a key mechanism responsible for the reduced CV observed around the infarcted border zone [12, 93, 105, 130]. Other factors including differences in transmembrane currents in the infarcted border zone resulting in excitability changes at a cellular

level causing a slower upstroke of the cardiac action potential, may also contribute to local differences in CV [63].

Due to the importance of cardiac conduction properties in determining the arrhythmogenicity of tissue, various studies have assessed CV [100]. Prior investigators have directly estimated CV by using regularly spaced microelectrode arrays on exposed and smooth (usually epicardial) surfaces, where the distance between two microelectrodes is defined and the activation time is manually measured [33, 37]. CV can also be estimated in experimental settings using optical mapping systems [90, 126]. In the clinical setting, CV can be estimated based on planar wavefront propagation by applying a fit model based on the neighboring electrodes' spatial locations and local activation times. The fitting can be performed either based on a pre-defined arrangement of measurement points depending on catheter design [27, 82] or more generalizable techniques such as polynomial surface fitting [16, 74] or triangulation [72, 101, 127]. However, these CV measurements are intrinsically invasive since the electrodes require direct myocardial contact. Non-invasive techniques to identify regions of altered myocardial CV may offer a valuable tool for pre-procedural planning and identification of the arrhythmogenic substrate, thereby reducing procedural duration and complexity.

The association between LGE and CV has been studied in the human left atrium [26, 60], where a negative association between LGE signal intensity and CV was shown during the sinus rhythm when clustered by patient, and adjusted for left atrial wall thickness [60]. In the left ventricle (LV), LGE and wall thickness was reported to independently be associated with local intracardiac electrogram (EGM) duration and deflections, suggesting slower conduction in regions with higher scar transmural thickness [85]. However, the association between CV and LGE or wall thickness in the LV has not yet been studied. Finally, although prior studies have reported association between LGE heterogeneity or wall thickness with adverse outcomes for arrhythmia [14, 19, 21, 83, 88, 104, 110], no study has investigated the direct association between CV and LGE heterogeneity or wall thickness gradient with CV.

In this study, we sought to investigate the association between CV and LGE, wall thinning, LGE heterogeneity, and wall thickness gradient in a swine model of healed anterior MI. With its ability to visualize and quantify myocardial fibrosis and wall thickness, CMR may offer a non-invasive imaging surrogate for identifying areas of reduced local CV and therefore arrhythmogenic substrate after MI.

3.2 METHODS

3.2.1 *Animal Study*

The protocol was approved by the Institutional Animal Care and Use Committee (IACUC) and conformed to the Position of the American Heart Association on Research Animal Use. All experiments were performed under general anesthesia with isoflurane inhalation (1.5-2.5%) and mechanical ventilation (12-16 breaths/min with tidal volumes between 300-400ml), and animals were euthanized with pentobarbital sodium. The animal study outline is summarized in [Figure 3.1](#). In brief, ischemia-reperfusion MI was created by 180-minute balloon occlusion of the left anterior descending (LAD) coronary artery. Following a 9-week recovery, each animal underwent in-vivo CMR. Zero to five days following in-vivo CMR, invasive electrophysiology (EP) studies were performed as described below to collect activation maps during RV apical pacing at cycle length of 400 ms. Inclusion criteria for enrollment into the study was defined as animals who completed the EP study protocol, and was set before the study. CMR and electroanatomic mapping (EAM) data were processed to extract CMR derived tissue characteristics and to estimate CV. CMR and EAM data were spatially registered to study their associations.

3.2.2 *Animal Model*

Five male and three female Yorkshire pigs from Parsons (3.5 – 4 months old; 35 – 40 kg) underwent balloon occlusion of the mid-LAD artery as previously described [[102](#), [123](#)]. One female pig died at 15 days post-MI during its first cardiac MR scan from an anesthetic-related bradycardic arrest and was excluded from the study. An angioplasty balloon was inflated in the mid-LAD under fluoroscopic guidance. After 180-minutes, the balloon was deflated and withdrawn, in order to create an ischemia-reperfusion mediated MI. Animals were treated with 800 mg twice daily oral amiodarone for 4 days following MI which was then decreased to 400 mg once daily throughout the survival period to minimize the risk of death from spontaneous ventricular arrhythmias. To establish the baseline CV, two healthy control animals of comparable weights underwent the EP study using the identical protocol – one animal was medicated with oral amiodarone as per infarcted animal protocol (control_{medicated}), and another animal was not medicated (control_{non-medicated}).

3.2.3 *CMR Imaging*

CMR imaging was performed using a 1.5T scanner (Philips Achieva, Best, The Netherlands) with a 32-element cardiac phased-array receiver

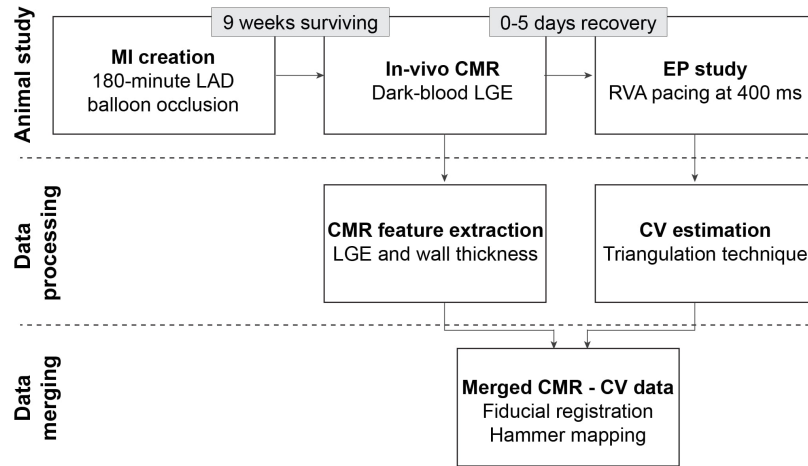


Figure 3.1: Study flowchart. Animal model of healed myocardial infarction (MI) was created by mid left anterior descending (LAD) coronary artery ischemia-reperfusion. After 9 weeks of surviving periods, in-vivo cardiovascular magnetic resonance (CMR) was performed. After 0-5 days of recovery, an electrophysiology (EP) study was performed and electroanatomic maps were acquired while pacing from the RV apex (RVA) at cycle length of 400 ms. CMR and EP data were processed to extract CMR features including late gadolinium enhancement (LGE) and left ventricular wall thickness. Conduction velocity (CV) was estimated using triangulation technique. CMR and CV data were spatially registered to study their associations.

coil. Scar imaging was performed using a dark-blood LGE sequence with an optimized joint inversion preparation and T2 magnetization preparation to simultaneously suppress myocardial and blood signal and enhance blood-scar contrast [89, 115]. Imaging was performed 15-25 minutes after injection of 0.15–0.2 mmol/kg gadobenate dimeglumine (MultiHance; Bracco Imaging, Milan, Italy). A respiratory navigator with an adaptive acquisition window [30] was used for prospective motion correction. Imaging was performed in short-axis with the following parameters: gradient echo imaging sequence; spatial resolution = $1.3 \times 1.3 \times 1.3 \text{ mm}^3$; field-of-view = $320 \times 335 \times 90 \text{ mm}^3$; TR/TE/flip angle = $2.6/1.3\text{ms}/55^\circ$; sensitivity encoding rate = 2; centric phase-encoding order.

3.2.4 Electrophysiology Study

EP study was performed using the CARTO₃ EAM system (Biosense Webster, Diamond Bar, California, USA) and standard electrophysiological recording system (LabSystem Pro, Bard, Lowell, Massachusetts, USA). 12 lead surface electrocardiogram (ECG) was recorded throughout all cases. High frequency (30 Hz) and low frequency (0.5Hz)

filters were applied to all surface ECG signals. Filters were applied to unipolar (low frequency filter: 0.5Hz; high frequency filter 250Hz) and bipolar (low frequency filter: 30Hz; high frequency filter: 250Hz) intracardiac EGMs prior to analysis. A sensor-enabled Thermocool (Biosense-Webster) ablation catheter was advanced to the aorta via the right femoral arterial sheath and used to acquire the aortic root and coronary ostia geometry prior to gaining retrograde LV access across the aortic valve. LV endocardial geometry was acquired using the fast anatomic mapping function within CARTO.

LV endocardial activation maps were acquired using a 5-spline 20-electrode mapping catheter (Pentaray, Biosense-Webster), with 1mm electrodes and 2-6-2mm electrode spacing introduced into the LV using a retrograde approach while pacing from the RV apex at a cycle length of 400ms. A reference bipolar electrode pair was selected on the RV catheter and activation times of each acquired LV activation point assigned relative to the reference EGM. Individual activation times were automatically assigned within the EAM at the point of the highest rate of negative deflection of the bipolar EGM ($-dV/dt_{max}$). Individual activation times were manually reviewed and reassigned following review of bipolar and unipolar EGM when necessary. Maps were considered complete when the point density allowed interpolation to be limited to <15 mm in normal region and <5 mm in regions of low bipolar voltage <1.5 mV [122]. One animal did not complete the study protocol due to the repeated and prolonged episode of VT which resulted in metabolic state deterioration and was not recovered, and was excluded from the study.

3.2.5 Local Conduction Velocity Estimation

CV was estimated based on triangulation techniques [100, 101] (Figure 3.2A). We used a triangular mesh of local activation time (LAT) exported from the EAM system, after manual annotation as needed. LAT maps were automatically generated within CARTO using interpolation that was limited to a maximum of 15 mm from an acquired data point. An edge collapse decimation was performed to simplify and re-triangulate meshes to improve triangular mesh quality. Triangulation techniques are based on the rules of trigonometry, and the coordinates of three points and their activation times were used to estimate the average CV within the triangle. When a wavefront is approximated as locally planar, from the earliest activation point to the next two points, the conduction speed and the direction is decided based on the activation time of the remaining two points. For example, when the earliest activation point is p , and the other points are q and r , the activation time difference between p to q is t_{pq} , and the orthogonal

distance between p to q can be notated as $acosa$. Then the CV can be defined as follows:

$$v = \frac{acosa}{t_a}$$

Likewise, for the third point, the activation time difference between p to r can be noted as t_b , and the orthogonal distance separating the points can be noted as $bcosb$, and the CV can be defined as follows as well:

$$v = \frac{bcosb}{t_b}$$

Constraints were imposed on distance between each pair of points ($1 < d < 20$ mm), the difference in activation times ($50 \text{ ms} > \text{LAT} > 1$ ms) to minimize measurement errors, and the ratio of circumcircle area to triangle area (< 10) to penalize elongated triangles [101].

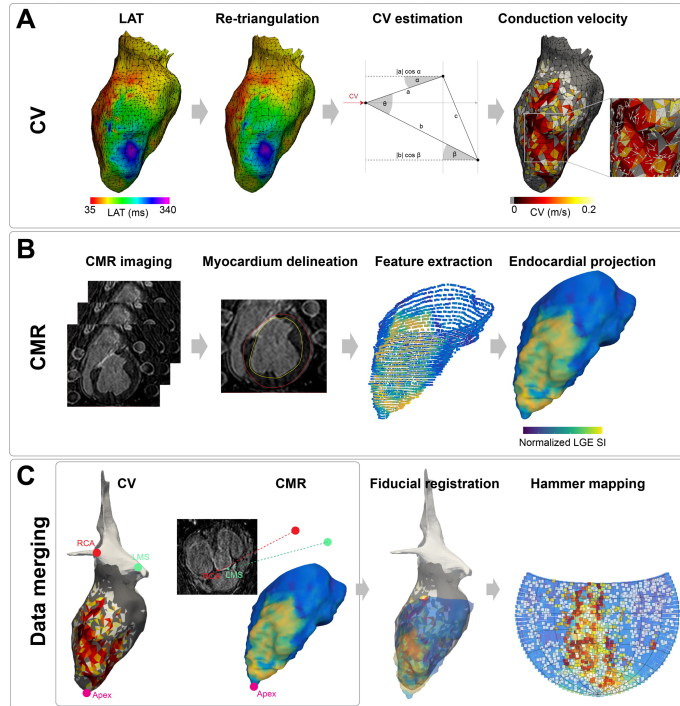


Figure 3.2: Analysis pipeline for investigating association between CMR features and conduction velocity (CV). (A) CV was estimated based on the local activation time (LAT) map using triangulation technique. (B) Endo-/epicardial contours were delineated to perform CMR feature projection on left ventricular endocardial surface model. (C) CV and CMR data were then spatially registered using fiducial registration based on right coronary artery (RCA), left main stem (LMS), and apex. CV and CMR data were then 2D projected on the semi-hemisphere map to minimize the surface area distortion using a Hammer mapping.

3.2.6 CMR Image Analysis

CMR images were processed to generate LV endocardial surface projected CMR imaging feature maps shown in Figure 3.2B. Endo- and epicardial contours were manually delineated by an experienced reader with guidance from cine balanced steady-state free-precession images. For each slice, the center of the endocardial contour was selected, and the equiangular chord lines were drawn from endo- to epicardial contours based on the number of pixels on the endocardial contour. Local tissue characterization parameters were defined for each chord line and were projected back the endocardial points. Endocardial points from each slice were merged into a single point cloud data set, and a Poisson surface reconstruction [95] was performed to reconstruct the LV endocardial surface. A second reader delineated endo- and epicardial contours independently to study the inter-observer reproducibility of the CMR measurements.

3.2.6.1 Late Gadolinium Enhancement

For LGE data, endocardial signal intensity was defined using subendocardial lines automatically identified as one third from endo to epicardial chord lines. The LGE signal intensity (SI) was then bimodal fitted, and LGE SI was normalized using the mean (μ_{remote}) and standard deviation (SD) (σ_{remote}) of remote regions, such that 0 in the normalized signal distribution was denoted as μ_{remote} and 1 as σ_{remote} . LGE+ was defined as any voxel with SI higher than $\mu_{remote} + 2\sigma_{remote}$ [61].

3.2.6.2 Myocardial Wall Thickness

Myocardial wall thickness was calculated as the Euclidean distance between endo- and epicardial contours of each chord line and was projected back to the endocardial points. wall thickness was presented as the absolute value in mm. wall thickness was bimodal fitted to define a region with wall thinning. Wall thinning+ was defined per chord line as wall thickness thinner than $\mu_{remote} - 2\sigma_{remote}$, such that 95% of the regions of remote wall thickness are thresholded.

3.2.6.3 LGE Heterogeneity

LGE heterogeneity was defined as the SD of the LGE SI of local neighbors in voxels that were within an Euclidean distance of 5 mm for each point, based on the minimal point density of EAM [122]:

LGE heterogeneity

$$= SD_{LGE_{5mm}} = \sqrt{\frac{\sum |LGE_{5mm} - \overline{LGE}_{5mm}|^2}{n}}$$

3.2.6.4 Wall Thickness Gradient

Wall thickness gradient was defined as the SD of the wall thickness of neighbors that were within an Euclidean distance of 5 mm for each point as follows:

Wall thickness gradient

$$= SD_{wall\ thickness_{5mm}} = \sqrt{\frac{\sum |wall\ thickness_{5mm} - \bar{wall\ thickness}_{5mm}|^2}{n}}$$

3.2.7 Data Registration

Imaging and EAM data were spatially aligned to study their associations as shown in Figure 3.2C. For spatial reference, the right coronary artery (RCA) ostium, left main stem (LMS) coronary artery ostium, and apex were manually marked both on EAM and CMR. Based on these three spatial reference points, fiducial registration was performed to align imaging and EAM data on the same spatial coordinates. Spatially registered EAM and imaging data were then 2D projected onto the semi-hemisphere map to minimize surface area distortion using Hammer mapping (Figure 3.2C) [112]. All hammer maps were orientated consistently with the RCA to apex axis along the center line. EAM and imaging data were projected onto the same hammer map, and for each data-containing EAM location, the closest point of imaging data was selected, and these spatially correlated values were paired for further analyses. All data processing analyses were performed using MATLAB (MathWorks, Natick, Massachusetts, USA) and Meshlab (Visual Computing Lab – ISTI – CNR, Rome, Italy) [24].

3.2.8 Statistical Analyses

Statistical analyses were performed to assess the association between CV and the other four parameters of 1) LGE, 2) wall thinning, 3) LGE heterogeneity, and 4) wall thickness gradient. First, we used the general linear models [118] to analyze data for each animal. In each of these models, we reported the model coefficient and its 95% confidence interval (CI). For LGE and wall thinning where we dichotomized the data, the model coefficient represents the estimated mean difference of CV for each category (+/-). For LGE heterogeneity and wall thickness gradient, the model coefficient represents the slope (the change of the mean of CV per unit change of LGE heterogeneity or wall thickness gradient). For the modeling of all animals, we used hierarchical models (linear mixed effects models) where we captured the within-animal repeated/longitudinal measurements by modeling the within-animal correlation using the compound symmetry structure

for the variance-covariance matrix of CV. The estimated variance-covariance parameters were used in the estimated fixed effects of the independent variables (LGE, wall thinning, LGE heterogeneity, wall thickness gradient) and the models yielded the estimated mean difference (LGE, wall thinning) or the slope (LGE heterogeneity, wall thickness gradient). All statistical analyses were performed using SAS software (SAS Institute Inc, Cary, North Carolina, USA).

3.3 RESULTS

Six swine (4 male; median 82.9 kg (range 74.9 – 93.1 kg)) with healed MI 63.5 (63 – 64) days after infarction, and two healthy control animals (control_{medicated}; control_{non-medicated}) were included in the study. The median number of data points per LV map was 296 (range 232 – 540) for post-MI animals, 265 for control_{medicated}, and 140 for control_{non-medicated}. EAM and CMR data were successfully registered, and examples of CV and CMR features including LGE, wall thickness, LGE heterogeneity, and wall thickness gradient are shown in [Figure 3.3](#). Scatter plots of CV vs. LGE, CV vs. wall thickness, CV vs. LGE heterogeneity, and CV vs. wall thickness gradient of all animals are shown in [Figure 3.4](#), where smoothing splines of each scatter plots are overlaid. Inter-observer reproducibility of CMR measurements were high with intraclass correlation coefficient of 0.95 for LGE scar volume, and 0.86 for LV wall thickness.

3.3.1 CV vs. LGE

Extensive antero-septal scarring was observed in all post-MI animals on in-vivo CMR. LGE distribution was mostly transmural with sparing of the sub-endocardium. Overall, the LGE scar volume was 24.0 ± 7.8 % of the entire LV myocardial volume. The endocardial LGE scar volume was 29.0 ± 10.7 % of the entire endocardial volume.

CV in post-MI animals was 0.38 ± 0.28 m/s in the presence of LGE (LGE+) and 0.58 ± 0.38 m/s in remote regions (LGE-) ([Figure 3.5](#); [Table 3.1](#)). CV was 0.65 m/s in the control_{medicated}, and 0.85 m/s in the control_{non-medicated}. For all animals, significantly lower CV was observed in LGE+ regions compared to LGE- regions with the estimated mean difference of -0.15 m/s (CI: -0.18, -0.13; $p < 0.001$, [Table 3.1](#)).

3.3.2 CV vs. Wall Thinning

The average LV wall thickness in CMR was 6.9 ± 1.1 mm with substantial wall thinning observed in scarred regions (minimum wall thickness 1.2 ± 0.7 mm). The average wall thickness was 5.1 ± 1.2 mm

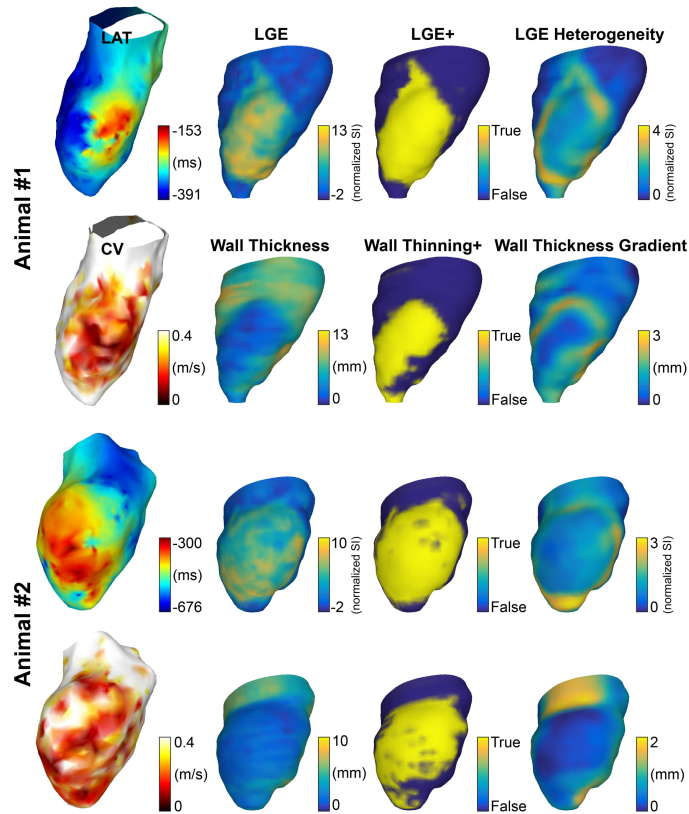


Figure 3.3: Conduction velocity (CV) and CMR features from 2 animals. CV was estimated based on the local activation time (LAT). CV and CMR data were registered in the same spatial coordinates. Slower CV was observed in the region of hyperenhancement on LGE and wall thinning. The pattern of CV was inhomogeneous throughout the scar with maximal slowing in the region of dense scar with higher LGE heterogeneity or wall thickness gradient.

in the region of hyperenhancement on LGE, and 7.4 ± 1.0 mm in the remote region.

CV in the post-MI animals were 0.38 ± 0.28 m/s in the presence of wall thinning (wall thinning+) and 0.55 ± 0.37 m/s in remote regions (wall thinning-) (Figure 3.6; Table 3.2). CV in the control_{medicated} was 0.65 ± 0.36 m/s, and 0.85 ± 0.45 m/s in the control_{non-medicated} (Figure 3.6). Significantly slower CVs were observed in the presence of wall thinning with the estimated mean difference of -0.07 m/s (CI: $-0.09, -0.04$; $p < 0.001$; Table 3.2).

3.3.3 CV vs. LGE Heterogeneity and Wall Thickness Gradient

LGE heterogeneity and CV were negatively associated, where CV decreases 0.02 m/s per unit increase in LGE heterogeneity (CI: -0.04 ,

	CV in LGE+ (m/s)	CV in LGE- (m/s)	Estimated Mean Difference (m/s)	95% CI	p-value
All Animals	0.38±0.28	0.58±0.38	-0.15	(-0.18, -0.13)	<0.001
Animal #1	0.33±0.24	0.59±0.37	-0.09	(-0.14, -0.03)	<0.001
Animal #2	0.35±0.29	0.58±0.37	-0.21	(-0.28, -0.13)	<0.001
Animal #3	0.35±0.28	0.58±0.40	-0.23	(-0.28, -0.19)	<0.001
Animal #4	0.43±0.27	0.57±0.33	-0.03	(-0.10, 0.03)	0.36
Animal #5	0.43±0.26	0.58±0.38	-0.16	(-0.24, -0.09)	<0.001
Animal #6	0.46±0.30	0.65±0.43	-0.15	(-0.21, -0.09)	<0.001

Table 3.1: Estimated mean differences in CV between LGE+ and LGE-, 95% confidence interval (CI), and p-value of general linear modeling and of multilevel model of all animals and each individual animal. The model: $CV = \beta_0 LGE + \beta_1 wall\ thinning + \epsilon$.

	CV in wall thinning+ (m/s)	CV in wall thinning- (m/s)	Estimated Mean Difference (m/s)	95% CI	p-value
All Animals	0.38±0.28	0.55±0.37	-0.07	(-0.09, -0.04)	<0.001
Animal #1	0.30±0.23	0.48±0.35	-0.13	(-0.18, -0.07)	<0.001
Animal #2	0.37±0.32	0.56±0.37	-0.04	(-0.13, 0.04)	0.32
Animal #3	0.37±0.31	0.50±0.37	-0.01	(-0.07, 0.05)	0.69
Animal #4	0.37±0.22	0.58±0.33	-0.18	(-0.26, -0.11)	<0.001
Animal #5	0.46±0.29	0.56±0.37	0.02	(-0.05, 0.10)	0.52
Animal #6	0.43±0.29	0.62±0.41	-0.12	(-0.19, -0.05)	<0.001

Table 3.2: Estimated mean difference in CV between wall thinning+ and wall thinning-, 95% confidence interval (CI), and p-value of general linear modeling and of multilevel model of all animals and each individual animal. The model: $CV = \beta_0 LGE + \beta_1 wall\ thinning + \epsilon$.

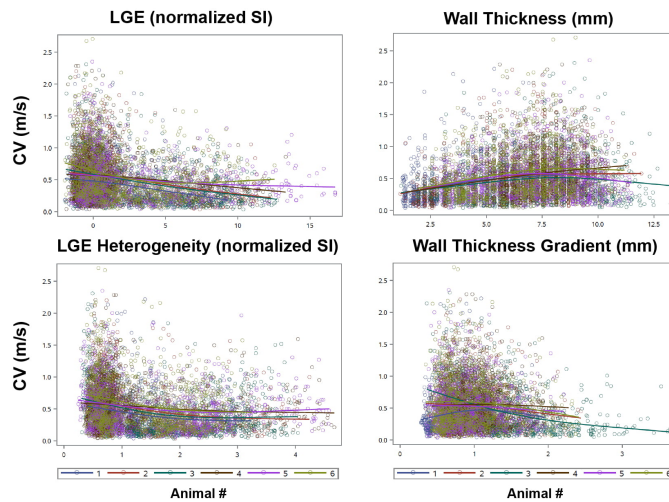


Figure 3.4: Scatter plots of LGE, wall thickness, LGE heterogeneity, and wall thickness gradient vs. conduction velocity (CV) of all 6 animals. Smoothing splines of each animal are overlaid on the scatter plots.

-0.01; $p < 0.001$, Table 3.3). A negative relationship between CV and wall thickness gradient was also observed, where CV decreases 0.05 m/s per unit increase in wall thickness gradient (CI: -0.07, -0.03; $p < 0.001$, Table 3.4). The pattern of the CV was inhomogeneous throughout the scar, and the maximal slowing occurred in the area of dense scar with higher LGE heterogeneity or wall thickness gradient.

3.4 DISCUSSION

We investigated the association between EAM defined CV with CMR defined LGE and wall thickness in a swine model of healed LV infarction. We found that during steady state pacing from the RV apex 1) CV is lower in LGE+ regions, 2) is lower in regions of wall thinning, and 3) is lower in regions with high LGE heterogeneity and steeper wall thickness gradient. CV exhibited inhomogeneous pattern with maximal slowing in the region of dense scar with higher LGE heterogeneity or wall thickness gradient.

Previous studies have reported associations between the extent and heterogeneity of LGE/ wall thickness and adverse outcomes in patients with arrhythmias [14, 19, 21, 31, 51, 52, 58, 83, 88, 94, 104, 110, 128]. Our study adds valuable insights by confirming a direct association between LGE/wall thickness with CV, highlighting an important mechanism by which CMR-defined tissue structural characteristics may promote arrhythmogenesis. This contributes to a deeper understanding of the previously reported association between the extent or heterogeneity of LGE/ wall thickness and outcomes in patients with arrhythmias. CMR may offer a valuable imaging surrogate for

	LGE Heterogeneity (normalized SI)		
	Slope	95% CI	p-value
All Animals	-0.02	(-0.04, -0.01)	<0.001
Animal #1	-0.03	(-0.07, 0.01)	0.18
Animal #2	-0.06	(-0.10, -0.02)	<0.001
Animal #3	0.02	(-0.01, 0.04)	0.27
Animal #4	-0.01	(-0.04, 0.02)	0.39
Animal #5	-0.05	(-0.09, -0.02)	0.01
Animal #6	-0.06	(-0.10, -0.01)	0.02

Table 3.3: The regression slope, 95% confidence interval (CI) and p-value of generalized linear modeling of CV vs. LGE heterogeneity of multilevel model of all animals and each individual animal. The model: $CV = \beta_0 LGE + \beta_1 LGE \text{ heterogeneity} + \beta_2 \text{ wall thickness} + \beta_3 \text{ wall thickness gradient} + \varepsilon$.

	Wall thickness gradient (mm)		
	Slope	95% CI	p-value
All Animals	-0.05	(-0.07, -0.03)	<0.001
Animal #1	0	(-0.07, 0.06)	0.94
Animal #2	0.01	(-0.06, 0.08)	0.84
Animal #3	-0.18	(-0.23, -0.13)	<0.001
Animal #4	0.05	(-0.01, 0.12)	0.11
Animal #5	0.05	(-0.03, 0.13)	0.26
Animal #6	-0.05	(-0.12, 0.02)	0.13

Table 3.4: The regression slope, 95% confidence interval (CI) and p-value of generalized linear modeling of CV vs. wall thickness gradient of multilevel model of all animals and each individual animal. The model: $CV = \beta_0 LGE + \beta_1 LGE \text{ heterogeneity} + \beta_2 \text{ wall thickness} + \beta_3 \text{ wall thickness gradient} + \varepsilon$.

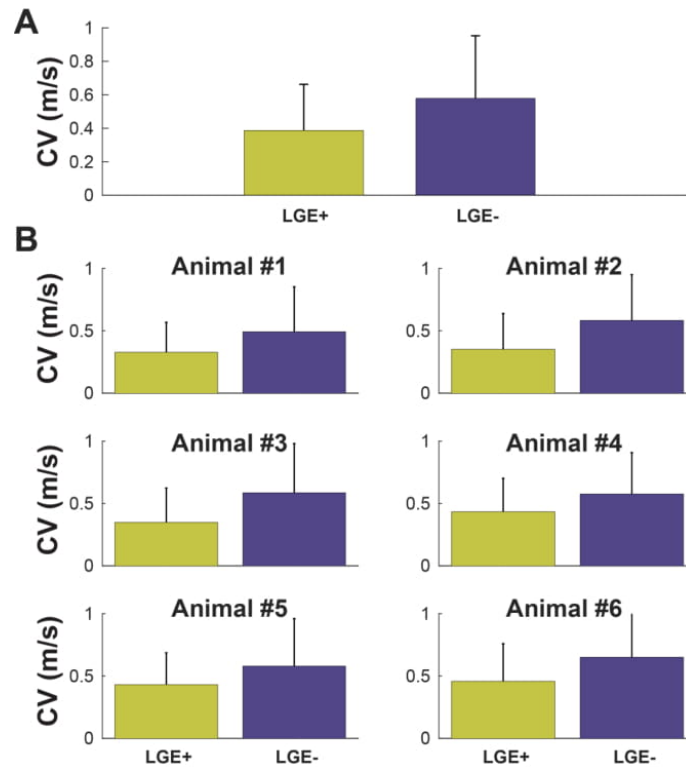


Figure 3.5: Conduction velocity (CV) in the presence and absence of LGE averages over all animals (A) and for each individual animal (B). Slower CV was observed in the areas of hyperenhancement on LGE (LGE+).

estimating CV, which may support non-invasive identification of the arrhythmogenic substrate.

We found significantly slower CV in LGE+ regions, which is consistent with previous reports showing slower CV in the presence of myocardial fibrosis due to reduced connectivity in myocyte couplings [32, 36, 59, 66]. Our study shows significantly slower CV in the presence of wall thinning, which is as expected from previous studies using multidetector computed tomography [103]. Our result shows significantly slower CV in regions of high LGE heterogeneity, confirming slowing of CV in the presence of tissue heterogeneity, which is likely due to branching and merging bundles of surviving myocytes within infarcted tissue [125]. Regions of steeper wall thickness gradient primarily represent the infarct border zone where the wavefront curvature changes, resulting in significantly slower CV as previously reported [12, 93, 105, 130].

Our CVs are similar to those reported LV CV ranges in swine. In the swine ventricle, a range of 0.5 ± 0.02 m/s in the longitudinal direction to the fiber orientation, and 0.21 ± 0.01 m/s in the transverse direction

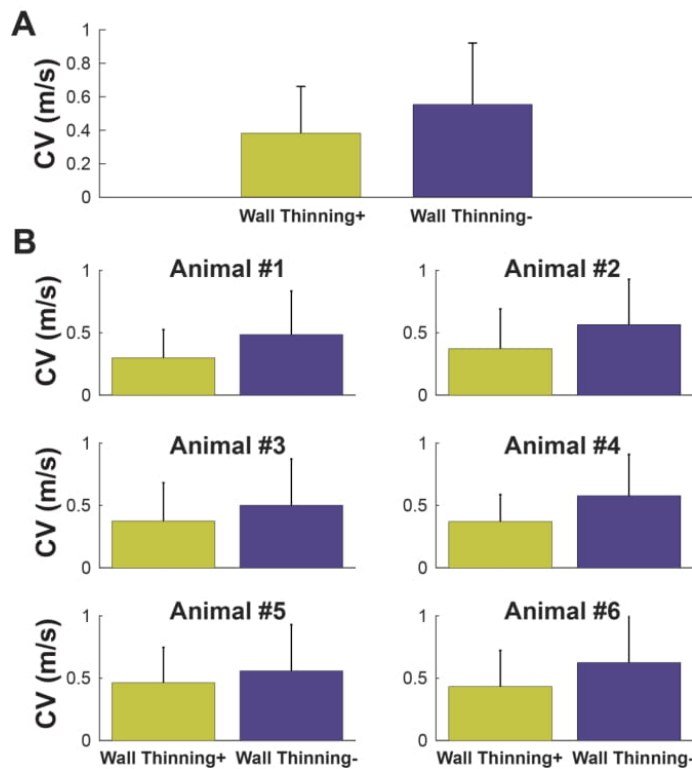


Figure 3.6: Conduction velocity (CV) in the presence and absence of wall thinning averages over all animals (A) and for each individual animal (B). Significantly slower CV was observed in areas of wall thinning+ compared to regions of wall thinning-.

was reported in Langendorff-perfused hearts where CV was measured with multiple terminal electrodes in epicardial surface of the anterolateral LV wall [68]. In another swine study during open-heart surgery, CV was estimated using polynomial surface fitting from 1.58 ± 0.83 to 1.82 ± 0.85 m/s depending on the sampling rate and activation threshold during sinus rhythm; and 0.70 ± 0.31 to 0.72 ± 0.34 m/s during pacing with cycle length of 300 ms from RV epicardium [74]. In a swine LV where CV was measured using high-resolution basket catheter and triangulation technique, absolute conduction velocities in the infarct and peri-infarct zone ranged from 0.10 m/s in areas of conduction block to 0.88 m/s in healthy myocardium and conduction bundles [78]. The CV estimated in our study was as low as 0.04 m/s in infarcted regions and 0.58 m/s in remote regions with pacing at cycle length of 400 ms, which lies within the expected range from the previous reports.

Our study has several limitations. The number of animals was small, though consistent with pre-clinical studies with large animal models. We did not study any factors that may contribute to functional aspects

of CV such as restitution properties. Using EAM, LAT was measured only for voltage amplitude $> 0.1\text{mV}$. We did not acquire identical number of data points in all our animals during EAM. Only one control animal underwent CMR imaging, although we did not observe either LGE or wall thinning in this animal.

3D STRUCTURAL MODELING OF THE ARRHYTHMOGENIC HEART

4.1 INTRODUCTION

The importance of the myocardial structure to understand arrhythmias has led cardiovascular magnetic resonance (CMR) to a promising technique to identify arrhythmogenic substrate. In infarct hearts, surviving tissues within the scar create heterogeneous tissue structures that cause slow conduction [42] and contribute to arrhythmogenesis. Late gadolinium enhancement (LGE) CMR allows accurate imaging of the extent and location of the myocardial infarction [75, 76] and can identify substrate in the scar-related ventricular tachycardia (VT). Studies have shown that scar border/ heterogeneous zone defined in LGE are associated with VT inducibility [106] and spontaneous ventricular arrhythmias [47, 98, 109].

Studies have identified conduction channels in CMR and correlated with those defined in electroanatomic mapping [6, 8, 11, 44, 45, 48, 91]. In in-vivo setting, multiple 2D slices of LGE images or endo-to-epi myocardial shells of LGE have been reviewed to identify conduction channels [8, 48, 91]. In ex-vivo setting, where higher-resolution imaging is possible, 3D reconstruction of the myocardial scar was performed to identify the conduction channels [11, 45]. However, these data are mainly based on the qualitative identification of the channels without streamlined workflow – different readers may identify conduction channels differently given the identical LGE scar/ myocardial images. Furthermore, histological validation in these data is limited.

Despite the potential of CMR for characterizing arrhythmogenic substrate, there is currently no standard approach to identify potential conduction channels. Therefore, in this study, we sought to develop a workflow to identify heterogeneous tissue (HT) channel, defined as narrow pathway consisting of healthy tissue, surrounded by scar or electrically non-excitable medium (e.g., fat, blood) and connected to healthy myocardium located within the areas of dense scar. The proposed technique was tested in high-resolution ex-vivo CMR images in 20 swine models with VT following myocardial infarction, and was validated in the electrophysiology study and histopathological analyses.

4.2 METHODS

We propose a technique for 3D HT channel detection based on the 3D structural modeling of the viable myocardium using high-resolution ex-vivo CMR [Figure 4.1A](#). We propose a workflow which takes segmentation of scar and myocardium from CMR images and perform an automated detection of HT channels [Figure 4.1B](#). In particular, we focus on detecting a macro-level HT channels. The overall processing pipeline consists of 3 steps, 1) 3D structural modeling of viable myocardium, 2) 3D skeletonization of viable myocardium, and 3) automated HT channel detection. The first step is to extract viable myocardium within the areas of dense scar where a cardiac electrical signal propagates. The second step is to simplify the geometry of the viable myocardium and enable automated characterization of the structures of the viable myocardium model. The last step is to identify HT channels based on the 3D structural properties of viable myocardium. Each step is detailed in the following sections.

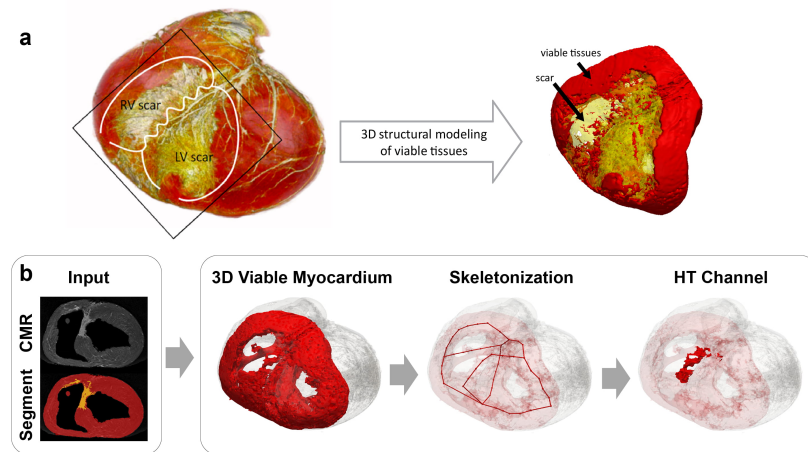


Figure 4.1: (A) A 3D volume rendered view of the 3D ex-vivo cardiovascular magnetic resonance (CMR) (yellow, scar; red, viable myocardium) and 3D structural model of viable myocardium in and around the scar generated with triangular surface meshes (yellow, scar; red, viable myocardium). (B) Proposed workflow for detection of a macro-level heterogeneous tissue (HT) channel uses scar and myocardium segmentation from CMR images as input and performs the following steps. Step 1: A 3D structural model of viable myocardium is generated from 3D CMR images to visualize the propagation pathway of a cardiac electrical signal. Step 2: 3D skeletonization of viable myocardium is performed to extract the simplified geometry of the viable tissue and automatize structural model characterization. Step 3: HT channels are automatically detected based on the 3D skeleton segmental analysis that identify HT channels with a high 3D structural complexity.

4.2.1 3D Structural Modeling

Viable myocardium in and around scar border plays important role in VT substrate. To explore structural characteristics of viable myocardium within the dense scar, we performed 3D structural modeling using high-resolution ex-vivo CMR images. An experienced reader performed segmentation of the scar and myocardium from CMR images [Figure 4.2A](#). A second reader independently performed scar/myocardium segmentation in the subset of 6 animals to assess inter-observer variability. As we are interested in extracting surviving myocardium near the scar, the first step was to perform the spatial growth operation to localize myocardial volume neighboring the scar [Figure 4.2B](#). We extracted any myocardium 30 mm isotropically around the scar as a good trade-off between skeletonization and discriminating normal myocardium. Segmented scar was then removed from the myocardial volume to extract only viable myocardium around the scar [Figure 4.2C](#). Before subtraction, scar volume was expanded 1mm isotropically to remove partial volume errors. The aforementioned processing was performed using the 3D Slicer [46].

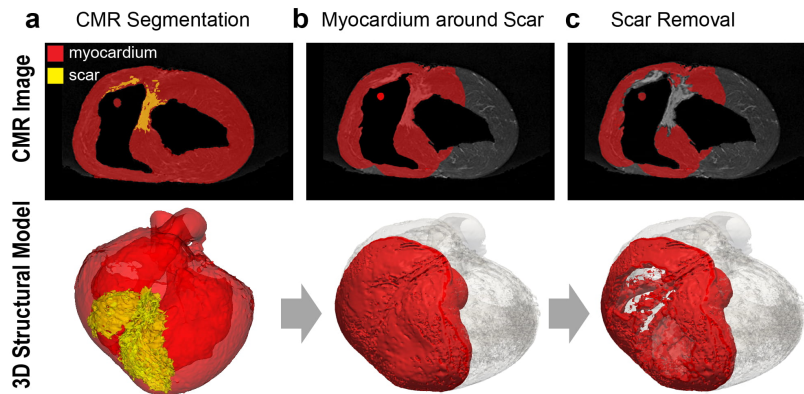


Figure 4.2: The proposed pipeline for building the 3D structural viable myocardium model. Upper panels show ex-vivo cardiovascular magnetic resonance images with overlaid myocardial segmentation (red), and the 3D structural model view of the corresponding segmentation (red) is represented in the lower panels. The whole ventricular 3D volume is shown in transparent gray. A) Scar and myocardium segmentation are used as an input to the system. B) Myocardium in and around the scar was extracted by expanding the 3D volume of the segmented scar to include neighboring myocardium. C) The scar was removed from the myocardium to exclude scarred tissues and to focus only on the viable myocardium where electrical signals propagate. Scar volume was expanded 1mm before subtracting to remove partial volume errors.

4.2.2 3D Skeletonization

3D skeletonization was performed to simplify the geometry of the complex 3D structures of viable myocardium and enable automated characterization of the 3D structural model. Before performing 3D skeletonization, the 3D structural model was first reduced to a smaller number of faces and vertices to reduce processing time and memory allocations [Figure 4.3A](#), which followed by removing duplicated faces. As we are interested in the connected pathway of the cardiac conduction through viable myocardium, any non-connected isolated myocardium of less than 100 triangles, which was typically considered as noise, was removed. A curved 3D skeleton was then extracted from the 3D viable myocardium model using a Point Cloud Skeletons via Laplacian-Based Contraction [[13](#), [28](#)]. 3D models were first normalized such that all models were located at the center of unit-sized cubes. The point cloud contraction was first performed to smooth and contract the 3D model into an approximate zero-volume mesh that abstracts the given shape and topology. The Laplacian-based maximal voluntary contraction (MVC) was first performed via local Delaunay triangulation [Figure 4.3B](#), which was further contracted using the Conformal Laplacian operation [Figure 4.3C](#). A final 3D skeletal graph consisting of points (nodes) and connecting lines (edges) was created by topological thinning [Figure 4.3D](#). During the skeletonization process, each segment of the structural model was contracted into nodes of the 3D skeletal graph, and the connection of each segment was represented as connecting edges of the 3D skeletal graph [Figure 4.3E](#).

4.2.3 Heterogeneous Myocardial Channel Detection

A skeletal graph enables automated characterization of structural properties of each segment and their connectivity. Anatomical, structural HT channel was defined as narrow pathway consisting of healthy tissue surrounded by scar or electrically non-excitable medium and connected to healthy myocardium. As the first step of HT channel detection, any narrow strip of tissue channel, which was defined as connected thin tissue segments, was detected. For each node of the skeletal graph, its orthogonal axis was computed based on the direction of its two adjacent nodes, and its cross-sectional plane was calculated. Skeletal node segments with a cross-sectional area less than 90 mm^2 were automatically detected to discriminate narrow channels from normal myocardium, as determined by the typical thin RV wall thickness ($[90 \text{ mm}^2] = [3 \text{ mm minimal RV wall thickness in normal [54, 124]] \times [30 \text{ mm neighboring volume expansion}]$) [Figure 4.4A](#). The minimal number of connected segments were set to 3 to minimize detection of any segments from the normal myocardium (LV, RV, and septum). As heterogeneous myocardium is often a mixture

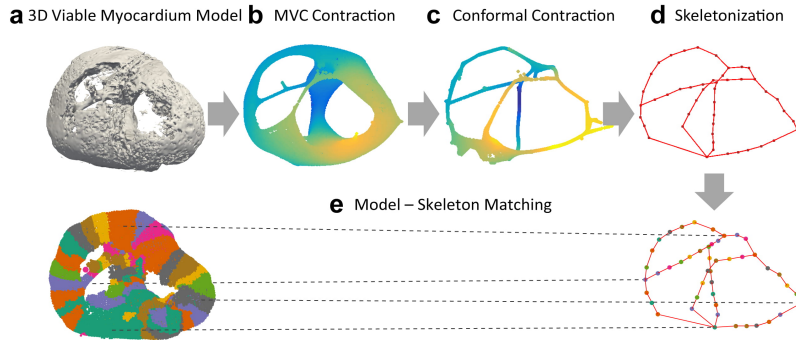


Figure 4.3: The proposed pipeline for 3D skeletonization to simplify viable myocardium geometry and enable automated quantification of the 3D viable myocardium model (A). Laplacian-based maximal voluntary contraction (MVC) (B) and conformal contraction (C) were performed to abstract and smooth the shape of the complex structures of the 3D model. 3D skeletonization was performed by topological thinning, resulting in a 3D skeleton with its simplified geometry represented by lines (D). During the skeletonization process, each segment of the structural model is contracted as a point on the 3D skeletal graph, so that the structural properties of the model can be automatically characterized using the skeletal graph (E).

of preserved and scarred tissue, it forms a complex 3D structure compared to smooth normal tissue. Therefore, as a second step, viable myocardial channels with high 3D structural complexity were detected. Structurally complex objects require a higher number of faces to model the finer details. Therefore, we defined HT index as the number of triangular faces per unit length (mm) [Figure 4.4B](#). The HT index was set to 26 to discriminate smooth vs. heterogeneous myocardial tissue channels. The proposed algorithm was implemented in MATLAB (MathWorks, Natick, MA).

4.2.4 Animal Study

Animal study was performed to test the proposed techniques in the animal model with scar-related VT using high-resolution ex-vivo CMR images in 20 animals. The study was carried out in strict accordance with the recommendations in the Guide for the Care and Use of Laboratory Animals of the National Institutes of Health. The protocol was approved by the Institutional Animal Care and Use Committee (Protocol Number: 100-2014). All experiments were performed under general anesthesia with isoflurane inhalation (1.5-2.5 %) and mechanical ventilation (12-16 breaths/min with tidal volumes between 300-400 ml), and animal was euthanized with pentobarbital sodium.

The twenty pigs (30 – 35 kg) underwent 180-minute balloon occlusion of the mid-left anterior descending (LAD) artery as previously

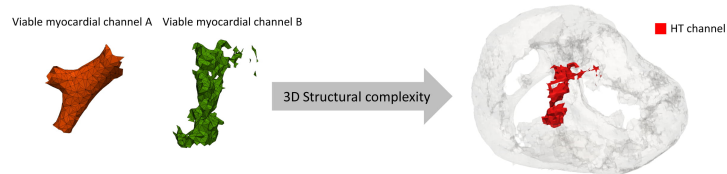
a Skeleton Segmental Analysis**b** HT channel Detection

Figure 4.4: The proposed algorithm for automated heterogeneous tissue (HT) channel detection. The algorithm consists of two steps: 1) skeleton segmental analysis of the cross-sectional area to detect narrow and connected segments to identify viable myocardial channels, and 2) HT channel detection based on the 3D structural complexity to detect HT channels that are known to cause slow conduction. A) For each skeletal point, its orthogonal axis is computed based on its two adjacent nodes, and the cross-sectional plane is calculated. Any connected segments with a cross-sectional area less than 90 mm² are automatically detected to identify narrow strips of tissue. B) Detected myocardial channels are further evaluated for tissue heterogeneity based on the 3D structural complexity defined as the unit number of triangular faces. Any myocardial channel with a heterogeneity index (unit number of triangular faces) greater than 26 was identified as an HT channel.

described [120, 129]. An angioplasty balloon was inflated in the mid-LAD under fluoroscopic guidance. After 180 minutes the balloon was deflated and withdrawn, in order to create an ischemia-reperfusion mediated myocardial infarction.

4.2.5 CMR Imaging

CMR imaging was performed using a 1.5T scanner (Philips Achieva, Best, The Netherlands) with a 32-element cardiac phased-array receiver coil. Upon completion of the electrophysiology study, the animal was euthanized and the heart was explanted. Intravenous injection of 0.15-0.2 mmol/L gadobenate dimeglumine was performed 15 minutes before euthanasia. Atria was excised and ventricles were filled with kinetic sand to maintain basic geometry. Scar imaging was performed using high-resolution 3D gradient echo sequence. Typical imaging parameters were as follows: spatial resolution = $0.4 \times 0.4 \times 0.5$ mm³;

FOV = $130 \times 130 \times 100$ mm³; TR/TE = 16/7.4 ms; flip angle = 25°; low-high phase-encoding order; signal averaging = 4.

4.2.6 *Electrophysiology Study*

All animals underwent electrophysiology study after an 8-week survival period. Percutaneous femoral arterial and venous access were obtained. Under fluoroscopic guidance, a 6Fr pentapolar diagnostic catheter (Bard EP, Lowell, MA) was placed in the right ventricular (RV) apex to allow pacing. The proximal electrode was positioned in the inferior vena cava and served as an indifferent unipolar electrode. Electrical stimulation was performed from the RV apex using a current strength twice the capture threshold and pulse width of 2 ms. Programmed ventricular stimulation at paced cycle lengths of 600 and 400 ms with 1-4 extra-stimuli down to ventricular effective refractory period were performed to induce VT. If electrical stimulation from the RV apex failed to induce VT, stimulation was repeated from the LV endocardium and epicardium near the infarct region until the animal was inducible. Animals were only considered non-inducible if VT could not be induced despite stimulation from all sites. Sustained monomorphic VT was defined on 12-lead ECG as the tachycardia lasting >30 seconds with a consistent morphology. A macroscopic localization of the site of origin of VT was identified using a surface 12-lead ECG [70, 71] to compare with the region of detected HT channels. Furthermore, activation mapping during VT was attempted to identify detailed site of origin of VT.

4.2.7 *Histopathological Analysis*

After the ex-vivo CMR study, the hearts were placed in a 10 % buffered formalin solution for >1-week for tissue fixation, then were serially sectioned parallel to the atrioventricular groove into 5-mm thick slices starting from the apex. Tissue samples were paraffin embedded by using large tissue histology cassettes. Tissue was sectioned with a 5- μ m thickness, and slides were stained with Masson's trichrome for collagen detection, and was digitized. The corresponding CMR slides were identified, and compared to the histological regions of infarction for characterization of myocardial fibrosis and surviving tissue in the region of detected HT channels.

4.2.8 *Statistical Analyses*

To test the null hypothesis that there are no non-random associations between VT inducibility and the existence of the detected HT channel, Fisher's exact test was performed. A result was considered statistically significant at $P < 0.05$.

4.3 RESULTS

4.3.1 *Animal Model*

All animals had extensive anterior-septal LGE in 8 weeks-post myocardial infarction. VT was inducible in 15 animals. The remaining 5 post-infarct animals were non-inducible.

4.3.2 *3D Structural Modeling and HT Channel Detection*

The 3D structural modeling enabled visualization of surviving myocardium in and around the scar region in a true 3D manner. Examples of 3D structural models are shown in animals with inducible VTs [Figure 4.5A](#) and non-inducible VTs [Figure 4.5B](#).

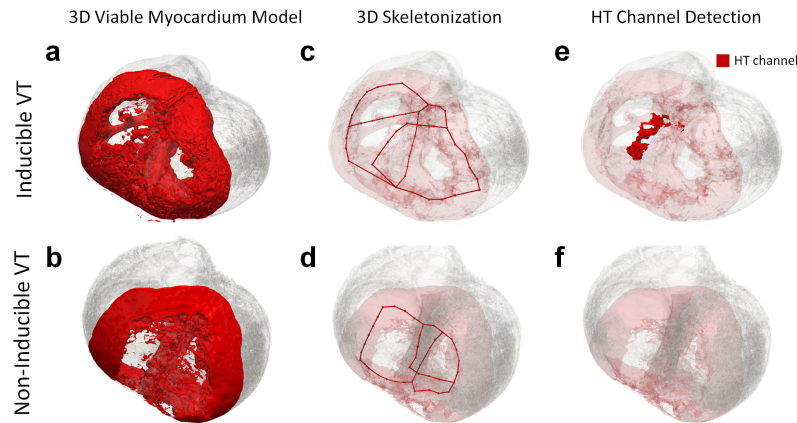


Figure 4.5: Example of 3D structural viable myocardium models, 3D skeletons, and detected heterogeneous tissue (HT) channel in an animal with an inducible ventricular tachycardia (VT) and an animal with a non-inducible VT. The 3D viable myocardium model was able to represent surviving and viable myocardium in and around the scar in a true 3D manner for each case (A-B). 3D skeletonization enabled simplification of the geometry of the viable myocardium (C-D). An HT channel was detected in the animal with the inducible VT (E), whereas it was not detected in the animal with the non-inducible VT (F).

The skeletal graph simplified the complex 3D structure and enabled quantification of structural properties of the 3D model which allowed automated identification of the HT channels. [Figure 4.5C-D](#) show the results of 3D skeletonization, represented by red lines in all animals.

HT channels were detected in all inducible VT animals and highlighted in red ([Figure 4.5E](#)), whereas such structure was mostly not detected in the animal with non-inducible VT ([Figure 4.5F](#)). The inter-

observer agreement was strong with Dice index of scar segmentation between two independent readers of 0.79 ± 0.07 .

4.3.3 HT Channel and VT Inducibility

In 15 animals with inducible VT, 22 viable myocardial channels were detected (an average of 1.5 per animal). Among the 22 viable myocardial channels, 16 myocardial channels were detected as heterogeneous myocardial channels (average of 1.1 per animal). In 5 animals with non-inducible VT, 3 viable myocardial channels were detected (average 0.6 per animal), which resulted in only 1 HT channel (average 0.2 per animal). HT channel showed a heterogeneous myocardium feature mingled with scar, which was typically located along with the anterior side of interventricular groove, at the subepicardium and/or mid-myocardium underneath epicardial fat surrounding the LAD.

Animals with inducible VTs were more likely to have HT channels detected than animals with non-inducible VTs ($P < 0.01$, Fisher's exact test; Figure 4.6A). One non-inducible VT animal with an HT channel had a shorter channel length compared to animals with inducible VT (inducible-VT animals: 35 ± 14 mm vs. non-inducible VT animal: 9.94 mm; Figure 4.6B).

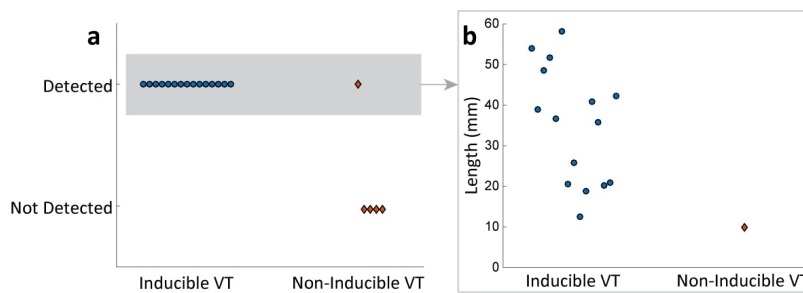


Figure 4.6: Results of heterogeneous tissue (HT) channel detection. A) HT channel was detected in all animals with inducible ventricular tachycardias (VT), whereas it was only detected in one animal with a non-inducible VT. Animals with inducible VTs were more likely to have HT channels detected than animals with non-inducible VTs ($P < 0.01$, Fisher's exact test). B) Of all animals with detected HT channels, only one non-inducible VT animal had a shorter channel length (inducible-VT animals: 35 ± 14 mm vs. non-inducible VT animal: 9.94 mm).

4.3.4 Site of Origin of VT

Among 20 animals with prior myocardial infarction, VTs were induced in 15 animals (75%) by a programmed stimulation or spontaneous premature ventricular contractions. One animal was excluded from the analysis for the site of origin of VT due to the lack of ECG data.

A total of 31 monomorphic VTs were induced in 14 swine and the average number of induced VTs were 2.2 per animal. Since previous studies showed that LBBB pattern VT arose from the RV or the interventricular septum (IVS) and RBBB pattern VT did from the LV [71], we further analyzed whether the site of origin of VT could be related to the location of detected HT channels. The mean cycle length of VTs was 244 ± 38 ms and the duration of QRS was 126 ± 23 ms. 90 % (28/31 VTs) had LBBB pattern, while only 10 % (3/31 VTs) did RBBB pattern. All animals with LBBB VTs had structural breakthrough sites at the RV or IVS, at the RV apex and the antero-septum of the mid-LV, which corresponded to the distal end and the proximal end of the HT channels, respectively.

More detailed localization of VT origin was identified in EAM by activation mapping during VT, which was compared to the location of the detected HT channels. VT exit sites were identified as the earliest activation points. Bipolar voltage maps of both left and right ventricles during sinus rhythm were compared to localize exit sites on the VT activation maps. For all animals, VT exits were located near the anterior side of interventricular groove, where HT channels were predominantly detected (Figure 4.7), which suggests potential involvement of detected HT channels in the VT.

4.3.5 Comparison to Histology

Histopathological analysis revealed complex viable myocardium structure in the anterior wall post-infarction due to the involvement of the RV and IVS. The overall architecture and distribution of scar were consistent with the CMR data (Figure 4.8). Analysis of the scar distribution showed heterogeneous distribution of collagen within the infarct and particularly along the anterior side of interventricular groove, consistent with typical location of HT channels (Figure 4.8).

4.4 DISCUSSION

We developed a workflow to identify HT channels within the areas of dense scar from high-resolution ex-vivo T_1 -weighted CMR images. 3D structural modeling was performed to extract viable myocardium in and around the scar. The 3D skeleton was created to automate characterization of structural properties of the viable myocardium model. Based on the skeleton, the cross-sectional area and tissue heterogeneity were characterized to detect HT channels, which are of interest for causing slow conduction. The proposed technique was successfully tested in 20 animals with prior myocardial infarction, 15 of which had scar-related VT and 5 which did not. Our results suggest that animals with inducible VT are more likely have detected HT channels than animals with non-inducible VT. We used 12-lead ECG and EAM to

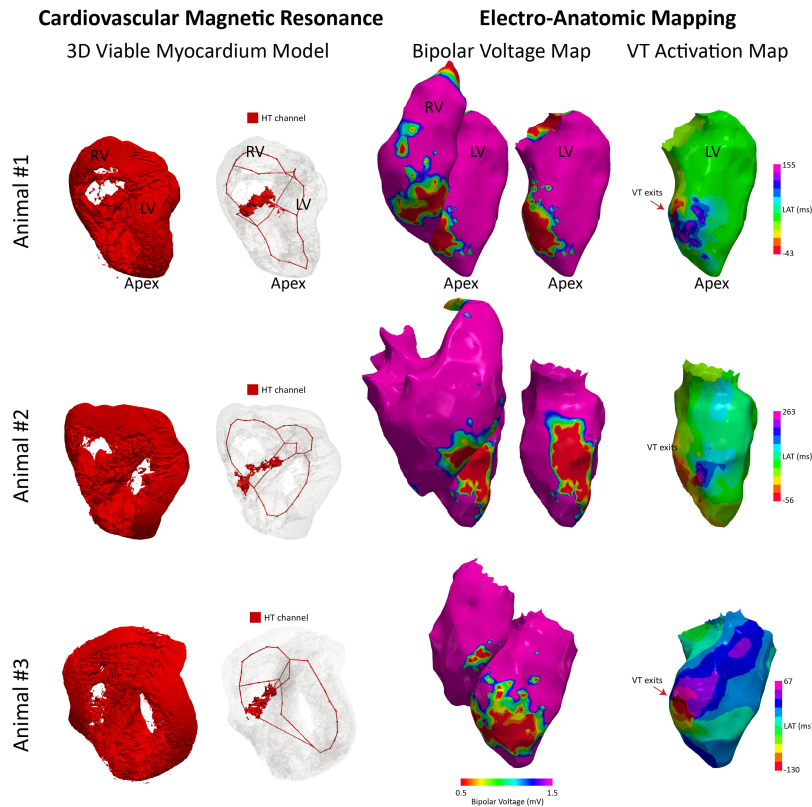


Figure 4.7: 3D viable tissue model and detected HT channels compared to the electroanatomic mapping data in 3 animals with inducible VT. Bipolar voltage maps during sinus rhythm in both right and left ventricles show similar scar distribution compared to the CMR 3D model. VT exits identified in the activation maps during VT are located near the anterior side of interventricular groove, consistent with where HT channels were detected.

identify the site of origin during VT, which preferred LBBB pattern, consistent with the structural breakthrough site observed at hinge point of HT channels located at interventricular groove anchored to two different regions of intact healthy myocardium. Histopathological analyses confirmed heterogeneous distribution of the viable tissue along the anterior side of interventricular groove, where HT channels were predominantly detected.

We have focused on the modeling of viable tissue rather than the scar where electrical signal travel across. 3D modeling of the viable myocardium enables us to understand cardiac impulse propagation in a true 3D manner. 3D skeletonization enables visualization of potential reentrant circuits based on the anatomical structure, reducing physicians burden to imagine potential anatomical electrical pathways in

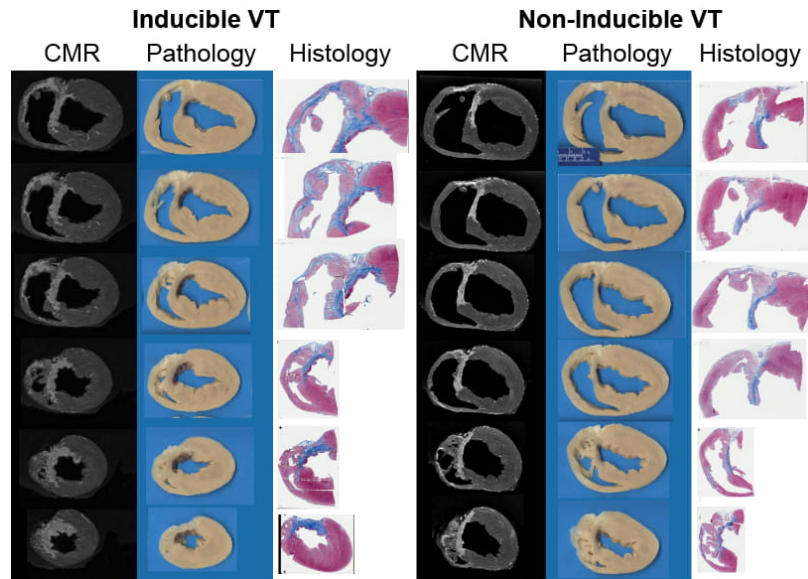


Figure 4.8: Comparison between CMR and histopathological analyses. A $5\text{-}\mu\text{m}$ histological slide with Masson's trichrome staining are shown in an anterior-posterior projection. The histological specimen shows complex scar architecture with areas of transmural scar and subendocardial preservation, along with extensive RV and interventricular septum involvement. The overall architecture and distribution of scar were consistent with the LGE data.

their minds. Visualizing anatomical circuits may further improve our understanding of structural and anatomical substrate for arrhythmias.

The proposed technique allows automated quantification of the 3D structural properties based on the segmented skeletal analysis. 3D skeletal graph consists of nodes and edges, which abstract a shape of the structural model. 3D graph representation of the structure allows automated quantification of the structural properties of each segment and their connectivity. Therefore the structural characteristics of the model, such as length, area, or thickness can be automatically quantified based on the simplified graph. It may be useful to quantify the length of the anatomical pathway, as reentry is only initiated when the length of the anatomical circuit is greater than the wavelength [132]. Automated quantification of the anatomical isthmus may offer an automated diagnosis of VT vulnerability. This technique can be further extended to detect any desired structure with certain structural properties.

The proposed technique allows automated pinpointing of HT channels and can be applied to any region of the heart to localize any heterogeneous structures or anatomical isthmus that may be susceptible to slow conduction. If merged with electroanatomic data or computer simulation, it will improve our understanding of the VT

mechanism and may support personalized planning for VT ablation. VT ablation outcome of effective removal of such structures identified on the proposed technique should be studied further.

Our study has several limitations. The proposed technique in this study is purely an anatomical approach and is not applicable to functional mechanisms of arrhythmias. We did not study whether ablation of anatomic regions identified with the proposed technique would improve VT ablation outcome. The correlation between HT channels, the site of VT origin, and histology was made as carefully as possible; however, it is based on gross estimation. The technique was not tested in-vivo, although it is expected to be applicable with the advancement of high-resolution in-vivo CMR imaging technique. This study focused on macro tissue structures, future studies will have to account for micro tissue structures by generating the 3D model in higher resolution and performing image segmentation and structural modeling in finer detail.

3D HOLOGRAPHIC VISUALIZATION OF MYOCARDIAL SCAR

5.1 INTRODUCTION

Late gadolinium enhancement (LGE) imaging in cardiovascular magnetic resonance (CMR) is a clinical gold standard for imaging of the myocardial scar [77]. In structural heart disease, ventricular tachycardia (VT) is usually caused by re-entry, involving an arrhythmogenic substrate in the region of ventricular scar from a prior myocardial infarction [69]. The extent of LGE has been reported to identify the arrhythmogenic substrate [17], and improves a risk stratification for implantable cardioverter defibrillator therapy [67, 79] in patients with ventricular arrhythmias. Scar border zone defined in LGE has shown good correlation with VT inducibility [107] and spontaneous ventricular arrhythmias [49, 99, 108]. The detailed scar depiction of the LGE has been suggested to be useful for planning and guiding scar-related VT ablation by characterizing location and extent of the scar [7, 43]. Understanding the 3D scar architecture is particularly important in the assessment of the VT substrate.

In the histological study, conduction channels have been described as surviving fiber bundles embedded in myocardial scar areas that can be located at any level of the myocardial wall, with a variable thickness and 3D structure [41, 50]. In electrophysiology study, voltage mapping is performed to identify “conduction channels” in and around the scar that could represent the VT isthmus. 3D LGE provides a better understanding of the complex scar anatomy compared with voltage mapping alone for guiding the radio-frequency (RF) ablation for VT [43]. Therefore, visualization of the 3D scar is important for identification of VT substrate and guidance of RF ablation for VT treatment.

Augmented reality has been emerging for visualizing complex medical data, particularly during and planning medical procedures [57]. In particular, HoloLens (Microsoft, Redmond, WA) [116] has enabled visualization of complex medical data that can provide immersive experience to interactively explore the data in 3D space in the mixed-reality environment, and has been tested in various clinical scenarios [38, 80]. Augmented reality allows true 3D visualization that provides 3D depth perception, and opens up the possibility for interacting with the medical data without physical contact to assist while maintaining sterile environment and reduce the risk of infection.

Augmented reality shows promise for supporting interventional procedures. After the first in-human example of creation of dynamic interactive holograms from intraprocedural data [23], various studies have explored the use of holographic augmentation in various interventional procedures such as invasive structural cardiac procedures [22], ultrasound-guided transcatheter aortic valve implantation [39], neurosurgery [84], endovascular intervention [80], and near-infrared fluorescence based image guided surgery [38]. In the field of electrophysiology, a recent study reports first in-human experience of projecting intra-procedural electrophysiology data into an interactive holographic display [111].

In this study, we sought to develop a framework for 3D holographic visualization of the LGE images on augmented reality HoloLens to provide a true 3D perception of the scar architecture with a direct physician interaction in a sterile environment. A pilot animal study was performed to demonstrate the feasibility of using 3D HoloLens visualization of scar in electrophysiology study.

5.2 METHODS

We propose a framework for 3D holographic visualization based on the high-resolution 3D LGE images to generate a 3D myocardial scar model and visualize on HoloLens (Microsoft, Redmond, WA). An overview of the proposed framework is presented in Figure 5.1, and detailed processing pipelines for 3D volumetric and endocardial projection of the scar are presented in the following sections.

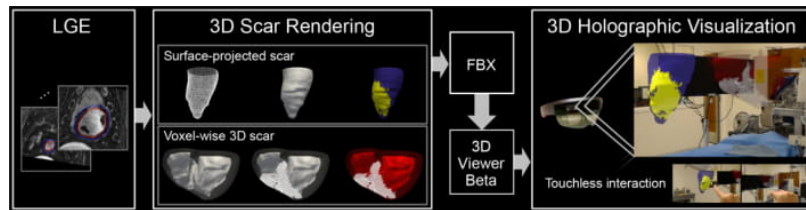


Figure 5.1: A framework for holographic visualization of the 3D late gadolinium enhancement (LGE) data. Endo- and epicardial contours are delineated in LGE images and surface-projected scar and voxel-wise 3D scar models are generated. 3D models are converted to Filmbox (FBX) file format to be able to load on 3D Viewer Beta (Microsoft, Redmond, WA). 3D scar LGE models are holographically visualized in the 3D mixed-reality space, which provides true 3D perception of the complex scar architecture with immersive experience to explore the 3D LGE images with a touchless interaction while maintaining sterile environment.

5.2.1 Myocardial Geometry Reconstruction

The initial step of the framework is reconstructing endo and/or epicardial surface meshes. Previous study showed that reconstructing ventricular geometry using variational implicit function-based method provides the most accurate model [96], therefore we used Poisson surface reconstruction which uses an implicit function framework [73]. Endocardial and epicardial contours were manually delineated from LGE images in all slices. Contours in all slices were merged into a set of point clouds for each surface. Clustering decimation was performed to organize point clouds based on the cell of 3D grid, followed by computing the surface orientation of all vertices based on the 10 nearest neighboring points in the point clouds. Endo/ epicardial triangular surface meshes were then generated using a Poisson surface reconstruction [34, 73].

5.2.2 Voxel-wise 3D Scar Rendering

Proposed framework for voxel-wise 3D scar rendered holographic visualization of the high-resolution LGE data is described in [Figure 5.2](#). Endo and epicardial surface meshes were reconstructed as described in the previous section. Scar tissue was defined as voxels in the myocardium with a signal intensity greater than a full-width at half-maximum (FWHM) [53]. To preserve high-resolution information of LGE voxels, every single voxel of the scar was rendered into a cube which carries the actual resolution of the LGE scan. Any duplicated vertices and faces were removed to reduce the size of the rendered scar mesh. All layers of rendered surface and scar mesh were then blended with different transparency and color to enhance visibility and perception.

5.2.3 Surface Projection of the Scar

The framework for holographic scar visualization of projected surface model is described in [Figure 5.3](#). Endocardial surface mesh was first created using a Poisson surface reconstruction as described in the previous section. LGE voxels in the subendocardial region (0-33% from endocardial to epicardial) was projected onto the endocardial points. Endocardial points with projected scar information were then transferred to a texture, which was followed by a texture mapping performed on the parametrized Poisson surface of the endocardial mesh. The proposed framework was implemented in Matlab (MathWorks, Natick, MA) and MeshLab (Visual Computing Lab – ISTI – CNR, Rome, Italy) [34].

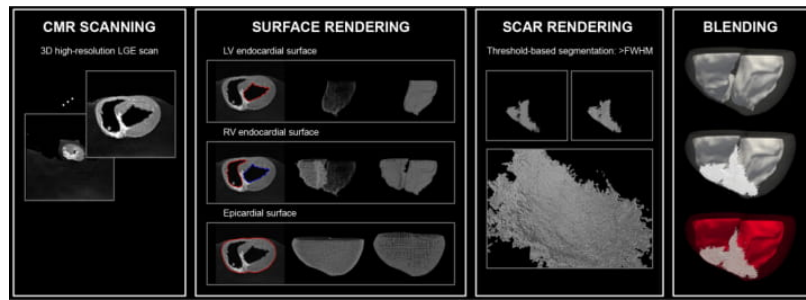


Figure 5.2: A framework for holographic visualization of the 3D late gadolinium enhancement (LGE) data. Left/ right ventricular (LV/ RV) endo-/ epicardial contours are manually delineated on short-axis view, and LV/RV endo-/ epicardial surfaces are estimated using Poisson surface reconstruction. Scar tissue was defined as voxels in the myocardium with signal intensity greater than a full-width at half-maximum (FWHM). Every voxel was then rendered into a single cube with the actual resolution of the LGE scan. All surface and scar layers were blended with different transparency and color to enhance visibility and perception.

5.2.4 Augmented Reality System

Voxel-wise 3D scar rendered model and surface-projected scar model were generated as described in the previous section, which were then exported to Filmbox (FBX) file format on Blender (Blender Foundation, Amsterdam, Netherland) and was imported onto HoloLens using OneDrive (Microsoft, Redmond, WA) and visualized using a 3D Viewer Beta (Microsoft, Redmond, WA).

5.2.4.1 System Performance

The system performance of the HoloLens while running the generated voxel-wise 3D scar and surface projected scar model were compared with the baseline performance on HoloLens while nothing was running. System on a chip (SoC) power, system power, frame rate, CPU and GPU usage percentage were reported for each case.

5.2.5 Pilot Animal Study

A pilot animal study was performed to test feasibility of using holographic 3D LGE visualization in an electrophysiology study. This study was carried out in strict accordance with the recommendations in the Guide for the Care and Use of Laboratory Animals of the National Institutes of Health. The protocol was approved by the Beth Israel Deaconess Medical Center's Institutional Animal Care and Use Committee (Protocol Number: 100-2014; Boston, MA, USA). All experiments were performed under general anesthesia with isoflurane

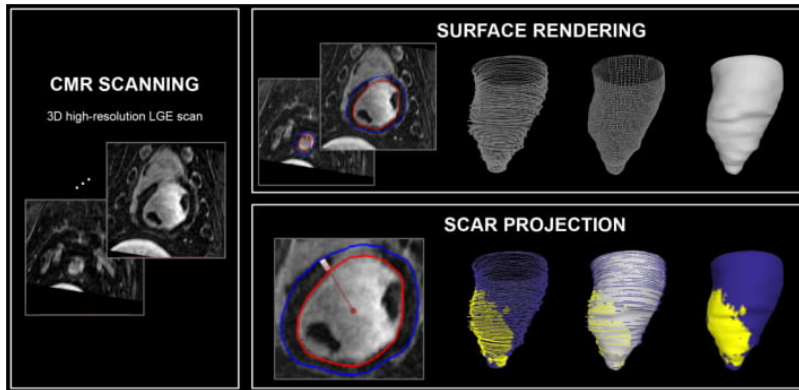


Figure 5.3: A framework for holographic visualization of endocardial surface with scar projection. LV endo-/ epicardial contours are manually delineated on short-axis view. Endocardial surface is then generated using a Poisson surface reconstruction by first performing clustering decimation followed by the surface orientation estimation based on the 10 neighboring points. To project color-coded scar information on the reconstructed endocardial surface, myocardium was divided into subendo, mid, subepicardial regions, and the subendocardial scar information was projected onto the endocardial surface mesh.

inhalation (1.5-2.5%) and mechanical ventilation (12-16 breaths/min with tidal volumes between 300-400ml), and animal was euthanized with pentobarbital sodium.

A flowchart of the pilot animal experiment is presented in [Figure 5.4](#). Five swines underwent 180 minute balloon occlusion of the mid left anterior descending artery to create an ischaemia-reperfusion mediated myocardial infarction model [121]. After the infarction, animals were recovered and survived for 8 weeks and underwent in-vivo CMR. High-resolution 3D LGE image was acquired with the low-dimensional-structure self-learning and thresholding reconstruction technique [1-3, 15]. Detailed CMR imaging parameters are reported in the next section. Holographic 3D LGE models were created as proposed using the in-vivo CMR, and after several days of recovery, animals underwent electrophysiology study where VT substrate mapping was performed. After the procedure, ex-vivo CMR imaging was performed and higher-resolution holographic model was generated using the ex-vivo CMR.

In the electrophysiology study, electroanatomic mapping was performed to define the arrhythmogenic VT substrate. Prior to the mapping procedure, both operator and mapping specialist used HoloLens 3D LGE data to review ventricular geometry and myocardial scar architecture, the size and extent of the scar from the voxel-wise 3D scar model and endocardial surface-scar projected model. Upon completion of the study, operator and mapping specialist independently

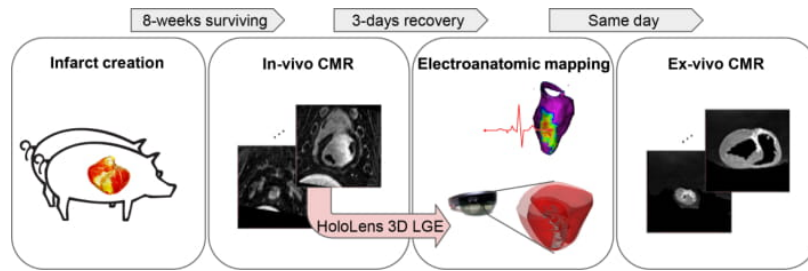


Figure 5.4: A flowchart of the pilot animal experiment. Myocardial infarction was created by occluding the mid left anterior descending artery. After 8 weeks of recovery and survival periods, animals underwent in-vivo CMR with high-resolution 3D LGE sequence. Based on the in-vivo CMR images, HoloLens 3D LGE model was generated and tested with the electroanatomic substrate mapping. After the electrophysiology study, ex-vivo imaging was performed to create higher-resolution HoloLens 3D LGE model.

completed the perceived usefulness questionnaire [40] to assess the perceived usefulness of the HoloLens 3D LGE consisting of 6 items on a seven-point Likert scale (1: extremely unlikely – 7: extremely likely). The overall usefulness rating is reported as a mean score of all 6 usefulness items for both the operator and the mapping specialist.

5.2.6 CMR Imaging

In-vivo and ex-vivo CMR imaging were performed to generate holographic 3D LGE models as described in the previous section. CMR imaging was performed using a 1.5 T Philips scanner (Philips Achieva, Best, Netherland) with a 32-element cardiac phased-array receiver coil. For in-vivo imaging, high-resolution 3D LGE images with random under-sampled accelerated acquisition [1–3, 15] were acquired 15-25 minutes after injection of 0.2 mmol/kg gadobenate dimeglumine (MultiHance; Bracco Imaging, Milan, Italy). A respiratory navigator with adaptive acquisition window [87] was used for prospective motion correction. Imaging parameters were as follows: gradient echo imaging sequence; TR/TE = 6.1/2.7 ms; field of view = $270 \times 270 \times 112 - 280 \times 280 \times 112 \text{ mm}^3$; flip angle = 25° ; isotropic spatial resolution = $1.0 \times 1.0 \times 1.0 \text{ mm}^3$. Ex-vivo imaging was performed using high-resolution 3D gradient echo sequence with the following imaging parameters: TR/TE = 17/8 ms; field of view = $130 \times 130 \times 100 \text{ mm}^3$; flip angle = 25° , isotropic spatial resolution = $0.4 \times 0.4 \times 0.5 \text{ mm}^3$.

5.3 RESULTS

5.3.1 *Animal Model*

An extensive LGE was observed in the anterior-septal regions in 8 weeks-post myocardial infarction swine. The distribution of the LGE was complex, with the areas of transmural or near transmural scar and subendocardial sparring. The overall LGE volume was 9.2 ± 7.5 % of the entire left ventricular myocardial volume, with the endocardial portion of the LGE corresponds to 34.8 ± 8.6 % of the total scar volume. The percentage of the LGE area projected on the endocardial surface was 13.8 ± 9.4 %. The endocardial LGE surface regions corresponded to the bipolar voltage amplitude < 1.5 mV in the electroanatomic mapping.

5.3.2 *Augmented Reality System Performance*

For the in-vivo voxel-wise 3D LGE models, the number of vertices were $19,849 \pm 13,216$ and the number of faces were $81,035 \pm 58,794$. For the ex-vivo voxel-wise models, the number of vertices were $300,308 \pm 382,670$ and the number of faces were $962,480 \pm 1,311,111$. For the surface rendered LGE models, the number of vertices were $7,217 \pm 2,381$ and the number of faces were $14,263 \pm 4,737$. The typical processing time of all models for a single animal was about 1-2 hours, most of which was used for performing manual delineation of endo- and epicardial contours. Except for the contour delineation, no process takes longer than several minutes. The overall processing time therefore can be significantly reduced by using automated left and right ventricle segmentation techniques.

The system performance of the HoloLens while running the generated 3D holographic LGE model was compared with the baseline and summarized in [Table 5.1](#). Surface model that was used for the performance test consists of 7,586 vertices and 2 materials were located. Voxel-wise 3D model that was used for the performance test consists of 290,506 vertices and 3 materials were located. SoC and system power were slightly increased with voxel-wise whole-heart 3D model, but CPU, and GPU usage stayed at the similar level.

5.3.3 *Holographic Visualization of 3D LGE*

The demonstration of the holographic visualization of the 3D LGE data using the proposed frameworks was recorded on HoloLens and presented in [Figure 5.5](#). The 3D holographic visualization of the whole-heart voxel-wise 3D scar rendering and scar projected endocardial surface mesh are demonstrated in [Figure 5.5A](#). The user could interactively explore 3D LGE myocardial scar by scaling, rotating, moving,

	Baseline	Surface-projected Model	Voxel-wise 3D Model
SoC Power (%)	56	65	73
System Power (%)	60	70	74
Frame Rate (fps)	60.05	60.1	60.05
CPU (%)	35	34	44
GPU (%)	16.81	28.76	25.12

Table 5.1: System Performance of HoloLens with the 3D LGE Models. Baseline (when nothing is running on the HoloLens), surface-projected model (when surface projected scar model is running on the HoloLens), and voxel-wise 3D model (when voxel-wise 3D model is running on the HoloLens) were compared for system on a chip (SoC) power, system power, frame rate, CPU, and GPU usage.

and viewing from any perspective in the augmented reality environment that allows for the combination of holographic 3D LGE data interacting with any real-world environments, such as a surgical suite or patient’s body. Holographic 3D LGE data can be viewed in any environment.

Figure 5.5B represents the endoscopic view of the holographic 3D LGE with the whole-heart voxel-wise 3D LGE model. The user can view the scar from inside of the ventricular chambers. As user steps into the heart, the transparent epicardial surface layer becomes invisible and the inner scar architecture can be explored more in detail. Figure 5.6 shows operator and mapping specialist view during the electrophysiology study. Both operator and mapping specialist found HoloLens 3D LGE useful (overall usefulness rating: operator, 5.8; mapping specialist, 5.5, on a scale from 1: extremely unlikely useful to 7: extremely likely useful; Figure 5.7) in the VT substrate mapping and RF ablation procedures. The operator could directly review holographic 3D LGE data with a touchless interaction in sterile environment, and without additional hardware installations. The operator could visually compare the detailed 3D scar information with electroanatomic mapping data by overlaying the holographic scar on the electroanatomic map or viewing side by side (Figure 5.6A). The mapping specialist could review scar information for navigating the electroanatomic mapping (Figure 5.6B).

5.4 DISCUSSION

We present a framework for 3D visualization of the high-resolution 3D LGE of myocardial scar in a holographic manner on the augmented-reality glass HoloLens. High-resolution 3D LGE sequence was used to image the myocardial scar, and 3D rendered LGE model was generated and visualized on HoloLens 3D Viewer Beta. HoloLens 3D LGE

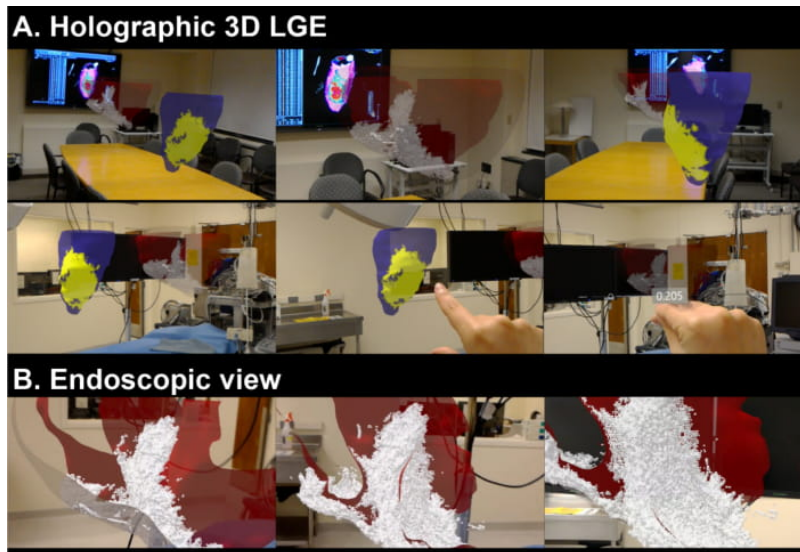


Figure 5.5: Demonstration of the 3D holographic visualization of the voxel-wise 3D scar rendering and scar projected endocardial surface mesh from 3D LGE data that are generated based on the proposed framework. User can interactively explore 3D LGE myocardial scar by scaling, rotation, moving, and viewing from any perspective in the augmented reality environment (A). In the 3D scar rendered model, as user walks closer to the model, the transparent epicardial surface layer becomes invisible and the inner scar volumes can be explored more in detail (B). Augmented reality representation of the 3D LGE data provides embodied experience to explore the clinical standard LGE images in a more interactive, and interpretable way.

was tested in the swine model of myocardial infarction with electrophysiology study of arrhythmogenic substrate mapping. Operator and mapping specialist interacted with HoloLens 3D LGE to review the extent and the structure of 3D myocardial scar and compared with the electroanatomic mapping data. Both operator and mapping specialist found HoloLens 3D LGE useful with a usefulness rating of 5.8 and 5.5, on a scale from 1 to 7, respectively. Holographic visualization of the 3D LGE images provides a true 3D perception of the complex scar architecture with immersive experience to explore the 3D LGE in a more interactive and interpretable way.

Holographic visualization of the LGE images allows to attain touchless interaction with the clinical data in sterile environments, thereby permitting the operator to have increased control and manipulation over pre- or intra-procedural information. Due to a robust gesture tracking using a depth sensor and camera, a user can also operate a HoloLens with a gloved and soiled hand. The availability of such augmented reality technologies to potentially improve procedural efficacy may be useful in the future for complex procedures, and the proposed

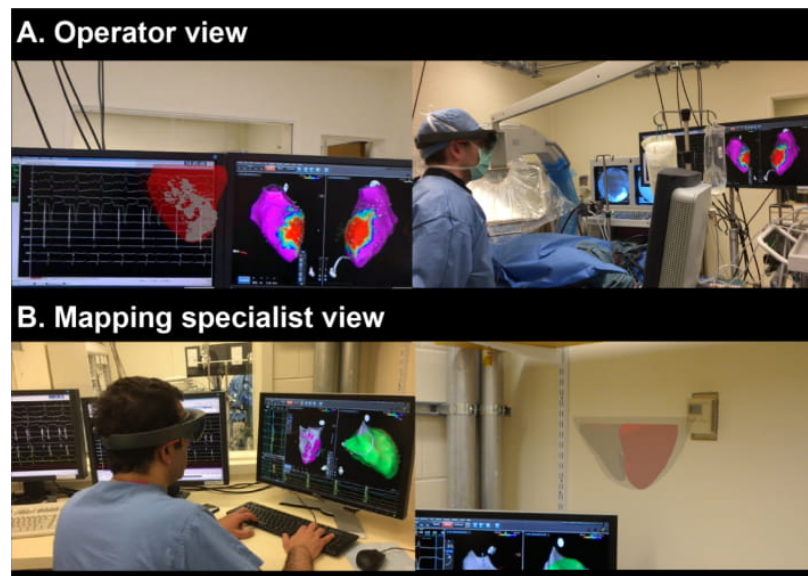


Figure 5.6: Demonstration of the HoloLens 3D LGE during the electroanatomic mapping and radio-frequency ablation of ventricular tachycardia in the pilot animal study. Holographic voxel-wise 3D LGE was created as proposed using the in-vivo CMR high-resolution 3D LGE images. The holographic LGE models were tested during the electrophysiology procedure. In the operator view, holographic scar can be compared with the electroanatomic data by overlaying holograms on the mapping system (A). The scar information facilitates navigation of electroanatomic mapping procedures (B).

framework can also be applied in other interventional and surgical procedures.

HoloLens 3D LGE allows detailed scar depiction with a 3D perception. Flat-screen visualizations of the complex three-dimensional myocardial scar structure limit our understanding due to the lack of the depth perception. Understanding the complex 3D scar anatomy using stereoscopic 3D visualization enables operator and mapping specialist to have a clear plan for VT substrate mapping and RF ablation. The endoscopic view further assist operator for a detailed pre-procedural plan for the endocardial catheter mapping. The current electrophysiology procedures are usually performed as a team of operator and a mapping specialist. Due to the sterility concerns, the operator does not have access to the mapping system inputs, which limits operator's ability to directly interact with maps during the intervention.

HoloLens will provide the operator a higher level of control and visibility and reduce the frustrations of miscommunication between the operator and the mapping specialist by offering touchless interaction. Furthermore, if integrated with the real-time electroanatomic

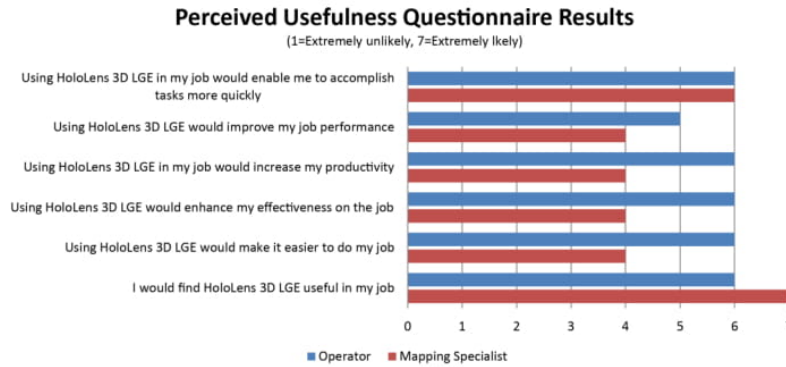


Figure 5.7: The perceived usefulness questionnaire results from operator and mapping specialist. The usefulness rating is reported as a mean rating of all 6 usefulness items in the questionnaire. Both operator and mapping specialist found HoloLens 3D LGE useful (usefulness rating: operator, 5.8; mapping specialist, 5.5, on a scale from 1 to 7).

data and the catheter position, it will improve image-based guidance and VT ablation outcome.

Augmented reality allows us to combine holographic 3D LGE data interacting with any real-world environments, and may in the future facilitate data fusion and exploration of the LGE and electroanatomic data to support planning and performing VT ablation. HoloLens also offers unique interactive capabilities between multiple individuals, which may support pre-procedural planning in a group.

Recent study reports significantly reduced procedural and fluoroscopy time when merging LGE into the clinical mapping system to perform VT ablation [9], although another study report no differences in procedural or fluoroscopy time [131]. We did not measure the procedural or fluoroscopy time in this study, however, the impact on having additional information about the myocardial scar may provide similar experience to operators.

We used ex-vivo imaging only for the development phase, and did not test during the intervention or evaluate for the usefulness. Modeling of ex-vivo images can be challenging due to very high spatial resolution ($400 \times 400 \times 500 \mu\text{m}^3$ in the current study) and large data size. We showed that three-dimensional holographic visualization of high-resolution ex-vivo images of $400 \mu\text{m}$ is feasible on HoloLens. Further improvement of the in-vivo CMR imaging techniques will enable higher-resolution imaging and offer a detailed depiction of the myocardial scar in the augmented reality environment during the intervention.

Our animal study was a pilot study towards demonstrating the feasibility of data visualization, and we did not use HoloLens 3D LGE for guiding ablation in real-time. We did not use ablation success as

an endpoint in our study. The questionnaire was performed by one operator and one mapping specialist; however, neither of the investigators were involved in developing the technology. The weight of the HoloLens is 579 g which may hamper interventional applications, and further design modification should be done to reduce weight and thereby improve comfort level during the intervention.

Part III

DISCUSSION AND OUTLOOK

DISCUSSION

This thesis demonstrates that CMR imaging and computer vision techniques can identify the arrhythmogenic scar and fibrosis of the underlying VT substrate:

- CMR allows non-invasive imaging-based identification of slow conduction region
- CMR allows 3D structural reconstruction of an arrhythmogenic heart structure
- CMR allows the effective presentation of complex myocardial scar in a 3D mixed-reality environment

Slow conduction regions are necessary for the initiation and maintenance of re-entrant arrhythmias, which are responsible for the majority of arrhythmias observed in tissue damaged by prior myocardial infarction. In the first study, CMR imaging features in the region of slow conduction was investigated by spatially aligning CMR and electrophysiology data. The study showed that slow conduction measured using invasive catheter mapping is exhibited in the areas of the presence of LGE and wall thinning, and the region with higher LGE heterogeneity and wall thickness gradient. CMR offers a valuable imaging surrogate for estimating conduction velocity, which enables non-invasive imaging identification of the arrhythmogenic substrate.

The second study demonstrated a workflow to identify heterogeneous tissue channel based on the structural 3D modeling of the viable myocardium within areas of a dense scar. The geometrical structure of the myocardium plays an essential role in understanding the initiation of arrhythmias. In particular, a heterogeneous tissue channel defined in CMR has been suggested to correlate with conduction channels defined in electroanatomic mapping in VT. Our results indicate that animals with inducible VT are more likely to have heterogeneous tissue channels than animals with non-inducible VT. The proposed technique allows automated pinpointing of heterogeneous tissue channels and can be expanded to localize any region of the heart with specific structural properties.

The last study demonstrated a framework for 3D holographic visualization of myocardial scar using the high-resolution 3D LGE images in mixed-reality. 3D holographic visualization provides an enhanced 3D perception of the complex scar architecture with immersive experience to explore scar in an interactive and interpretable 3D approach. It allows assessment of the complex 3D scar architecture with touchless

interaction while maintaining a sterile environment and facilitates CMR-guided VT ablation. Furthermore, any imaging features and structures can be effectively presented in the mixed-reality environment to support VT intervention.

In our studies, we did not study whether ablation of anatomic regions identified with the proposed techniques would improve VT ablation outcome, neither not used ablation success as an endpoint. Therefore, future clinical studies are warranted to confirm the role of the proposed techniques in clinical settings.

OUTLOOK

This thesis demonstrates that advanced CMR imaging techniques can enable identification of the arrhythmogenic scar and fibrosis of the heart, offering a non-invasive CMR imaging biomarker to support diagnosis and treatment of VT, ultimately enhancing risk-stratification of sudden cardiac death. The studies presented in this thesis shows exciting opportunities and role of CMR to identify the risk of VT, and opened up future research questions to explore.

Generating Images. Imaging quality matters. High-quality images make the analysis easier and post-processing steps less painful. Therefore, improvement of the generation of the image to enhance the quality and reduce imaging artifacts should be the foremost priority. Advancement of hardware as well as software such as the deployment of machine learning/ artificial intelligence (AI) in image reconstruction is enhancing the image quality.

Information in 3D. The electrical activity of the heart is complex, and the underlying 3D structure plays a crucial role. Therefore, understanding the complete cardiac electric circuit in 3D is imperative. By looking at the 2D projected view of images only, we may miss abundant information hidden in 3D. Future efforts should be continued to investigate the complex architecture of the heart in 3D.

Automated Segmentation. The current gold standard for delineating myocardium is manual segmentation, which can be time-consuming and introduce inter-observer variability. Automated segmentation has the potential to substantially save time for post-processing and image analysis, as well as improve robustness and reduce observer dependency. The advancement of AI is paving the way for automated segmentation for more robust image analysis.

Role of AI in Medical Imaging. Many of the preclinical imaging works are hypothesis-driven and based on *a priori* clinical understanding of specific diseases. Making implicit modeling and feature extraction would, therefore, be an exciting future direction to investigate. Using AI to learn and model the features implicitly could fundamentally improve our understanding of the images, which can be missed from the naked human eye.

BIBLIOGRAPHY

- [1] Mehmet Akçakaya, Tamer A Basha, Beth Goddu, Lois A Goepfert, Kraig V Kissinger, Vahid Tarokh, Warren J Manning, and Reza Nezafat. "Low-dimensional-structure self-learning and thresholding: Regularization beyond compressed sensing for MRI Reconstruction." In: *Magnetic Resonance in Medicine* 66.3 (2011), pp. 756–767. ISSN: 1522-2594.
- [2] Mehmet Akçakaya, Hussein Rayatzadeh, Tamer A Basha, Susie N Hong, Raymond H Chan, Kraig V Kissinger, Thomas H Hauser, Mark E Josephson, Warren J Manning, and Reza Nezafat. "Accelerated late gadolinium enhancement cardiac MR imaging with isotropic spatial resolution using compressed sensing: initial experience." In: *Radiology* 264.3 (2012), pp. 691–699. ISSN: 0033-8419.
- [3] Mehmet Akçakaya, Tamer A Basha, Raymond H Chan, Warren J Manning, and Reza Nezafat. "Accelerated isotropic sub-millimeter whole-heart coronary MRI: Compressed sensing versus parallel imaging." In: *Magnetic Resonance in Medicine* 71.2 (2014), pp. 815–822. ISSN: 1522-2594.
- [4] Sana M Al-Khatib, William G Stevenson, Michael J Ackerman, William J Bryant, David J Callans, Anne B Curtis, Barbara J Deal, Timm Dickfeld, Michael E Field, Gregg C Fonarow, et al. "2017 AHA/ACC/HRS guideline for management of patients with ventricular arrhythmias and the prevention of sudden cardiac death: a report of the American College of Cardiology/American Heart Association Task Force on Clinical Practice Guidelines and the Heart Rhythm Society." In: *Journal of the American College of Cardiology* 72.14 (2018), e91–e220.
- [5] Maurits A. Allessie, Felix I M Bonke, Wim Lammers, Joep Smeets, and John J. Fenoglio. "Electrophysiologic mapping to determine the mechanism of experimental ventricular tachycardia initiated by premature impulses. Experimental approach and initial results demonstrating reentrant excitation." In: *The American Journal of Cardiology* 49.1 (1982), pp. 166–185. ISSN: 00029149. DOI: [10.1016/0002-9149\(82\)90292-2](https://doi.org/10.1016/0002-9149(82)90292-2).
- [6] David Andreu, Antonio Berrueto, José T Ortiz-Pérez, Etelvino Silva, Lluís Mont, Roger Borràs, Teresa María de Caralt, Rosario Jesús Perea, Juan Fernández-Armenta, Hrvojka Zeljko, et al. "Integration of 3D electroanatomic maps and magnetic resonance scar characterization into the navigation system to guide

- ventricular tachycardia ablation." In: *Circulation: Arrhythmia and Electrophysiology* (2011), CIRCEP-111.
- [7] David Andreu, Antonio Berruezo, José T Ortiz-Pérez, Etelvino Silva, Lluís Mont, Roger Borràs, Teresa María de Caralt, Rosario Jesús Perea, Juan Fernández-Armenta, and Hrvojka Zeljko. "Integration of 3D electroanatomic maps and magnetic resonance scar characterization into the navigation system to guide ventricular tachycardia ablation." In: *Circ Arrhythm Electrophysiol* 4.5 (2011), pp. 674–683. ISSN: 1941-3149.
- [8] David Andreu, Diego Penela, Juan Acosta, Juan Fernández-Armenta, Rosario J Perea, David Soto-Iglesias, Teresa M de Caralt, Jose T Ortiz-Perez, Susana Prat-González, Roger Borràs, et al. "Cardiac magnetic resonance-aided scar dechanneling: Influence on acute and long-term outcomes." In: *Heart Rhythm* 14.8 (2017), pp. 1121–1128.
- [9] David Andreu, Diego Penela, Juan Acosta, Juan Fernández-Armenta, Rosario J Perea, David Soto-Iglesias, Teresa M de Caralt, Jose T Ortiz-Perez, Susana Prat-González, and Roger Borràs. "Cardiac magnetic resonance-aided scar dechanneling: Influence on acute and long-term outcomes." In: *Heart Rhythm* 14.8 (2017), pp. 1121–1128. ISSN: 1547-5271.
- [10] *Arrhythmia Ablation Therapy*. URL: <https://www.uchicagomedicine.org/conditions-services/heart-vascular/arrhythmias/treatments/ablation-therapy>.
- [11] Hiroshi Ashikaga, Tetsuo Sasano, Jun Dong, M Muz Zviman, Robert Evers, Bruce Hopenfeld, Valeria Castro, Robert H Helm, Timm Dickfeld, Saman Nazarian, et al. "Magnetic resonance-based anatomical analysis of scar-related ventricular tachycardia." In: *Circulation research* 101.9 (2007), pp. 939–947.
- [12] Hiroshi Ashikaga, James Coromilas, Bruce Hopenfeld, Daniel O. Cervantes, Andrew L. Wit, Nicholas S. Peters, Elliot R. McVeigh, and Hasan Garan. "Model of bipolar electrogram fractionation and conduction block associated with activation wavefront direction at infarct border zone lateral isthmus boundaries." In: *Circulation: Arrhythmia and Electrophysiology* 7.1 (2014), pp. 152–163. ISSN: 19413084. DOI: [10.1161/CIRCEP.113.000840](https://doi.org/10.1161/CIRCEP.113.000840).
- [13] Oscar Kin-Chung Au, Chiew-Lan Tai, Hung-Kuo Chu, Daniel Cohen-Or, and Tong-Yee Lee. "Skeleton extraction by mesh contraction." In: *ACM Transactions on Graphics (TOG)* 27.3 (2008), p. 44.
- [14] Clerio F. Azevedo et al. "Infarct tissue heterogeneity by magnetic resonance imaging identifies enhanced cardiac arrhythmia susceptibility in patients with left ventricular dysfunction." In:

- Circulation* 115.15 (2007), pp. 2006–2014. ISSN: 00097322. DOI: [10.1161/CIRCULATIONAHA.106.653568](https://doi.org/10.1161/CIRCULATIONAHA.106.653568).
- [15] Tamer A Basha, Mehmet Akcakaya, Charlene Liew, Connie W Tsao, Francesca N Delling, Gifty Addae, Long Ngo, Warren J Manning, and Reza Nezafat. “Clinical performance of high-resolution late gadolinium enhancement imaging with compressed sensing.” In: *J Magn Reson Imaging* (2017). ISSN: 1522-2586.
- [16] Philip V. Bayly, Shu Zhang, Gregory P. Walcott, Raymond E. Ideker, and William M. Smith. “Estimation of 3-D conduction velocity vector fields from cardiac mapping data.” In: *IEEE Transactions on Biomedical Engineering* 47.8 (2000), pp. 1027–1035. ISSN: 00189294. DOI: [10.1109/10.855929](https://doi.org/10.1109/10.855929).
- [17] David Bello, David S Fieno, Raymond J Kim, F Scott Perales, Rod Passman, Gina Song, Alan H Kadish, and Jeffrey J Goldberger. “Infarct morphology identifies patients with substrate for sustained ventricular tachycardia.” In: *Journal of the American College of Cardiology* 45.7 (2005), pp. 1104–1108. ISSN: 0735-1097.
- [18] Emelia J Benjamin, Salim S Virani, Clifton W Callaway, Alanna M Chamberlain, Alexander R Chang, Susan Cheng, Stephanie E Chiuve, Mary Cushman, Francesca N Delling, Rajat Deo, et al. “Heart disease and stroke statistics—2018 update: a report from the American Heart Association.” In: *Circulation* 137.12 (2018), e67–e492.
- [19] Antonio Berruezo et al. “Use of myocardial scar characterization to predict ventricular arrhythmia in cardiac resynchronization therapy.” In: *Europace* 14.11 (2012), pp. 1578–1586. ISSN: 10995129. DOI: [10.1093/europace/eus104](https://doi.org/10.1093/europace/eus104).
- [20] Evert J Blink. “mri: Physics.” In: *Online PDF file* (2004), pp. 0–75.
- [21] C. Jan Willem Borleffs et al. “Infarct tissue heterogeneity assessed with contrast-enhanced mri predicts spontaneous ventricular arrhythmia in patients with ischemic cardiomyopathy and implantable cardioverter-defibrillator.” In: *Circulation: Cardiovascular Imaging* 2.3 (2009), pp. 183–190. ISSN: 19419651. DOI: [10.1161/CIRCIMAGING.108.826529](https://doi.org/10.1161/CIRCIMAGING.108.826529).
- [22] Elchanan Bruckheimer and Cannel Rotschild. “Holography for imaging in structural heart disease.” In: *EuroIntervention: journal of EuroPCR in collaboration with the Working Group on Interventional Cardiology of the European Society of Cardiology* 12 (2016), pp. X81–X84. ISSN: 1774-024X.

- [23] Elchanan Bruckheimer, Carmel Rotschild, Tamir Dagan, Gabriel Amir, Aviad Kaufman, Shaul Gelman, and Einat Birk. "Computer-generated real-time digital holography: first time use in clinical medical imaging." In: *European Heart Journal-Cardiovascular Imaging* 17.8 (2016), pp. 845–849. ISSN: 2047-2412.
- [24] M Callieri, M Corsini, M Dellepiane, F Ganovelli, and Guido Ranzuglia. "MeshLab: an open-source mesh processing tool." In: *Eurographics Italian Chapter Conference* (2008), pp. 129–136. ISSN: 0167-577X. DOI: [10.2312/LocalChapterEvents/ItalChap/ItalianChapConf2008/129-136](https://doi.org/10.2312/LocalChapterEvents/ItalChap/ItalianChapConf2008/129-136).
- [25] A John Camm and Douglas P Zipes. "Ventricular Arrhythmias and Sudden Cardiac Death." In: *The AHA Guidelines and Scientific Statements Handbook* (2008), pp. 270–292.
- [26] Chris D Cantwell, Caroline H Roney, Norman A Qureshi, Phang Boon Lim, Jennifer H Siggers, Spencer J Sherwin, and Nicholas S Peters. "A novel method for quantifying localised correlation of late-gadolinium intensity with conduction velocity." In: *CINC - Computing in Cardiology* 41 (2014), pp. 193–196. ISSN: 2325887X 23258861.
- [27] Chris D. Cantwell, Norman A. Qureshi, Rheeda L. Ali, Eugene T.Y. Chang, Phang Boon Lim, Spencer J. Sherwin, Nicholas S. Peters, Jennifer H. Siggers, and Fu Siong Ng. "An automated algorithm for determining conduction velocity, wavefront direction and origin of focal cardiac arrhythmias using a multipolar catheter." In: *2014 36th Annual International Conference of the IEEE Engineering in Medicine and Biology Society, EMBC 2014*. 2014, pp. 1583–1586. ISBN: 9781424479290. DOI: [10.1109/EMBC.2014.6943906](https://doi.org/10.1109/EMBC.2014.6943906).
- [28] Junjie Cao, Andrea Tagliasacchi, Matt Olson, Hao Zhang, and Zhinxun Su. "Point cloud skeletons via laplacian based contraction." In: *Shape Modeling International Conference (SMI), 2010*. IEEE. 2010, pp. 187–197.
- [29] *Catecholaminergic polymorphic ventricular tachycardia - Genetics Home Reference - NIH*. URL: <https://ghr.nlm.nih.gov/condition/catecholaminergic-polymorphic-ventricular-tachycardia>.
- [30] Raymond H. Chan, Susie N. Hong, Jaime L. Shaw, Lois A. Goepfert, Kraig V. Kissinger, Beth Goddu, Mark E. Josephson, Warren J. Manning, and Reza Nezafat. "Free-breathing cardiac MR with a fixed navigator efficiency using adaptive gating window size." In: *Magnetic Resonance in Medicine* 68.6 (2012), pp. 1866–1875. ISSN: 07403194. DOI: [10.1002/mrm.24210](https://doi.org/10.1002/mrm.24210).

- [31] Enn Ling Chen, João A.C. Lima, and Robert M. Judd. "Myocardial Gd-DTPA kinetics determine MRI contrast enhancement and reflect the extent and severity of myocardial injury after acute reperfused infarction." In: *Circulation* 94.12 (1996), pp. 3318–3326. ISSN: 00097322. DOI: [10.1161/01.CIR.94.12.3318](https://doi.org/10.1161/01.CIR.94.12.3318).
- [32] Rasheda A. Chowdhury, Pravina M. Patel, Rita Jabr, Aziz U. Momin, Joshua Vecht, Rosaire Gray, Alex Shipolini, Christopher H. Fry, and Nicholas S. Peters. "Relationship between connexin expression and gap-junction resistivity in human atrial myocardium." In: *Circulation: Arrhythmia and Electrophysiology* 7.2 (2014), pp. 321–329. ISSN: 19413084. DOI: [10.1161/CIRCEP.113.000606](https://doi.org/10.1161/CIRCEP.113.000606).
- [33] Rasheda A. Chowdhury, Mark C S Hall, Pravina M. Patel, Clifford J. Garratt, and Nicholas S. Peters. "Fractionation of electrograms is caused by colocalized conduction block and connexin disorganization in the absence of fibrosis as AF becomes persistent in the goat model." In: *Heart Rhythm* 12.2 (2015), pp. 397–408. ISSN: 15563871. DOI: [10.1016/j.hrthm.2014.10.027](https://doi.org/10.1016/j.hrthm.2014.10.027).
- [34] Paolo Cignoni, Marco Callieri, Massimiliano Corsini, Matteo Dellepiane, Fabio Ganovelli, and Guido Ranzuglia. "Meshlab: an open-source mesh processing tool." In: *Eurographics Italian Chapter Conference*. Vol. 2008, pp. 129–136.
- [35] Samantha A. Clarke, T. Alexander Quinn, and Jeffrey W. Holmes. "Physiological implications of myocardial scar structure." In: *Comprehensive Physiology* 5.4 (2015). Amazing summary of conduction properties after MI, pp. 1877–1909. ISSN: 20404603. DOI: [10.1002/cphy.c140067](https://doi.org/10.1002/cphy.c140067).
- [36] James Coromilas, Nicholas J. Severs, and Andrew L. Wit. "Disturbed connexin43 gap junction distribution correlates with the location of reentrant circuits in the epicardial border zone of healing canine infarcts that cause ventricular tachycardia." In: *Circulation* 95.4 (1997), pp. 988–996. ISSN: 00097322. DOI: [10.1161/01.CIR.95.4.988](https://doi.org/10.1161/01.CIR.95.4.988).
- [37] James Coromilas, Michael S. Hanna, Mark E. Josephson, Constantinos Costeas, and Andrew L. Wit. "Characteristics of the temporal and spatial excitable gap in anisotropic reentrant circuits causing sustained ventricular tachycardia." In: *Circulation Research* 82.2 (1998), pp. 279–293. ISSN: 00097330. DOI: [10.1161/01.RES.82.2.279](https://doi.org/10.1161/01.RES.82.2.279).
- [38] Nan Cui, Pradosh Kharel, and Viktor Gruev. "Augmented reality with Microsoft HoloLens holograms for near infrared fluorescence based image guided surgery." In: *Molecular-Guided Surgery: Molecules, Devices, and Applications III*. Vol. 10049. International Society for Optics and Photonics, p. 100490I.

- [39] Maria E Currie, A Jonathan McLeod, John T Moore, Michael WA Chu, Rajni Patel, Bob Kiaii, and Terry M Peters. "Augmented reality system for ultrasound guidance of transcatheter aortic valve implantation." In: *Innovations: Technology and Techniques in Cardiothoracic and Vascular Surgery* 11.1 (2016), pp. 31–39. ISSN: 1556-9845.
- [40] Fred D Davis. "Perceived usefulness, perceived ease of use, and user acceptance of information technology." In: *MIS quarterly* (1989), pp. 319–340. ISSN: 0276-7783.
- [41] JM De Bakker, FJ Van Capelle, Michiel J Janse, AA Wilde, Ruben Coronel, Anton E Becker, Koert P Dingemans, Norbert M Van Hemel, and RN Hauer. "Reentry as a cause of ventricular tachycardia in patients with chronic ischemic heart disease: electrophysiologic and anatomic correlation." In: *Circulation* 77.3 (1988), pp. 589–606. ISSN: 0009-7322.
- [42] JM De Bakker, FJ Van Capelle, Michiel J Janse, S Tasseron, Jessica T Vermeulen, N De Jonge, and Jaap R Lahpor. "Slow conduction in the infarcted human heart. 'Zigzag' course of activation." In: *Circulation* 88.3 (1993), pp. 915–926.
- [43] T Dickfeld, J Tian, G Ahmad, A Jimenez, A Turgeman, R Kuk, M Peters, A Saliaris, M Saba, and S Shorofsky. "MRI-Guided ventricular tachycardia ablation: integration of late gadolinium-enhanced 3D scar in patients with implantable cardioverter-defibrillators." In: *Circ Arrhythm Electrophysiol* 4.2 (2011), pp. 172–184. ISSN: 1941-3084.
- [44] Timm Dickfeld, Jing Tian, Ghada Ahmad, Alejandro Jimenez, Aharon Turgeman, Richard Kuk, Matthew Peters, Anastasios Saliaris, Magdi Saba, Stephen Shorofsky, et al. "MRI-guided ventricular tachycardia ablation." In: *Circulation: Arrhythmia and Electrophysiology* 4.2 (2011), pp. 172–184.
- [45] Heidi L Estner, M Muz Zviman, Dan Herzka, Frank Miller, Valeria Castro, Saman Nazarian, Hiroshi Ashikaga, Yoav Dori, Ronald D Berger, Hugh Calkins, et al. "The critical isthmus sites of ischemic ventricular tachycardia are in zones of tissue heterogeneity, visualized by magnetic resonance imaging." In: *Heart Rhythm* 8.12 (2011), pp. 1942–1949.
- [46] Andriy Fedorov, Reinhard Beichel, Jayashree Kalpathy-Cramer, Julien Finet, Jean-Christophe Fillion-Robin, Sonia Pujol, Christian Bauer, Dominique Jennings, Fiona Fennessy, Milan Sonka, et al. "3D Slicer as an image computing platform for the Quantitative Imaging Network." In: *Magnetic resonance imaging* 30.9 (2012), pp. 1323–1341.

- [47] Juan Fernández-Armenta, Antonio Berruezo, Lluís Mont, Marta Sitges, David Andreu, Etelvino Silva, Jose Tomás Ortiz-Pérez, Jose María Tolosana, Teresa M de Caralt, Rosario Jesús Perea, et al. "Use of myocardial scar characterization to predict ventricular arrhythmia in cardiac resynchronization therapy." In: *Europace* 14.11 (2012), pp. 1578–1586.
- [48] Juan Fernández-Armenta, Antonio Berruezo, David Andreu, Oscar Camara, Etelvino Silva, Luis Serra, Valeria Barbarito, Luigi Carotenutto, Reinder Evertz, José T Ortiz-Pérez, et al. "Three-dimensional architecture of scar and conducting channels based on high resolution ce-CMR: insights for ventricular tachycardia ablation." In: *Circulation: Arrhythmia and Electrophysiology* (2013), CIRCEP–113.
- [49] Juan Fernández-Armenta, Antonio Berruezo, Lluís Mont, Marta Sitges, David Andreu, Etelvino Silva, Jose Tomás Ortiz-Pérez, Jose María Tolosana, Teresa M de Caralt, and Rosario Jesús Perea. "Use of myocardial scar characterization to predict ventricular arrhythmia in cardiac resynchronization therapy." In: *Europace* 14.11 (2012), pp. 1578–1586. ISSN: 1532-2092.
- [50] Juan Fernández-Armenta, Antonio Berruezo, David Andreu, Oscar Camara, Etelvino Silva, Luis Serra, Valeria Barbarito, Luigi Carotenutto, Reinder Evertz, and José T Ortiz-Pérez. "Three-dimensional architecture of scar and conducting channels based on high resolution ce-CMR: insights for ventricular tachycardia ablation." In: *Circ Arrhythm Electrophysiol* (2013), CIRCEP. 113.000264. ISSN: 1941-3149.
- [51] David S. Fieno, Todd B. Parrish, Kathleen Harris, Enn Ling Chen, Orlando Simonetti, Jeffrey Bundy, J. Paul Finn, Francis J. Klocke, and Robert M. Judd. "Relationship of MRI delayed contrast enhancement to irreversible injury, infarct age, and contractile function." In: *Circulation* 100.19 (1999), pp. 1992–2002. ISSN: 00097322. DOI: [10.1161/01.CIR.100.19.1992](https://doi.org/10.1161/01.CIR.100.19.1992).
- [52] David S. Fieno, Raymond J. Kim, F. Scott Pereles, Rod Passman, Gina Song, Alan H. Kadish, and Jeffrey J. Goldberger. "Infarct morphology identifies patients with substrate for sustained ventricular tachycardia." In: *Journal of the American College of Cardiology* 45.7 (2005), pp. 1104–1108. ISSN: 07351097. DOI: [10.1016/j.jacc.2004.12.057](https://doi.org/10.1016/j.jacc.2004.12.057).
- [53] Andrew S Flett, Jonathan Hasleton, Christopher Cook, Derek Hausenloy, Giovanni Quarta, Cono Ariti, Vivek Muthurangu, and James C Moon. "Evaluation of techniques for the quantification of myocardial scar of differing etiology using cardiac magnetic resonance." In: *JACC Cardiovasc Imaging* 4.2 (2011), pp. 150–156. ISSN: 1936-878X.

- [54] Nicola Galea, Iacopo Carbone, David Cannata, Giuseppe Cannavale, Bettina Conti, Roberto Galea, Andrea Frustaci, Carlo Catalano, and Marco Francone. "Right ventricular cardiovascular magnetic resonance imaging: normal anatomy and spectrum of pathological findings." In: *Insights into imaging* 4.2 (2013), pp. 213–223.
- [55] *Geographic Projections*. URL: <http://pnavarrc.github.io/workshop-d3-maps/pages/geographic-projections/>.
- [56] *George Washington University Heart & Vascular Institute*. URL: <http://www.gwheartandvascular.org/education/cardiovascular-diseases/anatomy-and-function-of-the-hearts-electrical-system/>.
- [57] RIVA Giuseppe and Brenda K Wiederhold. "The new dawn of virtual reality in health care: medical simulation and experiential interface." In: *ARCTT* (2015), p. 3.
- [58] Ilan Goldenberg, Valentina Kutyifa, Jayson R. Baman, Scott Solomon, Arthur J. Moss, Barbara Szepietowska, Scott McNitt, Bronislava Polonsky, Wojciech Zareba, and Alon Barsheshet. "Relative wall thickness and the risk for ventricular tachyarrhythmias in patients with left ventricular dysfunction." In: *Journal of the American College of Cardiology* 67.3 (2016), pp. 303–312. ISSN: 15583597. DOI: [10.1016/j.jacc.2015.10.076](https://doi.org/10.1016/j.jacc.2015.10.076).
- [59] Rosaire P. Gray, Paramdeep S. Dhillon, Rita I. Jabr, Emmanuel Dupont, Pravina M. Patel, and Nicholas S. Peters. "Architectural correlates of myocardial conduction: Changes to the topography of cellular coupling, intracellular conductance, and action potential propagation with hypertrophy in guinea-pig ventricular myocardium." In: *Circulation: Arrhythmia and Electrophysiology* 7.6 (2014), pp. 1198–1204. ISSN: 19413084. DOI: [10.1161/CIRCEP.114.001471](https://doi.org/10.1161/CIRCEP.114.001471).
- [60] Mohammadali Habibi et al. "Association of left atrial local conduction velocity with late gadolinium enhancement on cardiac magnetic resonance in patients with atrial fibrillation." In: *Circulation: Arrhythmia and Electrophysiology* 9.3 (2016). ISSN: 19413084. DOI: [10.1161/CIRCEP.115.002897](https://doi.org/10.1161/CIRCEP.115.002897).
- [61] Jonathan Hasleton, Christopher Cook, Derek Hausenloy, Giovanni Quarta, Cono Ariti, Vivek Muthurangu, and James C. Moon. "Evaluation of techniques for the quantification of myocardial scar of differing etiology using cardiac magnetic resonance." In: *JACC: Cardiovascular Imaging* 4.2 (2011), pp. 150–156. ISSN: 1936878X. DOI: [10.1016/j.jcmg.2010.11.015](https://doi.org/10.1016/j.jcmg.2010.11.015).
- [62] *Heart Information Center: Heart Anatomy*. URL: <https://www.texasheart.org/heart-health/heart-information-center/topics/heart-anatomy/>.

- [63] Craig S. Henriquez. "Genesis of complex fractionated atrial electrograms in zones of slow conduction: A computer model of microfibrosis." In: *Heart Rhythm* 6.6 (2009), pp. 803–810. ISSN: 15475271. DOI: [10.1016/j.hrthm.2009.02.026](https://doi.org/10.1016/j.hrthm.2009.02.026).
- [64] L. N. Horowitz and A. Farshidi. "Continuous local electrical activity. A mechanism of recurrent ventricular tachycardia." In: *Circulation* 57.4 (1978), pp. 659–665. ISSN: 00097322. DOI: [10.1161/01.CIR.57.4.659](https://doi.org/10.1161/01.CIR.57.4.659).
- [65] Leonard N. Horowitz, Ardeshir Farshidi, Scott R. Spielman, Eric L. Michelson, and Allan M. Greenspan. "Sustained ventricular tachycardia: Evidence for protected localized reentry." In: *The American Journal of Cardiology* 42.3 (1978), pp. 416–424. ISSN: 00029149. DOI: [10.1016/0002-9149\(78\)90936-0](https://doi.org/10.1016/0002-9149(78)90936-0).
- [66] Christopher L.-H. Huang and James A. Fraser. "Determinants of myocardial conduction velocity: implications for arrhythmogenesis." In: *Frontiers in Physiology* 4:154 (2013). ISSN: 1664-042X. DOI: [10.3389/fphys.2013.00154](https://doi.org/10.3389/fphys.2013.00154).
- [67] Leah Iles, Heinz Pfluger, Lisa Lefkovits, Michelle J Butler, Peter M Kistler, David M Kaye, and Andrew J Taylor. "Myocardial fibrosis predicts appropriate device therapy in patients with implantable cardioverter-defibrillators for primary prevention of sudden cardiac death." In: *Journal of the American College of Cardiology* 57.7 (2011), pp. 821–828. ISSN: 0735-1097.
- [68] M. J. Janse and F. J.G. Wilms-Schopman. "Changes in conduction velocity during acute ischemia in ventricular myocardium of the isolated porcine heart." In: *Circulation* 73.1 (1986), pp. 189–198. ISSN: 00097322. DOI: [10.1161/01.CIR.73.1.189](https://doi.org/10.1161/01.CIR.73.1.189).
- [69] Roy M John, Usha B Tedrow, Bruce A Koplan, Christine M Albert, Laurence M Epstein, Michael O Sweeney, Amy Leigh Miller, Gregory F Michaud, and William G Stevenson. "Ventricular arrhythmias and sudden cardiac death." In: *The Lancet* 380.9852 (2012), pp. 1520–1529. ISSN: 0140-6736.
- [70] Mark E Josephson and David J Callans. "Using the twelve-lead electrocardiogram to localize the site of origin of ventricular tachycardia." In: *Heart Rhythm* 2.4 (2005), pp. 443–446.
- [71] Mark E Josephson, Leonard N Horowitz, Harvey L Waxman, Michael E Cain, Scott R Spielman, Allan M Greenspan, Francis E Marchlinski, and Marilyn D Ezri. "Sustained ventricular tachycardia: role of the 12-lead electrocardiogram in localizing site of origin." In: *Circulation* 64.2 (1981), pp. 257–272.
- [72] Prapa Kanagaratnam, Vias Markides, D. Wyn Davies, and Nicholas Peters. "Age-related changes in human left and right atrial conduction." In: *Journal of Cardiovascular Electrophysiology*

- 17.2 (2006), pp. 120–127. ISSN: 10453873. DOI: [10.1111/j.1540-8167.2005.00293.x](https://doi.org/10.1111/j.1540-8167.2005.00293.x).
- [73] Michael Kazhdan, Matthew Bolitho, and Hugues Hoppe. “Poisson surface reconstruction.” In: *Proceedings of the fourth Eurographics symposium on Geometry processing*. Eurographics Association, pp. 61–70. ISBN: 3905673363.
- [74] Bruce H. KenKnight, Jack M. Rogers, Russel E. Hillsley, Raymond E. Ideker, and William M. Smith. “Estimation of conduction velocity vector fields from epicardial mapping data.” In: *IEEE Transactions on Biomedical Engineering* 45.5 (1998), pp. 553–562. ISSN: 00189294. DOI: [10.1109/10.668741](https://doi.org/10.1109/10.668741).
- [75] Raymond J Kim, Enn-Ling Chen, Robert M Judd, et al. “Myocardial Gd-DTPA kinetics determine MRI contrast enhancement and reflect the extent and severity of myocardial injury after acute reperfused infarction.” In: *Circulation* 94.12 (1996), pp. 3318–3326.
- [76] Raymond J Kim, David S Fieno, Todd B Parrish, Kathleen Harris, Enn-Ling Chen, Orlando Simonetti, Jeffrey Bundy, J Paul Finn, Francis J Klocke, and Robert M Judd. “Relationship of MRI delayed contrast enhancement to irreversible injury, infarct age, and contractile function.” In: *Circulation* 100.19 (1999), pp. 1992–2002.
- [77] Raymond J Kim, David S Fieno, Todd B Parrish, Kathleen Harris, Enn-Ling Chen, Orlando Simonetti, Jeffrey Bundy, J Paul Finn, Francis J Klocke, and Robert M Judd. “Relationship of MRI delayed contrast enhancement to irreversible injury, infarct age, and contractile function.” In: *Circulation* 100.19 (1999), pp. 1992–2002. ISSN: 0009-7322.
- [78] Andre G. Kleber, Markus Rottmann, Eran Leshem, Michael Barkagan, Cory M. Tschabrunn, Fernando M. Contreras-Valdes, and Alfred E. Buxton. “Infarct-related ventricular tachycardia: redefining the electrophysiological substrate of the isthmus during sinus rhythm.” In: *JACC: Clinical Electrophysiology* 4.8 (2018), pp. 1033–1048. ISSN: 2405500X. DOI: [10.1016/j.jacep.2018.04.007](https://doi.org/10.1016/j.jacep.2018.04.007).
- [79] Igor Klem, Jonathan W Weinsaft, Tristram D Bahnson, Don Hegland, Han W Kim, Brenda Hayes, Michele A Parker, Robert M Judd, and Raymond J Kim. “Assessment of myocardial scarring improves risk stratification in patients evaluated for cardiac defibrillator implantation.” In: *Journal of the American College of Cardiology* 60.5 (2012), pp. 408–420. ISSN: 0735-1097.

- [80] Ivo Kuhlemann, Markus Kleemann, Philipp Jauer, Achim Schweikard, and Floris Ernst. "Towards X-ray free endovascular interventions using HoloLens for on-line holographic visualisation." In: *Health-care Technology Letters* 4.5 (2017), p. 184.
- [81] Raymond Y. Kwong, Michael Jerosch-Herold, and Bobak Heydari. *Cardiovascular Magnetic Resonance Imaging*. Springer-Verlag New York, 2019.
- [82] Armin Luik, Christopher Schilling, Gunnar Seemann, Martin W. Krueger, Cristian Lorenz, Claus Schmitt, and Olaf Dössel. "Conduction velocity restitution of the human atrium—An efficient measurement protocol for clinical electrophysiological studies." In: *IEEE Transactions on Biomedical Engineering* 58.9 (2011), pp. 2648–2655. ISSN: 00189294. DOI: [10.1109/TBME.2011.2160453](https://doi.org/10.1109/TBME.2011.2160453).
- [83] Thomas A. Meijers, Paul Knaapen, Aernout M. Beek, Albert C. Van Rossum, and Cornelis P. Allaart. "Scar size and characteristics assessed by CMR predict ventricular arrhythmias in ischaemic cardiomyopathy: Comparison of previously validated models." In: *Heart* 97.23 (2011), pp. 1951–1956. ISSN: 13556037. DOI: [10.1136/heartjnl-2011-300060](https://doi.org/10.1136/heartjnl-2011-300060).
- [84] Antonio Meola, Fabrizio Cutolo, Marina Carbone, Federico Cagnazzo, Mauro Ferrari, and Vincenzo Ferrari. "Augmented reality in neurosurgery: a systematic review." In: *Neurosurgical review* 40.4 (2017), pp. 537–548. ISSN: 0344-5607.
- [85] Christopher F. Miller et al. "Myocardial structural associations with local electrograms: A study of postinfarct ventricular tachycardia pathophysiology and magnetic resonance-based noninvasive mapping." In: *Circulation: Arrhythmia and Electrophysiology* 5.6 (2012), pp. 1081–1090. ISSN: 19413149. DOI: [10.1161/CIRCEP.112.970699](https://doi.org/10.1161/CIRCEP.112.970699).
- [86] Sergey Mironov, Clément Taravant, Julien Brec, Luis M. Vaquero, Krishna Bandaru, Uma Mahesh R. Avula, Haruo Honjo, Itsuo Kodama, Omer Berenfeld, and Jérôme Kalifa. "Heterogeneous atrial wall thickness and stretch promote scroll waves anchoring during atrial fibrillation." In: *Cardiovascular Research* 94.1 (2012), pp. 48–57. ISSN: 00086363. DOI: [10.1093/cvr/cvr357](https://doi.org/10.1093/cvr/cvr357).
- [87] Mehdi H Moghari, Raymond H Chan, Susie N Hong, Jaime L Shaw, Lois A Goepfert, Kraig V Kissinger, Beth Goddu, Mark E Josephson, Warren J Manning, and Reza Nezafat. "Free-breathing cardiac MR with a fixed navigator efficiency using adaptive gating window size." In: *Magn Reson Med* 68.6 (2012), pp. 1866–1875. ISSN: 1522-2594.

- [88] John M. Morgan, Nicola Carroll, David C. Murday, Paul R. Roberts, Charles R. Peebles, Stephen P. Harden, and Nick P. Curzen. "The extent of left ventricular scar quantified by late gadolinium enhancement MRI is associated with spontaneous ventricular arrhythmias in patients with coronary artery disease and implantable cardioverter- defibrillators." In: *Circulation: Arrhythmia and Electrophysiology* 4.3 (2011), pp. 324–330. ISSN: 19413149. DOI: [10.1161/CIRCEP.110.959544](https://doi.org/10.1161/CIRCEP.110.959544).
- [89] Ulf Neisius, Connie W. Tsao, Sophie Berg, Elizabeth Goddu, Patrick Pierce, Tamer A. Basha, Long Ngo, Warren J. Manning, and Reza Nezafat. "Gray blood late gadolinium enhancement cardiovascular magnetic resonance for improved detection of myocardial scar." In: *Journal of Cardiovascular Magnetic Resonance* 20.1 (2018). ISSN: 1532429X. DOI: [10.1186/s12968-018-0442-2](https://doi.org/10.1186/s12968-018-0442-2).
- [90] F. S. Ng, M. S. Sulkin, R. M. Arthur, and I. R. Efimov. "Processing and analysis of cardiac optical mapping data obtained with potentiometric dyes." In: *AJP: Heart and Circulatory Physiology* 303.7 (2012), H753–H765. ISSN: 0363-6135. DOI: [10.1152/ajpheart.00404.2012](https://doi.org/10.1152/ajpheart.00404.2012).
- [91] Esther Perez-David, Ángel Arenal, José L Rubio-Guivernau, Roberto Del Castillo, Leonardo Atea, Elena Arbelo, Eduardo Caballero, Verónica Celorrio, Tomas Datino, Esteban Gonzalez-Torrecilla, et al. "Noninvasive identification of ventricular tachycardia-related conducting channels using contrast-enhanced magnetic resonance imaging in patients with chronic myocardial infarction: comparison of signal intensity scar mapping and endocardial voltage mapping." In: *Journal of the American College of Cardiology* 57.2 (2011), pp. 184–194.
- [92] *Pericardium*. 2019. URL: https://en.wikipedia.org/wiki/Pericardium#/media/File:Blausen_0470_HeartWall.png.
- [93] Arkady M. Pertsov, William T. Baxter, Jorge M. Davidenko, Richard A. Gray, and José Jalife. "Wave-front curvature as a cause of slow conduction and block in isolated cardiac muscle." In: *Circulation Research* 75.6 (1994), pp. 1014–1028. ISSN: 00097330. DOI: [10.1161/01.RES.75.6.1014](https://doi.org/10.1161/01.RES.75.6.1014).
- [94] Heinz Pfluger, Lisa Lefkovits, Michelle J. Butler, Peter M. Kistler, David M. Kaye, and Andrew J. Taylor. "Myocardial fibrosis predicts appropriate device therapy in patients with implantable cardioverter-defibrillators for primary prevention of sudden cardiac death." In: *Journal of the American College of Cardiology* 57.7 (2011), pp. 821–828. ISSN: 07351097. DOI: [10.1016/j.jacc.2010.06.062](https://doi.org/10.1016/j.jacc.2010.06.062).

- [95] "Poisson surface reconstruction and its applications." In: *Proceedings of the 2008 ACM symposium on Solid and physical modeling - SPM '08*. Vol. 44. 12. ACM Press, 2008, p. 10. ISBN: 9781605581062. DOI: [10.1145/1364901.1364904](https://doi.org/10.1145/1364901.1364904).
- [96] A Prakosa, P Malamas, S Zhang, F Pashakhanloo, H Arevalo, DA Herzka, A Lardo, H Halperin, E McVeigh, and N Trayanova. "Methodology for image-based reconstruction of ventricular geometry for patient-specific modeling of cardiac electrophysiology." In: *Progress in biophysics and molecular biology* 115.2 (2014), pp. 226–234. ISSN: 0079-6107.
- [97] DP Ripley, TA Musa, LE Dobson, S Plein, and JP Greenwood. "Cardiovascular magnetic resonance imaging: what the general cardiologist should know." In: *Heart* 102.19 (2016), pp. 1589–1603.
- [98] Stijntje D Roes, C Jan Willem Borleffs, Rob J van der Geest, Jos JM Westenberg, Nina Ajmone Marsan, Theodorus AM Kaandorp, Johan HC Reiber, Katja Zeppenfeld, Hildo J Lamb, Albert de Roos, et al. "Infarct Tissue Heterogeneity Assessed With Contrast-Enhanced MRI Predicts Spontaneous Ventricular Arrhythmia in Patients With Ischemic Cardiomyopathy and Implantable Cardioverter-DefibrillatorCLINICAL PERSPECTIVE." In: *Circulation: Cardiovascular Imaging* 2.3 (2009), pp. 183–190.
- [99] Stijntje D Roes, C Jan Willem Borleffs, Rob J van der Geest, Jos JM Westenberg, Nina Ajmone Marsan, Theodorus AM Kaandorp, Johan HC Reiber, Katja Zeppenfeld, Hildo J Lamb, and Albert de Roos. "Infarct Tissue Heterogeneity Assessed With Contrast-Enhanced MRI Predicts Spontaneous Ventricular Arrhythmia in Patients With Ischemic Cardiomyopathy and Implantable Cardioverter-DefibrillatorCLINICAL PERSPECTIVE." In: *Circulation: Cardiovascular Imaging* 2.3 (2009), pp. 183–190. ISSN: 1941-9651.
- [100] C. H. Roney, F. S. Ng, J. H. Siggers, S. J. Sherwin, and N. S. Peters. "Techniques for automated local activation time annotation and conduction velocity estimation in cardiac mapping." In: *Computers in Biology and Medicine* 65 (2015), pp. 229–242. ISSN: 18790534. DOI: [10.1016/j.compbiomed.2015.04.027](https://doi.org/10.1016/j.compbiomed.2015.04.027).
- [101] Caroline H. Roney, Rheeda L. Ali, Norman A. Qureshi, Phang Boon Lim, and Nicholas S. Peters. "A software platform for the comparative analysis of electroanatomic and imaging data including conduction velocity mapping." In: *2014 36th Annual International Conference of the IEEE Engineering in Medicine and Biology Society, EMBC 2014*. 2014, pp. 1591–1594. ISBN: 9781424479290. DOI: [10.1109/EMBC.2014.6943908](https://doi.org/10.1109/EMBC.2014.6943908).

- [102] Sébastien Roujol, Reza Nezafat, Beverly Faulkner-Jones, Alfred E. Buxton, Mark E. Josephson, and Elad Anter. "A swine model of infarct-related reentrant ventricular tachycardia: Electroanatomic, magnetic resonance, and histopathological characterization." In: *Heart Rhythm* 13.1 (2016), pp. 262–273. ISSN: 15563871. DOI: [10.1016/j.hrthm.2015.07.030](https://doi.org/10.1016/j.hrthm.2015.07.030).
- [103] Frédéric Sacher et al. "Myocardial wall thinning predicts transmural substrate in patients with scar-related ventricular tachycardia." In: *Heart Rhythm* 14.2 (2017), pp. 155–163. ISSN: 15563871. DOI: [10.1016/j.hrthm.2016.11.012](https://doi.org/10.1016/j.hrthm.2016.11.012).
- [104] Eric Saloux, Audrey Emmanuelle Dugué, Alain Lebon, Adrien Lemaitre, Vincent Roule, Fabien Labombarda, Nicole Provost, Sophie Gomes, Patrice Scanu, and Paul Milliez. "Scar extent evaluated by late gadolinium enhancement CMR: A powerful predictor of long term appropriate ICD therapy in patients with coronary artery disease." In: *Journal of Cardiovascular Magnetic Resonance* 15.1 (2013). ISSN: 10976647. DOI: [10.1186/1532-429X-15-12](https://doi.org/10.1186/1532-429X-15-12).
- [105] Richard J. Schilling, D. Wyn Davies, and Nicholas S. Peters. "Characteristics of wavefront propagation in reentrant circuits causing human ventricular tachycardia." In: *Circulation* 105.18 (2002), pp. 2172–2178. ISSN: 00097322. DOI: [10.1161/01.CIR.0000015702.49326.BC](https://doi.org/10.1161/01.CIR.0000015702.49326.BC).
- [106] André Schmidt, Clerio F Azevedo, Alan Cheng, Sandeep N Gupta, David A Bluemke, Thomas K Foo, Gary Gerstenblith, Robert G Weiss, Eduardo Marbán, Gordon F Tomaselli, et al. "Infarct tissue heterogeneity by magnetic resonance imaging identifies enhanced cardiac arrhythmia susceptibility in patients with left ventricular dysfunction." In: *Circulation* 115.15 (2007), pp. 2006–2014.
- [107] André Schmidt, Clerio F Azevedo, Alan Cheng, Sandeep N Gupta, David A Bluemke, Thomas K Foo, Gary Gerstenblith, Robert G Weiss, Eduardo Marbán, and Gordon F Tomaselli. "Infarct tissue heterogeneity by magnetic resonance imaging identifies enhanced cardiac arrhythmia susceptibility in patients with left ventricular dysfunction." In: *Circulation* 115.15 (2007), pp. 2006–2014. ISSN: 0009-7322.
- [108] Paul A Scott, John M Morgan, Nicola Carroll, David C Murday, Paul R Roberts, Charles R Peebles, Stephen P Harden, and Nick P Curzen. "The Extent of Left Ventricular Scar Quantified by Late Gadolinium Enhancement MRI Is Associated With Spontaneous Ventricular Arrhythmias in Patients With Coronary Artery Disease and Implantable Cardioverter-Defibrillators Clinical Perspective." In: *Circulation: Arrhythmia and Electrophysiology* 4.3 (2011), pp. 324–330. ISSN: 1941-3149.

- [109] Paul A Scott, John M Morgan, Nicola Carroll, David C Murday, Paul R Roberts, Charles R Peebles, Stephen P Harden, and Nick P Curzen. "The Extent of Left Ventricular Scar Quantified by Late Gadolinium Enhancement MRI Is Associated with Spontaneous Ventricular Arrhythmias in Patients with Coronary Artery Disease and Implantable Cardioverter Defibrillators." In: *Circulation: Arrhythmia and Electrophysiology* (2011), CIRCEP-110.
- [110] Adolphe J. Shayne, Kenneth A. Brown, Sandeep N. Gupta, Carmen W. Chan, Tuan M. Luu, Marcelo F. Di Carli, H. Glenn Reynolds, William G. Stevenson, and Raymond Y. Kwong. "Characterization of the peri-infarct zone by contrast-enhanced cardiac magnetic resonance imaging is a powerful predictor of post-myocardial infarction mortality." In: *Circulation* 114.1 (2006), pp. 32–39. ISSN: 00097322. DOI: [10.1161/CIRCULATIONAHA.106.613414](https://doi.org/10.1161/CIRCULATIONAHA.106.613414).
- [111] Jennifer N Silva, Michael K Southworth, Aarti Dalal, George F Van Hare, and Jonathan R Silva. "Improving Visualization and Interaction During Transcatheter Ablation Using an Augmented Reality System: First-in-Human Experience." In: *Circulation* 136.suppl_1 (2017), A15358–A15358.
- [112] B. H. Smaill. "The analysis of cardiac function: A continuum approach." In: *Progress in Biophysics and Molecular Biology* 52.2 (1988), pp. 101–164. ISSN: 00796107. DOI: [10.1016/0079-6107\(88\)90004-1](https://doi.org/10.1016/0079-6107(88)90004-1).
- [113] Eric C Stecker, Kyndaron Reinier, Eloi Marijon, Kumar Narayanan, Carmen Teodorescu, Audrey Uy-Evanado, Karen Gunson, Jonathan Jui, and Sumeet S Chugh. "Public health burden of sudden cardiac death in the United States." In: *Circulation: Arrhythmia and Electrophysiology* 7.2 (2014), pp. 212–217.
- [114] *Summit Medical Group Web Site*. URL: https://www.summitmedicalgroup.com/library/adult_health/car_electrophysiologic_study/.
- [115] Maxine C. Tang, Connie Tsao, Cory M. Tschabrunn, Elad Anter, Warren J. Manning, and Reza Nezafat. "Improved dark blood late gadolinium enhancement (DB-LGE) imaging using an optimized joint inversion preparation and T2magnetization preparation." In: *Magnetic Resonance in Medicine* 79.1 (2018), pp. 351–360. ISSN: 15222594. DOI: [10.1002/mrm.26692](https://doi.org/10.1002/mrm.26692).
- [116] Allen G Taylor. "What Is the Microsoft HoloLens?" In: *Develop Microsoft HoloLens Apps Now*. Springer, 2016, pp. 3–7.
- [117] Joni Taylor and Victoria Hampshire. "Basic research support for shared magnetic resonance imaging resources." In: *Lab animal* 44.11 (2015), pp. 435–438.

- [118] "The statistics of linear models: back to basics." In: *Statistics and Computing* 4.4 (1994), pp. 221–234. ISSN: 0960-3174. DOI: [10.1007/BF00156745](https://doi.org/10.1007/BF00156745).
- [119] Cory M Tschabrunn, Sébastien Roujol, Reza Nezafat, Beverly Faulkner-Jones, Alfred E Buxton, Mark E Josephson, and Elad Anter. "A swine model of infarct-related reentrant ventricular tachycardia: electroanatomic, magnetic resonance, and histopathological characterization." In: *Heart Rhythm* 13.1 (2016), pp. 262–273.
- [120] Cory M Tschabrunn, Sébastien Roujol, Reza Nezafat, Beverly Faulkner-Jones, Alfred E Buxton, Mark E Josephson, and Elad Anter. "A swine model of infarct-related reentrant ventricular tachycardia: electroanatomic, magnetic resonance, and histopathological characterization." In: *Heart Rhythm* 13.1 (2016), pp. 262–273.
- [121] Cory M Tschabrunn, Sébastien Roujol, Reza Nezafat, Beverly Faulkner-Jones, Alfred E Buxton, Mark E Josephson, and Elad Anter. "A swine model of infarct-related reentrant ventricular tachycardia: electroanatomic, magnetic resonance, and histopathological characterization." In: *Heart Rhythm* 13.1 (2016), pp. 262–273. ISSN: 1547-5271.
- [122] Cory M. Tschabrunn, Jihye Jang, John Whitaker, Israel Zilberman, Christopher Beeckler, Assaf Govari, Josef Kautzner, Petr Peichl, Reza Nezafat, and Elad Anter. "High-resolution mapping of ventricular scar: Evaluation of a novel integrated multielectrode mapping and ablation catheter." In: *JACC: Clinical Electrophysiology* (2017). ISSN: 2405500X. DOI: [10.1016/j.jacep.2016.12.016](https://doi.org/10.1016/j.jacep.2016.12.016).
- [123] Cory M. Tschabrunn, Jihye Jang, Eran Leshem, Mark O'Neill, Warren J. Manning, Elad Anter, and Reza Nezafat. "Cardiac MR Characterization of left ventricular remodeling in a swine model of infarct followed by reperfusion." In: *Journal of Magnetic Resonance Imaging* 48.3 (2018), pp. 808–817. ISSN: 15222586. DOI: [10.1002/jmri.26005](https://doi.org/10.1002/jmri.26005).
- [124] Emanuela R Valsangiacomo Buechel and Luc L Mertens. "Imaging the right heart: the use of integrated multimodality imaging." In: *European heart journal* 33.8 (2012), pp. 949–960.
- [125] F. J.L. Van Capelle, M. J. Janse, S. Tasserou, J. T. Vermeulen, N. De Jonge, and J. R. Lahpor. "Slow conduction in the infarcted human heart: "Zigzag" course of activation." In: *Circulation* 88.3 (1993), pp. 915–926. ISSN: 00097322. DOI: [10.1161/01.CIR.88.3.915](https://doi.org/10.1161/01.CIR.88.3.915).

- [126] Sander Verheule, Luis Scott, Antonio Navarrete, Vikram Katari, Emily Wilson, Dev Vaz, and Jeffrey E. Olgin. "Arrhythmogenic substrate of the pulmonary veins assessed by high-resolution optical mapping." In: *Circulation* 107.13 (2003), pp. 1816–1821. ISSN: 00097322. DOI: [10.1161/01.CIR.0000058461.86339.7E](https://doi.org/10.1161/01.CIR.0000058461.86339.7E).
- [127] Z Vespalcova and M J Lab. "Electrode for recording direction of activation, conduction velocity, and monophasic action potential of myocardium." In: *The American journal of physiology* 272(4):H19 (1997). ISSN: 0002-9513.
- [128] Jonathan W. Weinsaft, Tristram D. Bahnson, Don Hegland, Han W. Kim, Brenda Hayes, Michele A. Parker, Robert M. Judd, and Raymond J. Kim. "Assessment of myocardial scarring improves risk stratification in patients evaluated for cardiac defibrillator implantation." In: *Journal of the American College of Cardiology* 60.5 (2012), pp. 408–420. ISSN: 07351097. DOI: [10.1016/j.jacc.2012.02.070](https://doi.org/10.1016/j.jacc.2012.02.070).
- [129] John Whitaker, Cory M Tschabrunn, Jihye Jang, Eran Leshem, Mark O'Neill, Warren J Manning, Elad Anter, and Reza Nezafat. "Cardiac MR Characterization of left ventricular remodeling in a swine model of infarct followed by reperfusion." In: *Journal of Magnetic Resonance Imaging* (2018).
- [130] Jianan Yao, Penelope A. Boyden, Shan Chen, Wajid Hussain, Heather S. Duffy, Edward J. Ciaccio, Nicholas S. Peters, and Andrew L. Wit. "Heterogeneous gap junction remodeling in reentrant circuits in the epicardial border zone of the healing canine infarct." In: *Cardiovascular Research* 72.2 (2006), pp. 241–249. ISSN: 00086363. DOI: [10.1016/j.cardiores.2006.07.005](https://doi.org/10.1016/j.cardiores.2006.07.005).
- [131] Tarek Zghaib, Esra G Ipek, Rozann Hansford, Hiroshi Ashikaga, Ronald D Berger, Joseph E Marine, David D Spragg, Harikrishna Tandri, Stefan L Zimmerman, and Henry Halperin. "Standard Ablation Versus Magnetic Resonance Imaging-Guided Ablation in the Treatment of Ventricular Tachycardia." In: *Circulation: Arrhythmia and Electrophysiology* 11.1 (2018), e005973. ISSN: 1941-3149.
- [132] Peter J Zimetbaum and Mark E Josephson. *Practical clinical electrophysiology*. Lippincott Williams & Wilkins, 2017.